Development and Applications of a Radar-Attenuation Model for Polar Ice Sheets

Joseph A. MacGregor

A dissertation submitted in partial fulfillment of
the requirements for the degree of

Doctor of Philosophy

University of Washington

2008

Program Authorized to Offer Degree: Earth and Space Sciences

University of Washington
Graduate School

This is to certify that I have examined this copy of a doctoral dissertation by

Joseph A. MacGregor

and have found that it is complete and satisfactory in all respects,
and that any and all revisions required by the final
examining committee have been made.

Chair of the Supervisory Committee:

_____

Dale P. Winebrenner

Reading Committee:

_____

Dale P. Winebrenner

_____

Kenichi Matsuoka

_____

Edwin D. Waddington

Date: _____

In presenting this dissertation in partial fulfillment of the requirements for the doctoral degree at the University of Washington, I agree that the Library shall make its copies freely available for inspection. I further agree that extensive copying of this dissertation is allowable only for scholarly purposes, consistent with "fair use" as prescribed in the U.S. Copyright Law. Requests for copying or reproduction of this dissertation may be referred to Proquest Information and Learning, 300 North Zeeb Road, Ann Arbor, MI 48106-1346, 1-800-521-0600, to whom the author has granted "the right to reproduce and sell (a) copies of the manuscript in microform and/or (b) printed copies of the manuscript made from microform."

Signature_____

Date_____

University of Washington

Abstract

Development and Applications of a Radar-Attenuation Model for Polar Ice Sheets

Joseph A. MacGregor

Chair of the Supervisory Committee:
Research Professor Dale P. Winebrenner
Earth and Space Sciences

Modern ice sheets are currently responding to significant climatic forcings and undergoing ice-dynamics changes that are not yet well understood. Ice-penetrating radar surveys are often used to infer their basal condition (e.g., is the bed wet or dry?) and internal properties. However, such inferences typically require a model of the electromagnetic attenuation through the ice sheet. Here I first develop and test a radar-attenuation model that is based on a synthesis of existing laboratory measurements of the dielectric properties of ice. This synthesis shows that radar attenuation in polar ice has a strong non-linear temperature dependence and a weaker linear dependence on the concentrations of acid and sea-salt chloride. This model was tested at Siple Dome, West Antarctica, using ice-core-chemistry and borehole-temperature data, and the model agreed well with an existing radar-attenuation measurement. I then use this model to investigate the nature of radar detection of accreted ice over Lake Vostok, East Antarctica. My analysis of ice-core and radar data found that the observed reflection is likely due to a fabric contrast near the boundary between the dirty and clean accreted ices. This reflection mechanism is also consistent with the spatial pattern of detection of the reflection. In anticipation of the requirements of a thermomechanical ice-sheet model to predict the spatial variation of attenuation over Lake Vostok, I develop an accumulation-rate map for the Lake Vostok region using radar data, a steady-state flowband model, and inverse methods. I found that accumulation rates there are not inversely correlated with surface elevation, that there is a broad maximum above the lake's north-

western corner, and a minimum above most of its eastern shoreline. Finally, I investigate the spatial variability of attenuation in an ice sheet, using the flowline that crosses through the Vostok ice core as an example. I use radar layers and ice-velocity and temperature outputs from an ice-sheet model to estimate the spatial variation of attenuation using a series of progressively more complex models. I found that an attenuation-rate model that uses non-uniform ice temperatures and radar layers to rescale impurity-concentration profiles can satisfactorily capture most of the spatial variability of attenuation.

TABLE OF CONTENTS

LIST OF FIGURES

LIST OF TABLES

ACKNOWLEDGMENTS

No Ph.D. dissertation is produced in a vacuum devoid of others' ideas. Only my name is on the cover page but the ideas and words of many are expressed herein.

I would first like to thank my advisor, Dale, for leading me through my adventures in graduate school, for offering sage perspectives on academia and for sharing his enthusiasm for solving the mysteries of the natural world. Ed gave me an excellent foundation in glaciology, taught me scientific humility and the value of solving small problems first. Twit taught me how to write concisely and how to avoid being misunderstood while remaining affable. Kenny taught me precision in many senses, led my first polar experience and also suggested the literature review that changed the course of my graduate career. Many collaborators outside of the UW also supported my graduate studies and helped clarify the broader value of my research, particularly Michael, Sridhar and Bob.

I would also like to thank my mother, father and brother for their unwavering support of my plans to keep moving in science, despite the already large distance. They provided the drive and emotional foundation that I needed to pursue the odd education that has sent my mind and body to many remote places. I also owe an incredible amount to John, who taught me the value of toughness and visiting one's physical and mental limits; he took me further than I ever thought possible and I hope to honor his vision.

There are many graduate students whose friendship I cherish; their support during my graduate career has been invaluable to my soul and has led to many happy memories of my time in Seattle and beyond. Lora, Jess, Wes, Bob, Steve, Heather and Kaori deserve special mention as such friends. Kat shared many hugs and second chances. Philipp was a terrific partner in my final year's athletic experiment. Michael, Harrison and George kept me grounded and merry; their wit is as humbling as mountains.

I began my graduate studies at the same time as Claire, Julia and Michelle, three amazing

individuals to whom I am forever grateful for their boundless kindness and wisdom. I hope to continue learning from them for many years to come. Claire showed me how to mix and live with zest. Julia taught me as much as tact as I can be taught, why we bake and how to listen. Michelle and I learned glaciology from and with each other, and we worked in sync for many years as officemates, happily trading ideas, Matlab riddles, neuroses, stories, smiles and sneezes. Namasté.

A final thanks to Julie, who helped make these last few months very happy ones.

DEDICATION

For Grandma, Nan, and those I trust.

Chapter 1

INTRODUCTION

> "The ice sheets of Antarctica and Greenland could raise sea level greatly. Central parts of these ice sheets have been observed to change only slowly, but near the coast rapid changes over quite large areas have been observed. In these areas, uncertainties about glacier basal conditions, ice deformation and interactions with the surrounding ocean seriously limit the ability to make accurate projections."
>
> Intergovernmental Panel on Climate Change, 2007, Working Group I, Ch. 4, p. 367

1.1 Motivation and Goals

The above quote accurately synthesizes the current state of affairs in our understanding of modern ice sheets. Accurate predictions of future sea-level rise are, in large part, limited both by our incomplete understanding of the internal and subglacial properties of modern ice sheets and by our inability to dynamically model observed ice-sheet responses to climate change. As we do not yet fully understand why ice sheets behave as they do now, we cannot yet effectively predict how they might behave in the future.

Warmer ice flows more quickly than colder ice (*Paterson* (1994)), but what parts of an ice sheet are relatively warmer than others? Do model predictions of warmer ice agree with temperature observations, and can warmer ice significantly accelerate current ice-sheet retreat? Wet beds can cause basal sliding, but what does the subglacial hydrological system look like, how is it influenced by the underlying geology, and can it change rapidly? In particular, poorly known subglacial conditions have been repeatedly cited as a key weakness in current predictive ice-sheet models (e.g., *Alley et al.* (2005); *Bell* (2008)). Hence, the goal of this dissertation is to develop and apply one of the key radioglaciological tools necessary to investigate these key ice-sheet properties.

1.2 Background

There are several geophysical methods for surveying the internal and subglacial structure of ice bodies, including active and passive seismic surveys (e.g., *Anandakrishnan et al.* (1998); *Smith et al.* (2007)), gravimetry (e.g., *Studinger et al.* (2004)), magnetometry (e.g., *Blankenship et al.* (1993)) and satellite altimetry (e.g., *Fricker et al.* (2007)). These methods have yielded key insights into crystal-orientation fabric development, the presence of subglacial till/lakes/volcanoes, and subglacial water transport. However, the primary method for such investigations is ice-penetrating radar, because it is the most efficient method for probing ice sheets and mapping properties of interest (*Bogorodsky et al.* (1985)). The relatively low attenuation (absorption) rate of radio waves in ice is one of the primary reasons for ice-penetrating radar's efficiency. Ice is yet more transparent to seismic waves, but radar systems can survey much larger regions than seismic surveys in comparable periods of time, and can also be deployed for airborne surveys.

Ice-penetrating radar surveys can reliably measure multi-kilometer ice thicknesses and an ice sheet's internal stratigraphy. These data are critical constraints for ice-flow models that attempt to predict the evolution of modern ice sheets. The intensity of recorded radio echoes can also be used to estimate internal and basal properties, such as the nature of observed internal reflections (e.g., *Matsuoka et al.* (2003)) or whether the bed is wet or dry (e.g., *Peters et al.* (2005), *Oswald and Gogineni* (2008), *Murray et al.* (2008)), by correcting those echo-intensity data for various radar-system effects (e.g., antenna gain, system gain) and losses within the ice. We can then estimate the reflectivity of the interface, which depends on the dielectric contrast and roughness at that interface and is indicative of the physical contrast there. The spatial variation of interface reflectivities can reveal their relationship to ice flow (e.g., *Blankenship et al.* (1993); *Matsuoka et al.* (2003)) and begin to address the issue of ice-sheet stability that motivates this work (section 1.1). However, such interpretations can be confounded by uncertainties in the magnitude and spatial variation of attenuation by dielectric loss, which is one of the two dominant radar-signal loss mechanisms within the ice and also the least well known; the other is simply geometric spreading of the radio wave.

The radar-attenuation rate is proportional to conductivity of the ice column through which the radio waves travel. Spatial variations in attenuation produce corresponding variations in observed echo intensities that can mask real variations in interface reflectivities. A reliable radar-attenuation model can determine the true spatial variability of an interface's reflectivity, and can therefore help illuminate the nature of observed internal and basal reflections. Results from such investigations will lead to a better understanding of the glaciological controls on ice-sheet flow.

During the early development of radioglaciology, several investigators recognized the value of a better understanding of radar attenuation (e.g., *Robin et al.* (1969), *Robin* (1975), *Bogorodsky et al.* (1985)). They recognized that it would valuable for both the interpretation of radio-echo intensities and, prior to widespread borehole-temperature measurements and computer-based thermomechanical ice-flow modeling, for the estimation of mean ice-sheet temperatures. However, early radar systems did not produce digital records, which hindered the study of echo intensities, and early studies of ice conductivity were inconsistent and did not adequately consider the role of soluble impurities (e.g., the Westphal data cited by *Evans* (1965)), which hindered the conversion of crude attenuation-rate estimates into ice temperatures. Besides these issues, at the time there was still much to be learned about the stratigraphy of newly discovered internal layers in ice sheets (*Paren and Robin* (1975), *Millar* (1981)), from which significant glaciological discoveries continue to be made (e.g., the thinning history of Roosevelt Island, *Conway et al.* (1999)). Recent radioglaciological studies have re-focused on echo intensities so, along with ever-increasing amounts of data on the dielectric properties of ice, it is now appropriate to consider a quantitative study of radar attenaution in polar ice sheets.

The electrical conductivity of ice at radar frequencies (0.3–100 MHz) is relatively low (by 1–3 orders of magnitude) compared to that of other earth materials. This property is central to a key dilemma in radioglaciology: radio-wave energy loss due to conduction is low, enabling us to detect radio echoes that have traveled several kilometers through ice, yet in the laboratory we cannot easily measure the amount of energy loss due to conduction through decimeter-sized samples of ice, because it is so low. This dilemma hindered early investigations of ice conductivity and continues to do so today. Accurately measuring con-

duction loss in small ice samples is critical for testing hypotheses regarding the conduction mechanisms present in polar ice.

Figure 1.1 illustrates the current model of conduction mechanisms in laboratory-grown and naturally occurring polar ice (e.g., *Petrenko and Whitworth* (1999). Defects in a perfect crystal structure (one that obeys both of Pauling's "ice rules"), permit electrical conduction. Ice is considered a "protonic semiconductor", which means the movement of protons (H^+ ions) constitute the charge displacement in a pure ice lattice. An extra or a missing H^+ ion surrounding an oxygen ion (O^{2-}) induces an electrical polarization in the ice crystal. These defects are called ionic defects, and they cause conduction in pure ice ("pure" in the sense that these defects do not require an ion other than H^+ or O^{2-}, the two elements that form ice). Soluble impurities (e.g., Cl^-, NH_4^+ and F^-) can produce other types of electrical defects in the lattice. These impurities can replace O^{2-} in the crystal lattice because they have a similar ionic radius, but not necessarily the same number of valence electrons. This charge difference as compared to an O^{2-} ion induces displacement of the H^+ ions, and hence a bulk polarization of the ice crystal. Other soluble impurities, especially acids, can also be present at liquid-filled grain boundaries outside of the lattice (e.g., *Mulvaney et al.* (1988)). There, H^+ ions dissociated from acid anions are mobile in the presence of an electrical field. As new methods are developed to study the microscopic properties of ice, this model of electrical conduction in polar ice will undoubtedly be refined (*Wolff* (2000)). However, because it successfully explains many of the key features of the electrical properties of ice cores (e.g., *Wolff et al.* (1997)) upon which radar-attenuation models are based, I explicitly accept its validity in this dissertation. The consequences of these assumptions are discussed in Chapter 2.

For two reasons, in this dissertation I focus exclusively on the radar attenuation of polar ice, i.e., ice bodies whose temperatures are entirely below the pressure-melting point. First and foremost, there are outstanding problems in glaciology related to polar ice, because the vast modern ice sheets of Greenland and Antarctica are composed mostly of polar ice. Second, the dielectric properties of ice are best understood for polar ice (and lab samples below $-10\ ^\circ C$), and much less so for temperate ice close to the pressure-melting point. Large scattering losses due to the englacial water system of temperate ice bodies complicates the

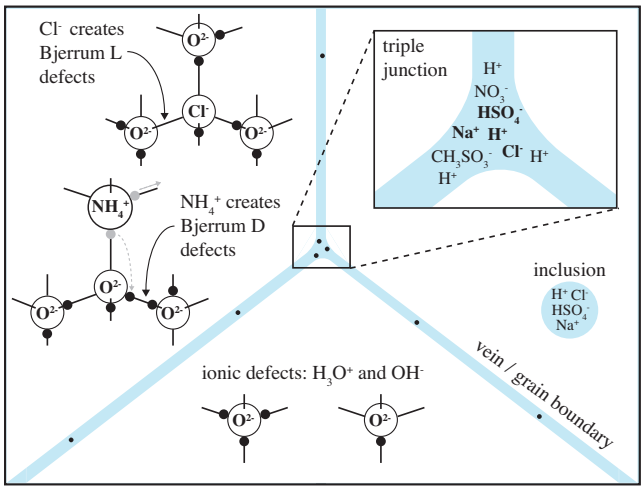

Figure 1.1: Illustration of the conduction mechanisms that are present in both pure and impurity-laden polar ice. The small circles adjacent to O^{2-} or O^{2-}-replacing ions represent H^+ ions. Blue represents water, and white represents the ice lattice.

interpretation of radar-attenuation data and models developed for it, so we cannot yet reliably predict radar attenuation through a temperate glacier.

1.3 Organization of the Dissertation

This dissertation is organized into six chapters. This chapter introduces the motivation and background for this work. The next four chapters are stand-alone studies that, within the framework of this dissertation, constitute a broad study of the development and applications of an ice-sheet radar-attenuation model. The locations of the two study areas considered in this dissertation are shown in Figure 1.2. Chapter 2 presents the initial development of the radar-attenuation model and its evaluation at Siple Dome, West Antarctica. Ice-core-chemistry data and borehole-temperature data are used to model radar attenuation there. This chapter forms the basis for all subsequent attenuation models in this dissertation. Chapter 3 applies this model to the study of accreted ice over Lake Vostok, East Antarctica, with the goal of determining the reflection mechanism and explaining the spatial pattern of its detection over this subglacial lake. A one-dimensional attenuation-rate model is necessary to derive the interface's reflectivity from the radar data. Chapter 4 temporarily diverges

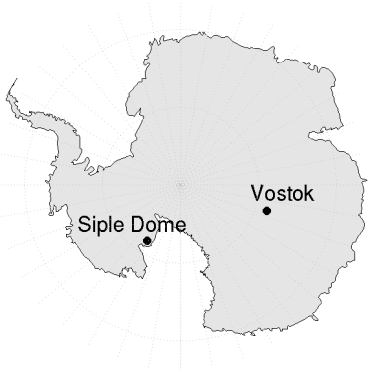

Figure 1.2: Location map showing Siple Dome and Vostok stations in Antarctica.

from the direct study of ice-sheet radar attenuation to develop an accumulation-rate map for Lake Vostok region, which is necessary for the work in Chapter 5. This accumulation-rate map is based on the depths of internal radar layers and ice-flow modeling with varying degrees of sophistication. In Chapter 5, I describe several methods for estimating the spatial variation of radar attenuation and apply them to a flowline that crosses through the Vostok ice-core site. These models use observed radar-layer depths and outputs from a thermomechanical ice-flow model to examine the effect of both temperature and impurity concentrations upon the modeled attenuation-rate field. Finally, Chapter 6 summarizes the main results of this dissertation, explains their immediate value to others in this field, and suggests future work.

Chapter 2

MODELING ENGLACIAL RADAR ATTENUATION AT SIPLE DOME, WEST ANTARCTICA, USING ICE CHEMISTRY AND TEMPERATURE DATA

This chapter was published in the Journal of Geophysical Research in 2007. My co-authors are Dale Winebrenner, Howard Conway, Kenichi Matsuoka, Paul Mayewski and Gary Clow. I wrote the text and conducted all of the work described in this chapter, including the synthesis of published data and calculation of attenuation rates at Siple Dome. Dale Winebrenner, Howard Conway and Kenichi Matusoka guided my work and edited the entire manuscript. Paul Mayewski and Gary Clow provided unpublished chemistry and temperature data, respectively, and edited portions of the manuscript related to those data. Gwenn Flowers, Robert Jacobel and an anonymous referee reviewed the manuscript.

2.1 Summary

The radar reflectivity of an ice-sheet bed is a primary measurement for discriminating between thawed and frozen beds. Uncertainty in englacial radar attenuation and its spatial variation introduces corresponding uncertainty in estimates of basal reflectivity. Radar attenuation is proportional to ice conductivity, which depends on the concentrations of acid and sea-salt chloride and the temperature of the ice. We synthesize published conductivity measurements to specify an ice-conductivity model and find that some of the dielectric properties of ice at radar frequencies are not yet well constrained. Using depth profiles of ice-core chemistry and borehole temperature and an average of the experimental values for the dielectric properties, we calculate an attenuation rate profile for Siple Dome, West Antarctica. The depth-averaged modeled attenuation rate at Siple Dome (20.0 ± 5.7 dB km^{-1}) is somewhat lower than the value derived from radar profiles (25.3 ± 1.1 dB km^{-1}). Pending more experimental data on the dielectric properties of ice, we can match the modeled and radar-derived attenuation rates by an adjustment to the value for the pure ice conductiv-

ity that is within the range of reported values. Alternatively, using the pure ice dielectric properties derived from the most extensive single dataset, the modeled depth-averaged attenuation rate is 24.0 ± 2.2 dB km^{-1}. This work shows how to calculate englacial radar attenuation using ice chemistry and temperature data and establishes a basis for mapping spatial variations in radar attenuation across an ice sheet.

2.2 Introduction

Radio-echo sounding is a proven tool for characterizing the geometry, internal structure and subglacial environment of ice sheets and glaciers (*Bogorodsky et al.* (1985)). The basal echo intensity is of special interest because it can be diagnostic of thawed/frozen conditions at the bed. However, the basal echo intensity depends not only on the dielectric properties and roughness of the basal interface but also on the characteristics of the radar system, power losses from scattering, birefringence, geometric spreading and attenuation within the overlying ice. It is therefore necessary to account for those system characteristics and englacial power losses, especially attenuation, to calculate the basal reflectivity.

Relatively little is known about englacial attenuation and its spatial variation. Here we investigate power losses caused by dielectric absorption. Previous studies have accounted for attenuation either by making measurements over an ice shelf where the theoretical reflectivity at the ice–water interface is known (e.g., *Shabtaie et al.* (1987); *Bentley et al.* (1998)), empirically (e.g., *Gades et al.* (2000)) or by using a temperature–attenuation relationship (e.g., *Peters et al.* (2005)). *Corr et al.* (1993) interpreted differences in radar-derived attenuation in two Antarctic ice shelves to be caused by differences in impurity concentrations. *Miners et al.* (2002) and *Eisen et al.* (2003) included attenuation in modeling studies of englacial reflections, but these studies focused on matching reflections and ice-core data rather than attenuation.

Englacial attenuation is proportional to electrical conductivity. Frequencies typically used to sound deep ice range from 1–300 MHz (e.g., *Gogineni et al.* (1998); *Gades et al.* (2000), *Matsuoka et al.* (2002)) and frequencies less than 10 MHz are particularly well suited to measuring attenuation (*Winebrenner et al.* (2003)). This frequency range is within the ac conductivity "plateau", which is above the Debye dispersion ($\sim$ 0.01 MHz) and below

the low-frequency tail of the infrared resonance that begins at ~ 5 GHz (*Moore and Fujita* (1993)). The high-frequency (0.1–300 MHz) conductivity of ice depends on its impurity concentrations and its temperature.

Observations from Siple Dome, West Antarctica (81.7°S, 148.8°W), provide a unique opportunity to test a model of radar attenuation. Siple Dome has been the site of extensive glaciological investigations, including a 1004-m ice core to the bed (*Gow and Engelhardt* (2000)). A borehole temperature profile and measurements of major-ion concentrations along most of the ice core provide the data necessary to model of attenuation. In addition, *Winebrenner et al.* (2003) used ground-based radar profiles from *Jacobel et al.* (1996) to calculate englacial radar attenuation at Siple Dome. Ice thickness varies by several hundred meters across the dome. Based on assumptions of constant basal reflectivity and depth-averaged attenuation along the radar profiles, they calculated a depth-averaged attenuation rate of 25.9 dB km^{-1}.

Here we use published conductivity measurements to specify a conductivity model that depends on the impurity concentrations and temperature of the ice. We then use depth profiles of major-ion concentrations and temperature as inputs into the ice-conductivity model and calculate an attenuation rate profile for Siple Dome. Finally, we compare the depth-averaged modeled attenuation rate to the value derived from radar profiling data.

2.3 High-Frequency Conductivity of Ice

Methods for measuring the high-frequency conductivity of ice cores, summarized by *Wolff* (2000), include dielectric profiling (DEP; e.g., *Moore et al.* (1992a)), complex conductivity measurements (CCM) and ac electrical conductivity measurements (AC-ECM; e.g., *Sugiyama et al.* (2000)). These measurements are typically made at constant temperature on extracted ice cores. However, the high-frequency conductivity of ice consists of several components that have separate temperature dependencies; measurements of conductivity at a constant temperature are not sufficient to describe the englacial conductivity of ice sheets that are not isothermal. Below we describe a conductivity model that allows for the depth variations of ice chemistry and temperature that are typically observed in ice sheets.

2.3.1 Conductivity Model

The high-frequency conductivity of pure ice is due to the polarization of individual H_2O molecules, ionic defects (H_3O^+ and OH^-) and Bjerrum defects in the presence of an alternating electric field (*Petrenko and Whitworth* (1999)). The high-frequency conductivity of meteoric polar ice is also linearly dependent on its molar concentrations of acid ($[H^+]$), sea-salt chloride ($[\mathrm{ss\,Cl^-}]$) and ammonium ($[NH_4^+]$) (e.g., *Moore and Fujita* (1993); *Petrenko and Whitworth* (1999), *Fujita et al.* (2000)). The conductivity contribution of pure ice and each of these impurities have separate Arrhenius-form temperature dependencies. Conduction mechanisms in ice are not yet fully understood (*Wolff et al.* (1997); *Wolff* (2000)). The H^+ contribution is generally attributed to concentrations of acid in quasi-liquid layers at grain boundaries (*Moore and Fujita* (1993), *Wolff et al.* (1997)), although acids may also be present outside the grain boundaries (*Cullen and Baker* (2001); *Barnes and Wolff* (2004)). The $\mathrm{ss\,Cl^-}$ contribution is probably caused by $\mathrm{ss\,Cl^-}$ ions that form Bjerrum–L defects (*Moore et al.* (1992a); *Moore and Fujita* (1993)), while the ammonium contribution is probably caused by NH_4^+ ions that form Bjerrum–D defects (*Moore et al.* (1994b), *Wolff et al.* (1997)).

We assume that the total conductivity σ at Siple Dome can be represented by an empirical function of the form (e.g., *Corr et al.* (1993)):

$$\begin{aligned}\sigma &= \sigma_{\mathrm{pure}} \exp\left[\frac{E_{\mathrm{pure}}}{k}\left(\frac{1}{T_r}-\frac{1}{T}\right)\right] \\ &\quad +\mu_{\mathrm{H^+}}[\mathrm{H^+}] \exp\left[\frac{E_{\mathrm{H^+}}}{k}\left(\frac{1}{T_r}-\frac{1}{T}\right)\right] \\ &\quad +\mu_{\mathrm{ss\,Cl^-}}[\mathrm{ss\,Cl^-}] \exp\left[\frac{E_{\mathrm{ss\,Cl^-}}}{k}\left(\frac{1}{T_r}-\frac{1}{T}\right)\right], \end{aligned} \tag{2.1}$$

where σ_{pure} is the pure ice conductivity, $\mu_{\mathrm{H^+}}$ and $\mu_{\mathrm{ss\,Cl^-}}$ are molar conductivities, E_{pure}, $E_{\mathrm{H^+}}$ and $E_{\mathrm{ss\,Cl^-}}$ are activation energies, k is Boltzmann's constant, T is temperature in Kelvin and $T_r = 251$ K is a reference temperature.

Although $[NH_4^+]$ is high in Greenland, it is generally small in meteoric ice in Antarctica (*Legrand and Mayewski* (1997)). Measurements from the 150-m 1994 Siple Dome core indicate that the mean value of $[NH_4^+]$ is only 0.13 μM (*Mayewski et al.* (1995)), where M $= \mathrm{mol\,L^{-1}}$. *Moore et al.* (1994b) found that the molar conductivity of NH_4^+ at $-15°$C is 1.0

$S\,m^{-1}M^{-1}$. At Siple Dome, the product of $[NH_4^+]$ and its molar conductivity is generally more than an order of magnitude smaller than that for H^+ or ss Cl^-, so we ignore its contribution to conductivity in this study.

Conductivity increases with firn density but its density dependence is not yet well known (*Barnes et al.* (2002)). In the upper firn layer, we correct each conductivity component in (2.1) for density using a conductivity–density model suggested by *Barnes et al.* (2002), which includes a Looyenga mixing model for the pure ice and ss Cl^- components and a percolation model for the H^+ component. While *Barnes et al.* (2002) focused on the conductivity–density relationship of H_2SO_4, we assume that the percolation model is valid for all acids (section 2.3.3).

2.3.2 Synthesis of Experimental Data

Reported dielectric properties

Table 2.1 shows reported experimental values for each of the dielectric properties in (2.1) and the mean and standard deviation of each dielectric property. Here we use the mean and standard deviation of the dielectric properties to calculate the total conductivity and its uncertainty. References given in Table 2.1 are those that originally reported the measurements; the footnotes discuss any adjustments that have been made to the original reported values. Activation energies in Table 2.1 are only reported from experiments that measured conductivity over a range of temperatures.

Several conductivity experiments are not reported in Table 2.1. We do not use values of the pure ice dielectric properties derived from experiments at microwave frequencies because those data may be affected by the low-frequency tail of the infrared resonances. We include dielectric properties of the H^+ component from microwave experiments because it is not dispersive, but we exclude microwave dielectric properties of the ss Cl^- component because it is dispersive (*Moore and Fujita* (1993)). Temperature-dependent phenomena present at microwave frequencies may also be present at radar frequencies and are considered in section 2.7.2 and section 2.7.2.

Figure 2.1 shows the contributions of pure ice, H^+ and ss Cl^- components to the con-

Table 2.1a: Observed, mean and standard deviation of the dielectric properties used in the conductivity model given in (2.1). The reference temperature used throughout this table and study is 251 K; values reported at a different reference temperature were adjusted to our reference temperature using the mean activation energies. References are: 1. *Camplin and Glen* (1973); 2. *Johari and Charette* (1975); 3. *Takei and Maeno* (1987); 4. *Moore et al.* (1989); 5. *Fujita et al.* (1992); 6. *Moore et al.* (1992a); 7. *Moore et al.* (1992b); 8. *Moore et al.* (1994b); 9. *Matsuoka et al.* (1996); 10. *Matsuoka et al.* (1997a); 11. *Sugiyama et al.* (2000); 12. *Barnes et al.* (2002). Footnotes are shown in Tables 2.1b and 2.1c. Reasons for values in parentheses are explained in their respective footnotes.

Ref. #	Ice type	Temp. (K)	Freq. (MHz)	E_{pure} (eV)	$E_{\mathrm{H+}}$ (eV)	$E_{\mathrm{ss\,Cl-}}$ (eV)	σ_{pure} ($\mu\mathrm{S\,m^{-1}}$)	$\mu_{\mathrm{H+}}$ ($\mathrm{S\,m^{-1}M^{-1}}$)	$\mu_{\mathrm{ss\,Cl-}}$ ($\mathrm{S\,m^{-1}M^{-1}}$)
1	Lab-grown pure	225–265	0.02	0.61	—	—	4.5	—	—
2	Lab-grown pure	248–272	35–60	0.51 ± 0.01 [a]	—	—	9.2 ± 0.2 [b]	—	—
3	Lab-grown pure	123–263	0.1	0.585 ± 0.024	—	—	—	—	—
4	Ice core	251	0.1	—	—	—	(12.7 ± 0.3) [b]	2.57 ± 0.09 [c]	0.43 ± 0.01 [d]
5	Lab-grown doped	243–268	9700	—	0.195	—	—	3.5 ± 0.3	—
6	Ice core	203–273	0.3	—	0.26 ± 0.03	0.19 ± 0.02	—	—	—
7	Ice core	251	0.3	—	—	—	(6.1 ± 0.6) [e]	3.66 ± 0.16 [f]	—
8	Ice core	258	0.3	—	—	—	—	3.5 ± 0.5 [g]	—
9	Lab-grown doped	240–264	0.1–5	0.51 ± 0.01 [h]	0.20 ± 0.01	—	6.0 ± 0.1 [h]	2.3 ± 1.0	—
10	Lab-grown doped	193–271	5000	—	0.16 [i]	—	—	3.0 [j]	—
11	Ice core	253	1	—	—	—	—	3.1 ± 0.7	—
12	Ice core	258	0.1	—	—	—	(4.9 ± 1.0) [e]	3.8 [k]	(1.0) [l]
	Mean and standard deviation			0.55 ± 0.05	0.20 ± 0.04	0.19 ± 0.02	(7.2 ± 3.1) [m] 6.6 ± 2.4 [n]	3.2 ± 0.5	0.43 ± 0.07 [o]

Table 2.1b: Footnotes for Table 2.1a.

Label	Footnote
a	Calculated using a non-linear least-squares fit to the single crystal data at 35 and 60 MHz from Figures 2 and 3 in *Johari and Charette* (1975); uncertainties given are the 99% confidence bounds on this fit and the fraction of explained variance is 0.97.
b	*Corr et al.* (1993) argued that organic acids contributed 8 $\mu S\,m^{-1}$ to the constant value of the DEP regression reported by *Moore et al.* (1989). However, *Moore et al.* (1989) reported "very good agreement" between $[H^+]$ values from acid titration measurements and those calculated from a charge balance that did not include organic acids, so it is unlikely that large concentrations of organic acids altered the impurity concentrations used in their DEP regression (section 2.4.2). The reported constant value of the DEP regression is interpreted as σ_{pure} but ignored in the calculation of its mean and standard deviation.
c	Value adjusted from 1.43 ± 0.05 $S\,m^{-1}M^{-1}$ by *Moore and Fujita* (1993), who re-evaluated the values of $[H^+]$ used by considering the "effective" $[H^+]$ of H_2SO_4 in the ice (section 2.3.3).
d	Value adjusted from 0.39 ± 0.01 $S\,m^{-1}M^{-1}$ by *Moore et al.* (1992a), who converted μ_{salt} to $\mu_{\text{ss Cl}^-}$.
e	The reported constant value of the DEP regression is interpreted as σ_{pure} but ignored in the calculation of its mean and standard deviation.
f	Value adjusted from 1.83 ± 0.08 $S\,m^{-1}M^{-1}$ by *Moore and Fujita* (1993), who converted the reported value to $\mu_{H_2SO_4}$. Their value for $\mu_{H_2SO_4}$ is reported here as μ_{H^+} (section 2.3.3).
g	Mean and standard deviation of four values reported for four separate depth ranges in the GRIP core.
h	Calculated using a non-linear least-squares fit to the mean conductivity of two pure ice samples between 0.5 and 1.0 MHz; uncertainties given are the 99% confidence bounds on this fit and the fraction of explained variance is 0.98.
i	Mean of values of $E_{H_2SO_4}$ and E_{HCl}.
j	Mean of values of $\mu_{H_2SO_4}$ and μ_{HCl}.
k	*Barnes et al.* (2002) reported values for the molar conductivities of H_2SO_4 and HCl, but H_2SO_4 was the dominant impurity. Their value for $\mu_{H_2SO_4}$ is reported here as μ_{H^+} (section 2.3.3).
l	*Barnes et al.* (2002) stated that their value for $\mu_{\text{ss Cl}^-}$ is not "well established" because $[Na^+]$ is anti-correlated with the measured acid species. Therefore, we do not use this value when calculating the mean and standard deviation of $\mu_{\text{ss Cl}^-}$.

Table 2.1c: Footnotes for Table 2.1a (continued).

Label	Footnote
m	Calculated using all reported values of σ_{pure}.
n	We interpreted the constant values from DEP regression as σ_{pure} (refs. 4, 7 and 12). However, these values may include contributions from unknown chemical species that contribute to the conductivity measured by DEP. Thus, these values may overestimate σ_{pure} and we do not include them in this preferred calculation of its mean and standard deviation.
o	The uncertainties for the dielectric properties reported by *Moore et al.* (1989) are small relative to the reported range of values, so in the absence of additional reliable values for $\mu_{\text{ss Cl}-}$ we note their reported uncertainty for $\mu_{\text{ss Cl}-}$ ($0.01\ \text{S m}^{-1}\text{M}^{-1}$) is likely an underestimate of its true uncertainty and assign $\mu_{\text{ss Cl}-}$ the same relative uncertainty as $\mu_{\text{H}+}$ (16%).

ductivity model given in (2.1) for a typical range of ice-sheet temperatures. The values for $[\text{H}^+]$ and $[\text{ss Cl}^-]$ used in Figure 2.1 are the mean values at Siple Dome (section 2.6.1). This figure shows that the pure ice component of conductivity dominates the total conductivity as the temperature approaches the melting point.

Evans (1965) reported conductivity measurements made by Westphal on Greenland ice at frequencies from 150 MHz to 2.7 GHz. The Westphal data appear to be the source for the temperature–attenuation relationship at 150 MHz given by *Gudmandsen* (1971). However, the impurity concentrations of the samples used by Westphal are unknown (*Moore and Fujita* (1993)) and therefore these measurements are not included in Table 2.1. The temperature–attenuation relationship given by *Gudmandsen* (1971) can be described using a non-linear least-squares fit to a single-term conductivity model of the form:

$$\sigma = \sigma_0 \exp\left[\frac{E_0}{k}\left(\frac{1}{T_r} - \frac{1}{T}\right)\right], \tag{2.2}$$

where $\sigma_0 = 15.4 \pm 1.4\ \mu\text{S m}^{-1}$ and $E_0 = 0.33 \pm 0.03$ eV. The uncertainties are the 99% confidence intervals, which are a measure of the precision of the fit rather than the accuracy of the *Gudmandsen* (1971) relationship, which is not known. By subtracting the pure ice term in (2.1) from the fit to the *Gudmandsen* (1971) relationship, we can match that fit if the ice contains either 2.0 ± 1.2 μM of $[\text{H}^+]$ or 15.0 ± 8.2 μM of $[\text{ss Cl}^-]$, or a combination of lower concentrations of those impurities. However, the ice from which the *Gudmandsen*

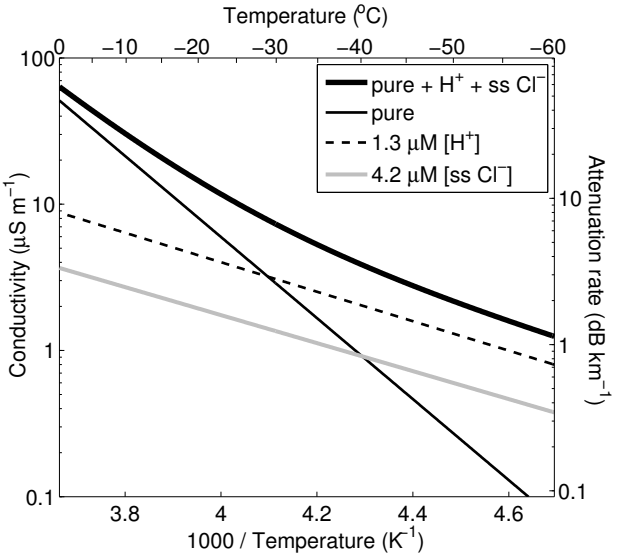

Figure 2.1: Contributions of pure ice, H^+ and ss Cl^- components to the conductivity of ice as a function of inverse temperature. Values for $[H^+]$ and [ss Cl^-] are the mean values for Siple Dome (data discussed in section 2.6.1). For these concentrations, the pure ice component dominates the total conductivity at temperatures higher than $\sim -30°C$; higher impurity concentrations raise the temperature at which the pure ice component dominates. Equivalent attenuation rates are calculated using (2.10).

(1971) relationship was derived is from Greenland, where NH_4^+ may also be an important impurity.

The mean temperature–conductivity relationship at Siple Dome, calculated using (2.1) and the mean values for $[H^+]$ and $[ss\,Cl^-]$, is well approximated by (2.2) using $\sigma_0 = 12.7 \pm 0.6$ $\mu S\,m^{-1}$ and $E_0 = 0.42 \pm 0.02$ eV. The differences between these best-fit values and those for the *Gudmandsen* (1971) relationship indicate the effect of different impurity concentrations on the temperature–conductivity relationship. A single temperature–conductivity relationship like (2.2) cannot capture the effect of separate temperature dependencies from distinct impurities. We therefore consider the *Gudmandsen* (1971) relationship inadequate for modeling conductivity versus depth, and thus attenuation, at Siple Dome.

Model mean and uncertainty

We calculate the mean and standard deviation of measurements of the dielectric properties in (2.1) shown in Table 2.1 and ignore the reported experimental uncertainties in these calculations. We considered calculating values of the mean and uncertainty that are weighted by the uncertainties of the reported values (*Bevington* (1969)), but the reported uncertainties of most of the values in Table 2.1 are significantly smaller than the range of reported values for each dielectric property. Assuming that the same conduction mechanisms are present in all of the ice samples used in Table 2.1, this discrepancy suggests that most of the reported uncertainties in Table 2.1 underestimate the true uncertainty in their respective dielectric properties. However, recent work suggests that the conduction mechanism for different impurities also depends on both impurity concentration and grain structure of the ice (*Barnes and Wolff* (2004)). This potential variability in the conduction mechanism may explain the large range of reported values of some of the H^+ and ss Cl^- dielectric properties.

Uncertainties in $[H^+]$ and $[ss\,Cl^-]$ also affect uncertainty in the conductivity. The measurement uncertainties of the major-ion data are small, but we assign a constant uncertainty of 0.5 μM to the calculated values of $[H^+]$ and $[ss\,Cl^-]$ (section 2.4.2). We assume that the dielectric properties do not covary and calculate the uncertainty in the total conductivity $\widetilde{\sigma}$

using standard error propagation techniques:

$$\widetilde{\sigma} = \sqrt{\sum_{j=1}^{8} \widetilde{p}_j^2 \left(\frac{\partial \sigma}{\partial p_j} \right)^2}, \tag{2.3}$$

where p_j includes the six dielectric properties and two impurity concentrations, $\widetilde{p}_j$ is the standard deviation for the dielectric property (Table 2.1) or impurity concentration uncertainty (0.5 μM) and σ is the total conductivity given by (2.1). We report all uncertainties as $\pm 1\widetilde{\sigma}$.

Uncertainty in the activation energies affects the temperature dependence of the conductivity model, whereas uncertainty in the molar conductivities affects the impurity-concentration dependence. The relative uncertainty in the total conductivity ($\widetilde{\sigma}/\sigma$) depends on the impurity concentrations and temperature. Values for $\widetilde{\sigma}/\sigma$, calculated using the depth profiles of impurity concentrations and temperature at Siple Dome (section 2.6.1), range from 17–34%; the mean value is 27%.

Because of the non-linearity of (2.3), it is not possible to evaluate the contribution of each dielectric property or impurity concentration to $\widetilde{\sigma}/\sigma$ independent of the contributions of the other dielectric properties and impurity concentrations. However, σ_{pure} has the largest contribution to the uncertainty in the conductivity model. Assuming that σ_{pure} is error-free, we set its standard deviation to zero and find that the mean value of $\widetilde{\sigma}/\sigma$ decreases to 13%. Using the same assumption for E_{pure}, the mean value of $\widetilde{\sigma}/\sigma$ decreases to 26%, for $[H^+]$ it decreases to 25% and for the remaining dielectric properties and $[\text{ss}\,Cl^-]$ it decreases by less than 1%. Thus, reduction in the uncertainty in σ_{pure} most effectively reduces uncertainty in the conductivity model.

2.3.3 Model Simplifications

Conductivity dispersions

There is no evidence for significant dispersions in the H^+ component of conductivity in the high-frequency range but there is some evidence that the ss Cl^- component of conductivity is dispersive, although its dispersion is not well quantified (*Moore and Fujita* (1993)). *Fujita et al.* (2000) showed the frequency independence of the pure ice component of conductivity

at frequencies below 300 MHz, which they calculated using an empirical relationship for conductivity at the high-frequency tail of the Debye relaxation and the low-frequency tail of the infrared resonance. Here we ignore possible conductivity dispersions and assume that the conductivity model is valid for the entire high-frequency range (0.1–300 MHz).

Conductivity of different acids

Several studies have found that μ_{H^+} is dependent on the acid species present (*Matsuoka et al.* (1997a), *Fujita et al.* (2000); *Barnes et al.* (2002)). Using DEP, *Barnes et al.* (2002) found that different acids have slightly different molar conductivities: $\mu_{H_2SO_4} = 3.8\ \mathrm{S\,m^{-1}M^{-1}}$ and $\mu_{HCl} = 3.5\ \mathrm{S\,m^{-1}M^{-1}}$, adjusted to $-22°\mathrm{C}$ using $E_{H^+} = 0.20$ eV. The difference between these two values of $\mu_{H_2SO_4}$ and μ_{HCl} ($0.3\ \mathrm{S\,m^{-1}M^{-1}}$) is smaller than the standard deviation of μ_{H^+} in Table 2.1 ($0.5\ \mathrm{S\,m^{-1}M^{-1}}$). In meteoric polar ice, H_2SO_4 is often concentrated at grain boundaries (*Mulvaney et al.* (1988); *Barnes and Wolff* (2004)) where only a single H^+ ion is dissociated from H_2SO_4 (*Wolff and Paren* (1984), *Moore and Fujita* (1993); *Fukazawa et al.* (1998)). Hence, its molar conductivity is similar to HCl and HNO_3, which are the other major acids in polar ice. Here we assign the same molar conductivity to all acid species.

2.4 Impurity Concentrations From Major-Ion Chemistry

Soluble major-ion concentrations are usually measured in meltwater samples taken from ice cores using ion chromatography. $[H^+]$ cannot be directly measured by ion chromatography but it can be estimated using the charge balance of major ions (e.g., *Legrand and Mayewski* (1997)). $[\mathrm{ss\,Cl^-}]$ is determined using ion chromatography data to separate $[Cl^-]$ into sea-salt and excess components.

2.4.1 [ss Cl^-]

The total concentration of each ion [X] can be separated into a sum of its sea-salt ($[\mathrm{ss\,X}]$) and excess, non-sea-salt ($[\mathrm{xs\,X}]$) components:

$$[\mathrm{X}] = [\mathrm{ss\,X}] + [\mathrm{xs\,X}]. \tag{2.4}$$

It is convenient to represent [ss X] relative to a reference marine ion and a coefficient F_X:

$$F_X = \frac{[\text{ss X}]}{[\text{ss Na}^+]}, \tag{2.5}$$

where F_X is the ratio of the molalities of X to Na^+ in seawater, which are given by *Holland* (1978). The molality ratios of X to any single ion could be used, but Na^+ is the preferred reference marine ion (*Legrand and Delmas* (1988)).

[ss Na^+] is determined using a conservative ion method similar to that described by *Dixon et al.* (2004). The concentration [X] of each ion in a meltwater sample can be used to estimate [ss Na^+] by setting [ss X] = [X] in (2.5). [ss Na^+] for the sample is taken to be the smallest value of [ss Na^+] calculated in this way:

$$[\text{ss Na}^+] = \min\left(\frac{[\text{X}]}{F_X}\right). \tag{2.6}$$

This method ensures non-negative values for [xs X]. The combination of (2.4), (2.5) and (2.6) is used to calculate [ss Cl^-], [ss SO_4^{2-}] and [xs SO_4^{2-}].

The conservative ion method assumes that the values of F_X for seawater are valid for the sea salts deposited on the ice sheet. Recent work has shown that frost flowers are also an important source of sea-salt aerosol in Antarctica (e.g., *Rankin et al.* (2004)). Compared to seawater, [SO_4^{2-}] is depleted by $\sim 67\%$ in frost flowers and [Na^+] is depleted by $\sim 10\%$ (*Rankin et al.* (2000)). Hence, F_{SO_4} for sea salt that originated from frost flowers is less than that for seawater; [xs SO_4^{2-}] may be underestimated if F_{SO_4} is simply assumed to be the seawater ratio. Although depletion of [Na^+] in frost flowers affects all values of F_X, the amount of depletion is small and we do not adjust F_X for possible [Na^+] depletion.

For the top 22 m of the 1994 Siple Dome core, *Rankin et al.* (2004) estimated that at least 43% of the total sea salt input in the past $\sim$ 100 a at Siple Dome came from frost flowers. Here we assume that this ratio of frost flower to sea-spray salt is valid for the entire ice thickness and treat F_{SO_4} as $(0.43 \cdot (1 - 0.67)) + (1 - 0.43) = 71\%$ of its seawater value for the entire Siple Dome record. The overall effect on [H^+] is small (section 2.4.2): accounting for the effect of frost flowers decreases the mean estimate of [H^+] by less than 0.06 μM.

2.4.2 [H$^+$]

The charge balance for melted ice samples using molar concentrations is (*Legrand and Mayewski* (1997)):

$$\begin{aligned} 2\,[Ca^{2+}] + [H^+] + [K^+] + \\ 2\,[Mg^{2+}] + [Na^+] + [NH_4^+] \end{aligned} = \begin{aligned} &[CH_3COO^-] + [CH_3SO_3^-] + \\ &[Cl^-] + [F^-] + [HCOO^-] + \\ &[NO_3^-] + 2\,[SO_4^{2-}]. \end{aligned} \tag{2.7}$$

The ions present in an ice sheet depend on location. For example, $[NH_4^+]$ and several organic acids contribute to the charge balance in Greenland (e.g., *Legrand and de Angelis* (1996)), but in Antarctica, concentrations of $[F^-]$ and most of the organic acids except $[CH_3SO_3^-]$ are either very low or undetectable (*Legrand et al.* (1988); *Legrand and Mayewski* (1997)). Although $[NH_4^+]$ was detected in the earlier shallow Siple Dome core (*Mayewski et al.* (1995)), it was either low or undetectable in subsequent measurements on the main core.

The charge balance in (2.7) applies to meltwater samples, but in ice, H_2SO_4 is only singly dissociated into H^+ and HSO_4^- at the grain boundaries (section 2.3.3). To apply the charge balance calculated in meltwater to a charge balance in ice, we separate $[SO_4^{2-}]$ into its sea-salt and excess contributions using (2.4). We assume that the crustal contribution to $[SO_4^{2-}]$ is negligible (*Castellano et al.* (2004)) and that all $[xs\,SO_4^{2-}]$ is associated with H_2SO_4 and thus substitute $2\,[SO_4^{2-}]$ measured in meltwater with $2\,[ss\,SO_4^{2-}] + [xs\,SO_4^{2-}]$.

For application to the Siple Dome ice core, we ignore undetected ions ($[CH_3COO^-]$, $[F^-]$, $[HCOO^-]$, $[NH_4^+]$), apply the above substitution for $[SO_4^{2-}]$ and rearrange (2.7) to calculate $[H^+]$:

$$\begin{aligned} [H^+] \;=\; & [Cl^-] + [NO_3^-] + 2\,[ss\,SO_4^{2-}] + [xs\,SO_4^{2-}] \\ & + [CH_3SO_3^-] - 2\,[Ca^{2+}] - [K^+] \\ & - 2\,[Mg^{2+}] - [Na^+]. \end{aligned} \tag{2.8}$$

Because $(2\,[ss\,SO_4^{2-}] + [xs\,SO_4^{2-}]) < 2\,[SO_4^{2-}]$, $[H^+]$ calculated using (2.8) can be negative. Negative values of $[H^+]$, which occurred for less than 6% of all samples from Siple Dome, are set to zero.

Generally, the sum of the major ions detected by ion chromatography is charge-balanced to within the precision of the measurements. *Legrand and de Angelis* (1996) compared a calculation of $[H^+]$ using a charge balance to direct measurements of $[H^+]$ using acid titration for ice from Summit, Greenland. They found imbalances equivalent to 2–25% of the measured $[H^+]$. *Legrand and Delmas* (1988); *Moore et al.* (1989) and *Moore et al.* (1992b) also found good agreement between $[H^+]$ calculated from charge balances and acid titration measurements. We assume that the uncertainty in the charge-balance calculation of $[H^+]$ is 0.5 μM, which is similar to previously reported differences between $[H^+]$ calculated using charge balances and acid titration measurements. Because no other independent method exists for measuring $[\mathrm{ss}\,Cl^-]$, we assign it the same uncertainty as for $[H^+]$.

2.5 Depth-averaged Attenuation

The attenuation length L_a is the e–folding length of radar power attenuation and it is inversely proportional to the high-frequency conductivity of ice (e.g., *Jackson* (1975)):

$$L_a = \frac{\varepsilon_0 \sqrt{\varepsilon'_r} c}{\sigma}, \tag{2.9}$$

where ε_0 is the permittivity of free space, ε'_r is the real part of the relative permittivity of ice and c is the speed of light in the vacuum.

ε'_r depends on ice temperature, impurity concentrations and frequency, although these dependencies are weaker than those for conductivity. ε'_r of pure ice decreases less than 2% from 1 MHz to 39 GHz (*Matsuoka et al.* (1997b)) and increases $\sim 1\%$ from $-80°C$ to $-5°C$ at microwave frequencies (*Matsuoka et al.* (1997a)). The effect of $[H^+]$ on ε'_r is larger at lower frequencies and higher temperatures (*Fujita et al.* (2000)). *Matsuoka et al.* (1996) estimated that ε'_r at $-10°C$ would increase by 3% and 2% at 2 MHz and 10 MHz, respectively, for an $[H^+]$ increase of 10 μM. Overall, for the temperature range -40 to $-10°C$ and the impurity range 0 to 10 μM, ε'_r is 3.23 at 2 MHz and 3.20 at 10 MHz. Here we use $\varepsilon'_r = 3.22$ and assume that it is independent of temperature, impurity concentration and frequency within the range of 0.1–300 MHz.

It is often more convenient to describe radar attenuation in an ice sheet in terms of a

one-way attenuation rate N_a:

$$N_a = \frac{1000(10 \log_{10} \mathrm{e})}{L_a} \approx 0.912\,\sigma, \tag{2.10}$$

where N_a is in $\mathrm{dB\,km^{-1}}$, L_a is in m and σ is in $\mu\mathrm{S\,m^{-1}}$ (*Winebrenner et al.* (2003)).

For the frequency range of the traverse data used at Siple Dome (3–5 MHz), the transmitted power into the ice sheet was reduced mainly by attenuation by dielectric absorption and geometric spreading. Appendix A shows that power losses from reflections at internal layers are negligible in this frequency range. Losses from birefringence are also negligible in this frequency range (*Fujita et al.* (2006)) and losses from volume scattering are expected to be small in crevasse-free regions since the wavelengths in ice (35–55 m) of this frequency range are larger than the size of volume scatterers. Hence we ignore power losses from reflections at internal layers, birefringence and volume scattering.

Radar-derived estimates of attenuation give the depth-averaged attenuation to a reflector. To compare our modeled attenuation at Siple Dome with the radar-derived attenuation (*Winebrenner et al.* (2003)), we calculate the depth-averaged modeled attenuation rate N_a^*. The power loss due to attenuation within a depth increment Δz_i in the ice column is simply $N_a(\Delta z_i) \cdot \Delta z_i$. The depth-averaged attenuation rate to a reflector at a depth z over m discrete depth increments is:

$$N_a^*(z) = \frac{1}{z} \sum_{i=1}^{m} N_a(\Delta z_i) \cdot \Delta z_i, \tag{2.11}$$

Δz_i is determined by the sampling intervals of the measurements of impurity concentrations and temperature, which are treated as constant across Δz_i.

2.6 Application to Siple Dome

2.6.1 Borehole and Ice-core Data

The temperature profile down the 1004-m borehole was measured using the same system described by *Clow et al.* (1996). The basal temperature is -2.35°C. Depth intervals of borehole temperature measurements range from 0.093–0.102 m and the mean depth interval is less than 0.10 m. J. Fitzpatrick (pers. comm., 2006) provided the measurements of density along the Siple Dome core.

Concentrations of major ions ($[Ca^{2+}]$, $[Cl^-]$, $[K^+]$, $[Mg^{2+}]$, $[Na^+]$, $[NO_3^-]$, $[SO_4^{2-}]$) were measured using ion chromatography on the upper 974 m of the ice core. Depth intervals of major-ion samples range from 0.003–1.58 m and the mean depth interval is 0.21 ± 0.10 m. $[CH_3SO_3^-]$ was measured separately at about the same depth intervals (*Saltzman et al.* (2006)).

Ion chromatography measurements in the depth range 974–1004 m are not available. Visually, this basal ice appears to be clean and debris-free (*Gow and Engelhardt* (2000)), so we assume that the impurity concentrations in this ice are the same as the mean concentrations in the adjacent 30-m interval (944–974 m). The mean value of $[H^+]$ for this depth range is 1.1 μM and the mean value of $[ss\,Cl^-]$ is 4.5 μM. While this approximation is not ideal, accurate knowledge of $[H^+]$ and $[ss\,Cl^-]$ within this depth range is not too critical because temperatures near $-3°C$ at the bed imply that attenuation there is dominated by the pure ice contribution (Figure 2.1).

Electrical conductivity measurements (ECM) and CCM measurements were also made along most of the core (e.g., *Taylor and Alley* (2004)) but these measurements were not calibrated with direct measurements of $[H^+]$ using acid titration. Relationships between these electrical data and our calculated $[H^+]$ and $[ss\,Cl^-]$ profiles are discussed in Appendix B.

2.6.2 Modeled Attenuation at the Ice-core Site

Measurements discussed in section 2.6.1 were made at varying depth intervals. We spatially average the measurements of temperature, density and impurity concentrations. Figure 2.2 shows the impurity concentrations and temperature at 10-m intervals. The density profile is not shown, but it is used to correct ε_r' in (2.9) for its density dependence using Looyenga's dielectric mixing equation (*Kovacs et al.* (1995)) and also to correct σ in (2.1) for its density dependence (section 2.3.1).

The conductivity profile is calculated using (2.1) and converted into an attenuation rate profile using (2.10). Figure 2.3 shows the contributions of the pure ice, H^+ and $ss\,Cl^-$ components to the attenuation rate profile. As temperature increases with depth, so does

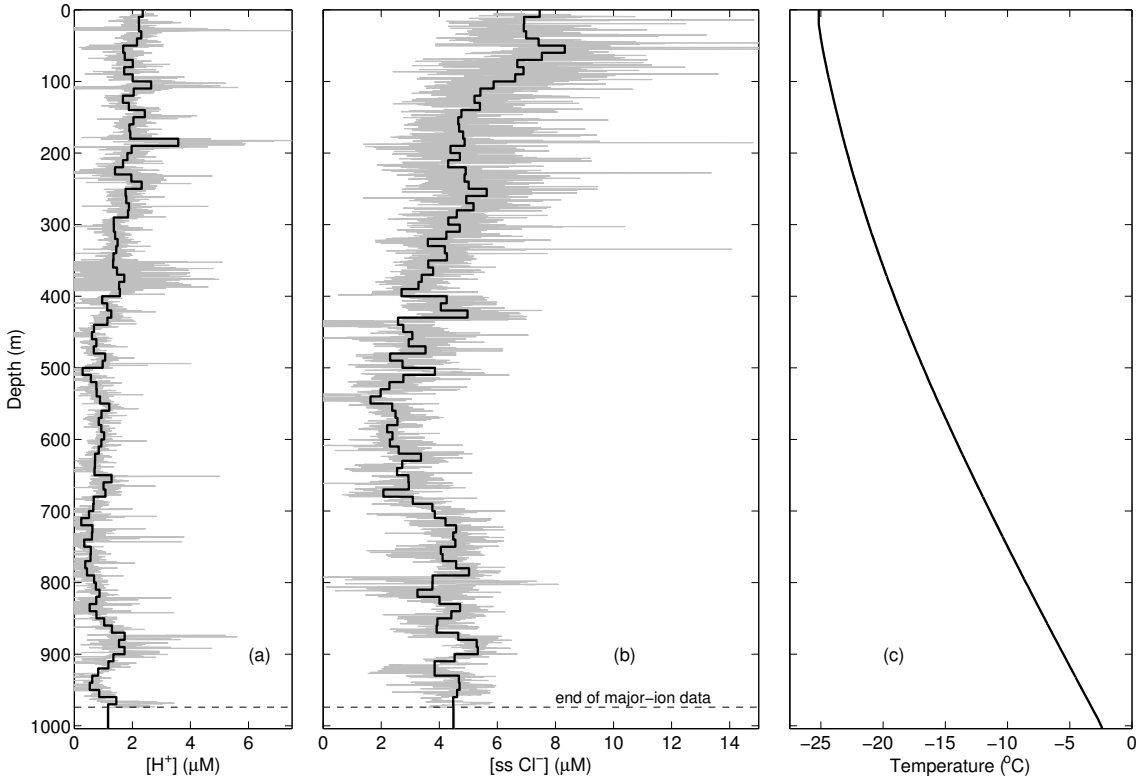

Figure 2.2: Siple Dome ice-core and borehole data used to model attenuation. (a) $[H^+]$ profile calculated using (2.8). (b) $[\mathrm{ss}\,Cl^-]$ profile calculated using (2.5). For (a) and (b), the concentration axes are at the same scale, the gray lines are the raw profiles, the black lines are the data averaged at 10-m intervals and the horizontal dashed line represents the largest depth for which major-ion data are available (974 m). (c) Measured temperature profile.

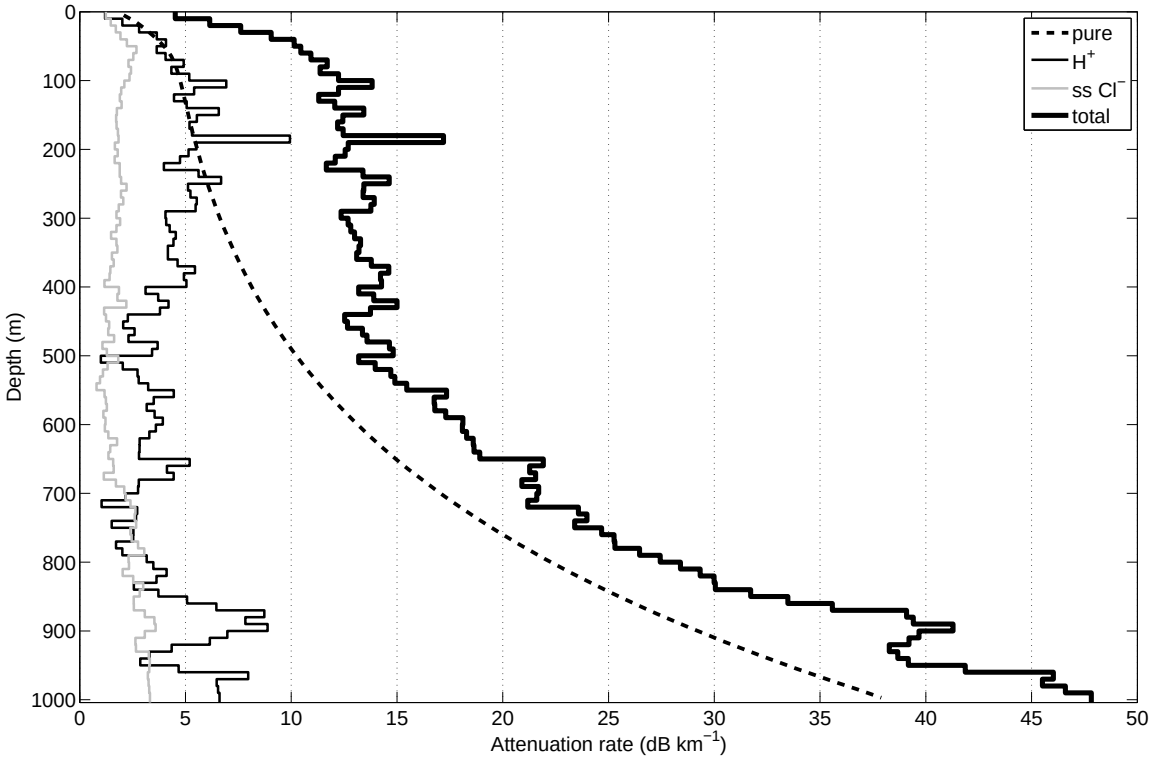

Figure 2.3: Contribution of pure ice, H^+ and ss Cl^- components to the modeled attenuation rate profile (N_a) at Siple Dome. At the bed, the depth-averaged modeled attenuation rate (N_a^*), calculated from (2.11), is 20.0 ± 5.7 dB km^{-1}.

the attenuation rate. At temperatures higher than $\sim -23°$C (depths greater than ~ 200 m), the pure ice component of the attenuation exceeds the H^+ and ss Cl^- components and begins to dominate the attenuation rate profile. However, even at depths below ~ 200 m, depth variations in impurity concentrations can still produce changes in the total attenuation rate profile. At the bed, the depth-averaged modeled attenuation rate at the ice-core site is 20.0 ± 5.7 dB km^{-1}. If the H^+ and ss Cl^- components of the conductivity model are ignored in this calculation, the modeled attenuation rate decreases to 13.7 ± 5.3 dB km^{-1}; this result emphasizes the importance of impurity concentration data for modeling attenuation.

Figure 2.4 shows the depth-averaged modeled attenuation rate profile (N_a^*) at Siple Dome. The value of this profile at the bed is the same as the depth-normalized attenuation rate using the entire total attenuation rate profile (N_a) shown in Figure 2.3. The depth-

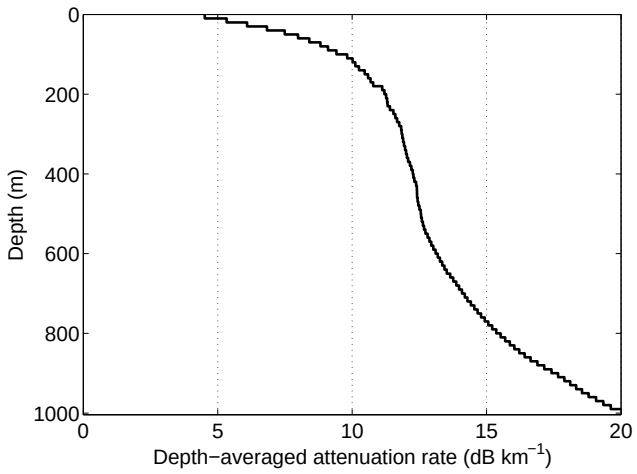

Figure 2.4: Depth-averaged modeled attenuation rate profile (N_a^*) at Siple Dome calculated using (2.11) at all depths.

averaged attenuation rate does not respond quickly to changes in the total attenuation rate because it is an average of the total attenuation rate profile between the surface and any given depth. Hence, the depth-averaged attenuation rate profile is not strongly influenced by rapid changes in the contribution of attenuation from impurities, but it is primarily influenced by the temperature profile.

2.6.3 Radar-derived Attenuation

The depth-averaged modeled attenuation rate can be compared to that derived from radar measurements. *Winebrenner et al.* (2003) calculated the depth-averaged attenuation rate at Siple Dome using two different methods. Using common midpoint data, where the transmitting and receiving antennae are progressively separated from a fixed midpoint, they examined the relationship between basal echo intensity and the radar path length through the ice and calculated an attenuation rate of 35.0 dB km^{-1} at a location $\sim$ 4 km southeast of the ice divide. However, the common midpoint data were not corrected for the angular dependence of the beam pattern, which is important (e.g., *Arcone* (1995)) but not known for the system used to the make the measurements. Because of this uncertainty, we do not use the attenuation rate derived from the common-midpoint method.

Using data from a 125 km traverse across the ice divide, *Winebrenner et al.* (2003) calculated an attenuation rate of 25.9 dB km^{-1}. This required the assumption that the basal reflectivity and the depth-averaged attenuation rate were constant across the traverse. We suspect that those assumptions are not valid far to the north of the ice divide. Beyond 54 km north, the radar traverse crosses into the relict Siple Ice Stream, where the bed reflection powers (BRPs) are much higher, indicating a different basal condition than that under most of Siple Dome (*Gades et al.* (2000)). Here we restrict the attenuation calculation to data within 54 km both north and south of the ice divide. We have made several adjustments to the traverse method presented by *Winebrenner et al.* (2003), which are explained in Appendix C. The updated radar-derived depth-averaged attenuation rate is 25.3 ± 1.1 dB km^{-1}.

Radar-derived attenuation rates to several reflectors could constrain the depth-averaged attenuation rate profile and provide additional tests for the attenuation model. However, the calculation of attenuation rates using internal reflections requires bright, isolated reflectors, which are uncommon at radar frequencies less than 10 MHz (e.g., *Jacobel and Welch* (2005)). Here we only use the basal reflector because we could not calculate reliable attenuation rates using internal reflections at Siple Dome.

2.7 Discussion

In section 2.6.2, we presented the modeled depth-averaged attenuation rate at Siple Dome using our standard conductivity model from Table 2.1. In the following two subsections, we consider adjustments to the conductivity model that may explain the difference between the modeled and radar-derived attenuation rates.

2.7.1 Matching Modeled and Radar-derived Attenuation

Here we assume that the radar-derived attenuation rate at Siple Dome is correct and adjust each dielectric property and impurity concentration in (2.1) to match the modeled and radar-derived attenuation rates. Each adjustment is made separately while keeping the other dielectric properties and impurity concentrations at their original values; these results are shown in Table 2.2. For [H^+], [ss Cl^-] and the dielectric properties associated with these

Table 2.2: Separate adjustments to the mean values of the dielectric properties and impurity concentrations in (2.1) that are necessary to match the modeled and radar-derived attenuation at Siple Dome.

Parameter	Units	Original value	Adjusted value (% increase)
E_{pure}	eV	0.55	0.71 (29%)
$E_{\text{H+}}$	eV	0.20	0.72 (260%)
$E_{\text{ss Cl}^-}$	eV	0.19	0.87 (358%)
σ_{pure}	$\mu\text{S m}^{-1}$	6.6	9.1 (38%)
$\mu_{\text{H+}}$	$\text{S m}^{-1}\text{M}^{-1}$	3.2	7.2 (125%)
$\mu_{\text{ss Cl}^-}$	$\text{S m}^{-1}\text{M}^{-1}$	0.43	1.56 (263%)
$[\text{H}^+]$	μM	1.3	2.7 (108%)
$[\text{ss Cl}^-]$	μM	4.2	15.0 (257%)

Each original value is adjusted separately while the other dielectric properties and impurity concentrations are kept at their original values. The original mean impurity concentrations shown here are for the 10-m averaged data. Also, these adjustments are implemented at all temperatures rather than a specific temperature range, which is considered for $E_{\text{H+}}$ in section 2.7.2.

impurities, large adjustments relative to their original values are necessary to match the modeled and radar-derived values; smaller relative adjustments are needed for the pure ice dielectric properties.

For the englacial temperatures present at Siple Dome, the dominance of the pure ice contribution to attenuation (Figure 2.3) is consistent with the higher sensitivity of the depth-averaged modeled attenuation rate to the pure ice dielectric properties (Figure 2.1). The adjusted value for σ_{pure} is within its reported range (Table 2.1) and is the smallest adjustment relative to the original value, whereas the adjusted values for all other dielectric properties are outside of their respective reported ranges and are large adjustments relative to their original values. We therefore prefer to only adjust σ_{pure} to calibrate the conductivity model using the radar-derived attenuation rate at Siple Dome and conclude that uncertainty in σ_{pure} is the most problematic component of our modeling. More precise measurements of the σ_{pure} over a wide temperature range, including the temperatures close to the melting

point, are crucial.

Alternatively, we can adjust values of the dielectric properties to those from preferred sources. Using only the values of σ_{pure} and E_{pure} derived from *Johari and Charette* (1975) (Table 2.1) and keeping the other dielectric properties at their original values yields a depth-averaged modeled attenuation rate of 24.0 ± 2.2 dB km^{-1} at Siple Dome, which is in good agreement with the radar-derived attenuation rate. Their experiments included a relatively large number of measurements of the conductivity of pure ice that also covered the range of temperatures present at Siple Dome, including temperatures near the melting point.

2.7.2 Unmodeled Physics

Melting-point depression

Most of the conductivity experiments referenced in Table 2.1 were performed at atmospheric pressure. However, the melting point of ice is depressed by pressure and soluble impurities (*Paterson* (1994)). This temperature depression is expected to increase the mobility of impurities in the ice, effectively increasing the ice conductivity (*Wolff and Paren* (1984)). Ignoring the firn, the melting point depression for ice overburden is -8.7×10^{-4} K m^{-1}. However, *Johari and Charette* (1975) measured conductivity at a range of hydrostatic pressures (10^5–10^7 Pa) and did not observe any change in conductivity. The adjustment for sea-ice salinity is -2.03 K M^{-1} and this adjustment is also inversely proportional to the fractional water content in the ice (*Paterson* (1994)). The salinities present in meteoric polar ice are generally less than 15 μM (e.g., Figure 2.2b), so the correction for salinity is less than -0.001 K and is ignored in this study. Assuming that the melting-point depression due to acids is similar to that of salinity, we also do not correct for acids. To examine the possible importance of the pressure-melting effect, we adjust the measured temperature profile by adding the pressure-melting correction due to the ice overburden and calculate an adjusted attenuation rate that is 0.9 dB km^{-1} larger than our original modeled value. This value is closer to the radar-derived value.

Eutectic point of NaCl

Matsuoka et al. (1997a) found that the molar conductivity of NaCl–doped ice at 5 GHz decreased by more than 50% across the eutectic point of NaCl ($-21°$C) and that NaCl existed primarily in the liquid phase in their samples. However, the Cl^- ions that contribute to the conductivity of meteoric ice are believed to form defects in the lattice (section 2.3.1) rather than exist in the liquid phase. Furthermore, *Moore et al.* (1992a) did not observe this phenomenon while using DEP (300 kHz) on ice core samples with large values of $[\mathrm{ss}\,Cl^-]$ across a range of temperatures that crossed the eutectic point of NaCl (their Figure 4). Conductivity due to $[\mathrm{ss}\,Cl^-]$ is probably dispersive (*Moore and Fujita* (1993)), so a change in conductivity across the eutectic point of NaCl may not be apparent at or below 300 kHz. The eutectic temperature of NaCl occurs at a depth of $\sim$ 310 m at Siple Dome, so it is possible that the $\mathrm{ss}\,Cl^-$ component of conductivity changes abruptly there if NaCl is present in the liquid phase. To examine the possible importance of this effect, we simply assume that $[\mathrm{ss}\,Cl^-]$ does not contribute to conductivity at temperatures below its eutectic point. This yields an attenuation rate that is 0.6 $\mathrm{dB\,km^{-1}}$ smaller than our original modeled value and differs further from the radar-derived value.

Matsuoka et al. (1997a) also found that the molar conductivity of acid-doped ice decreased significantly below the eutectic point of two acid species, HNO_3 ($-43°$C) and H_2SO_4 ($-73°$C), which are believed to be in the liquid phase in meteoric ice. *Fujita et al.* (2002b) observed a decrease in the apparent activation energy of the AC-ECM conductivity of several Antarctic ice-core samples below $\sim -81°$C. They interpreted this change as due to a large decrease in liquid-phase conduction across the eutectic point of the samples, which had $[SO_4^{2-}] > 8$ μM and other impurities. However, the eutectic points of HNO_3 and H_2SO_4 are outside the range of temperatures measured at Siple Dome (Figure 2.2c) so we do not consider an adjustment to the conductivity model below these temperatures.

Premelting ice

There is some evidence that the dielectric properties of acid-doped ice change when the temperature exceeds about $-10°$C (Figure 2 of *Matsuoka et al.* (1997a)), although this phe-

nomenon is not always observed (e.g., Figure 4 of *Moore et al.* (1992a)). This phenomenon is likely related to melting-point depression (section 2.7.2) and possible explanations include: the surface conductance at grain boundaries may increase as the thickness of the liquid-like layer increases in premelting ice (*Petrenko and Whitworth* (1999)); the presence of impurities can also increase the rate of premelting (*Wettlaufer* (1999)); HSO_4^- at grain boundaries dissociates into H^+ and SO_4^{2-} as the liquid-like layer grows at high temperatures, thus increasing $[H^+]$. Analogously, the temperature dependence of the mechanical properties of ice change as grain-boundary sliding increases above $-10°C$ (*Paterson* (1994)). At Siple Dome, temperatures above $-10°C$ occur at depths below ~ 750 m, which is about a quarter of the ice thickness, so this phenomenon may be important and present there.

We examine the possible importance of the increased conductivity of premelting ice by arbitrarily doubling the mean value of E_{H^+} to 0.40 ± 0.08 eV at temperatures above $-10°C$ (Figure 2 of *Matsuoka et al.* (1997a)). In this temperature range, there are few experimental data to constrain dielectric properties and the pure ice contribution dominates conductivity (Figure 2.1), but H^+ is the dominant impurity in terms of its contribution to attenuation at Siple Dome (Figure 2.3). To avoid an unrealistic and unobserved discontinuity in μ_{H^+} at $-10°C$, μ_{H^+} above $-10°C$ is adjusted so that μ_{H^+} using the original E_{H^+} value is equal to μ_{H^+} using the doubled E_{H^+} value at $-10°C$. This adjustment yields an attenuation rate that is just 0.2 $dB\,km^{-1}$ larger than our original modeled value.

2.7.3 Influence of Spatial Variability on Radar-derived Attenuation

Spatial variations in impurity and temperature profiles complicate interpretation of the radar-derived attenuation from traverse data. The traverse data used in section 2.6.3 sampled ice from points up to 54 km away from the ice core. However, cold ice is advected downwards from the ice divide towards the flanks, so the flanks are presumably colder than the ice divide. Also, the rheology of ice at low deviatoric stresses causes higher temperatures that are localized underneath the ice divide (e.g., *Nereson and Waddington* (2002)). Ice thickness and accumulation rate gradients (*Nereson et al.* (2000)) will also produce asymmetry in the englacial temperatures across Siple Dome. The attenuation rate at the Siple

Dome ice divide therefore may be larger than the value derived from traverse data, which also sampled ice at lower temperatures on the flanks.

Restricting the traverse data to within 5 km of the ice divide and recalculating the attenuation rate, this gives an unreasonably high attenuation rate (66 $\mathrm{dB\,km^{-1}}$) with a large uncertainty (> 30 $\mathrm{dB\,km^{-1}}$), which is not supported by direct observations of the BRPs over this portion of the traverse. This result also implies that caution is needed when estimating attenuation from such restricted traverse data. To calculate the attenuation rate using traverse data requires BRPs from a range of ice thicknesses comparable to or greater than the attenuation length. This condition is satisfied for the traverse data at Siple Dome used to calculate the radar-derived attenuation rate (section 2.6.3), where the range of ice thicknesses ($\sim$ 350 m) is approximately double the radar-derived attenuation length (172 m).

2.7.4 Comparison to Attenuation at Other Sites

The modeled and radar-derived estimates of the depth-averaged attenuation rate at Siple Dome are not directly applicable to other sites. Different locations and glaciological settings have different impurity and temperature profiles, which control the attenuation rate profile. However, it is helpful to compare the modeled and radar-derived attenuation at Siple Dome to other sites and place it in the context of previous estimates of attenuation in ice sheets.

Bentley et al. (1998) calculated an attenuation rate of 17.3 $\mathrm{dB\,km^{-1}}$ for the Ross Ice Shelf at the outlet of Kamb Ice Stream, which is $\sim$ 100 km from Siple Dome, by assuming that the reflections underneath their survey region were from seawater. Using the same method, *Peters et al.* (2005) calculated an attenuation rate of 18 $\mathrm{dB\,km^{-1}}$ for Kamb Ice Stream. Both *Bentley et al.* (1998) and *Peters et al.* (2005) derived basal reflectivity maps of their study regions that are consistent with glaciological expectations. Their attenuation rates on or near Kamb Ice Stream are lower than the modeled and radar-derived values at Siple Dome. This difference in attenuation rates may be consistent with differences in observed temperature profiles: measured profiles from further upstream on Kamb Ice Stream all show higher basal temperature gradients and lower temperatures at intermediate depths

than those at Siple Dome (*Engelhardt* (2004)). Temperature is the dominant control on ice-sheet attenuation (Figure 2.3), so regions that have generally higher englacial temperatures will have higher attenuation rates, assuming their mean impurity concentrations are the same.

Separately, *Peters et al.* (2005) calculated an attenuation rate of 21 dB km^{-1} at Whillans Ice Stream using the temperature–attenuation relationship of *Gudmandsen* (1971) and a measured borehole temperature profile. Combining the temperature–attenuation relationship of *Gudmandsen* (1971) and the measured temperature profile at Siple Dome (Figure 2.2c) yields an attenuation rate of 21.5 dB km^{-1}. This value is near the modeled and radar-derived values for Siple Dome, but the agreement is coincidental. Impurity concentrations were implicitly included in the temperature–attenuation relationship of *Gudmandsen* (1971) (section 2.3.2), but that relationship does not allow for varying impurity concentrations, which can significantly alter attenuation rates (Figure 2.3). As temperature increases, increases in [H^+] or [ss Cl^-] produce larger attenuation rate increases compared to equivalent [H^+] or [ss Cl^-] increases at lower temperatures (Figures 2.2 and 2.3).

Corr et al. (1993) estimated attenuation from radar measurements on the Ronne and George VI ice shelves in West Antarctica. We convert their reported attenuation values to attenuation rates: 9 ± 1 dB km^{-1} at their Ronne Ice Shelf site and 27 ± 3 dB km^{-1} at their George VI Ice Shelf site. They attributed the difference in attenuation at the two sites to differing mean impurity concentrations. Their ice-shelf sites are more dynamic and proximal to the sea than Siple Dome, especially the George VI site; these sites illustrate the potentially large variability of attenuation rates over spatial scales of $\sim$ 500 km and their dependence on relative coastal proximity.

2.8 Conclusions

We have presented a framework for modeling englacial radar attenuation using impurity concentration and temperature profiles from ice cores and boreholes, respectively. The conductivity model used in this study is based on a synthesis of available experimental data. However, the value of σ_{pure} is not well constrained and its uncertainty contributes more than 50% of the uncertainty in the depth-averaged modeled attenuation rate at Siple

Dome. More measurements are needed to reduce the uncertainty in the value of σ_{pure}. More measurements are also needed to further quantify the effects of (1) varying firn densities, (2) high pressures to simulate the effect of the pressure overburden in ice sheets and (3) temperatures near the eutectic point of NaCl and near the melting point.

The depth-averaged modeled attenuation rate at Siple Dome (20.0 ± 5.7 dB km^{-1}) is somewhat lower than the radar-derived value (25.3 ± 1.1 dB km^{-1}). However, an adjustment to σ_{pure} that is within its range of reported values is sufficient to match the modeled and radar-derived attenuation rates. Using the values of σ_{pure} and E_{pure} derived from *Johari and Charette* (1975), the modeled attenuation rate is 24.0 ± 2.2 dB km^{-1}, which also matches the radar-derived attenuation rate within the uncertainties of these two values. When integrated over a two-way raypath through an ice sheet, the modeled one-way attenuation rate uncertainty (5.7 dB km^{-1}) is potentially large compared to the reflectivity difference between wet and dry grounded ice-sheet beds ($\sim$ 4–26 dB; *Peters et al.* (2005)), which depends on the dielectric properties of the subglacial interface. This comparison emphasizes the importance of constraining attenuation rate uncertainties for the accurate interpretation of basal echo intensities.

This work shows that impurity concentrations and temperature profiles are needed to model englacial radar attenuation; neglecting the H^+ and ss Cl^- contributions to attenuation decreases the modeled attenuation rate at Siple Dome by more than 30%. Also, variations in impurity concentration profiles, particularly $[H^+]$, can produce large changes in the attenuation rate profile.

The depth-averaged attenuation rate increases with depth and is primarily controlled by the temperature profile. Radar-derived depth-averaged attenuation rates to internal reflections could thus provide further constraints on the temperature profile. The conductivity model presented here could also be used to study spatial variations in attenuation. Ice-flow models can be used to track englacial temperatures and the vertical strain history along a flowline that passes through an ice-core site (e.g., *Nereson and Waddington* (2002); *Clarke et al.* (2005)). Those model outputs could be used to extrapolate impurity concentration profiles from an ice core based on the vertical strain history and then calculate the spatial variation of attenuation along the flowline.

Chapter 3

RADAR DETECTION OF ACCRETED ICE OVER LAKE VOSTOK, ANTARCTICA

This chapter was submitted to Earth and Planetary Science Letters in February 2008 and revised and resubmitted in July 2008. My co-authors are Kenichi Matsuoka and Michael Studinger. I wrote most of the text and conducted most of the work described in this chapter, including the development of the attenuation model for Vostok and the calculation of the reflectivity values for different possible reflection mechanisms. Kenichi Matsuoka guided my work, wrote the paragraph concerning birefringence and extensively edited the paper. Michael Studinger provided several datasets, assisted with the radar-data analysis, guided the work in the context of previous studies of Lake Vostok and edited the paper. Peter deMonecal (the scientific editor), Olaf Eisen and two anonymous referees reviewed this paper. Ed Waddington provided many helpful comments on the resubmitted draft.

3.1 Summary

Airborne radar data collected over Lake Vostok, East Antarctica, show a reflection close to the Vostok ice core below the depth of the meteoric–accreted ice boundary (MAIB) and near the boundary between impurity-rich (1) and impurity-poor (2) accreted ice (A12B). The spatial pattern of detection of the reflection is aligned with ice flow over the southern half of the lake. Ice-core data from the accreted ice show large variations in the number density of inclusions, soluble chloride-ion concentration ($[Cl^-]$), charge-balance-derived acidity ($[H^+]_{cb}$) and crystal-orientation fabric. Here we investigate the existing hypothesis that this reflection is due to the MAIB and seek possible reflection causes that explain the radar-derived reflectivity (-49 ± 8 dB). The maximum reflectivity due to an insoluble mineral-inclusions contrast is -125 dB, based on a likely range of inclusion permittivities and diameters. If none of the Cl^- or H^+ ions are trapped within inclusions, then ice-conductivity models predict a reflectivity of -59 dB near the MAIB and -58 dB near the

A12B, primarily due to a large $[H^+]_{cb}$ increase and decrease, respectively. If some of those ions are trapped within inclusions, then those values are smaller. Fabric contrasts at either boundary can produce significant reflectivities (-62 dB). These results indicate that the mineral-inclusion contrast near the MAIB does not cause the observed reflection. Because of uncertainty in the *in situ* location of the soluble impurities, and because impurity-rich accreted ice 1 is believed to only originate in the small bay in the southwestern corner of the lake yet the reflection is observed over a much wider area, we argue that a fabric contrast at the A12B is the probable reflection cause. Both predicted spatial variations in accretion rates near the upstream shoreline, or lower ice temperatures along flowbands that originate at bedrock ridges near the upstream shoreline, may explain why the reflection is not detected everywhere that accretion is predicted.

3.2 Introduction

Lake Vostok, East Antarctica, is the world's largest known subglacial lake (*Kapitsa et al.* (1996); Figure 3.1) and has been the subject of intense study, including the drilling of a 3623-m-long ice core to within $\sim$ 120 m of the ice–lake interface at the southern end of the lake (*Petit et al.* (1999)). Radar surveys (e.g., *Bell et al.* (2002); *Tikku et al.* (2004)) and modeling (e.g., *Wüest and Carmack* (2000); *Thoma et al.* (2008)) suggest that the lake is in a dynamic balance with the overlying ice sheet, with basal melting occurring in the northern half of the lake and basal freeze-on of lake water (hereafter accretion) occurring in the southern half of the lake (Figure 3.1b).

Bell et al. (2002) examined the radar transect that crossed over the lake closest to the ice-core site and found a weak, isolated and intermittent reflection somewhat below the depth of the meteoric–accreted ice boundary (MAIB) observed in the ice core (Figures 3.1–3.3). This reflection's height above the ice–lake interface increases along-flow (Figure 3.2), as expected if this reflection is related to the MAIB and more ice is accreted as the ice sheet flows over the lake. The MAIB has also been observed in radar data collected at several Antarctic ice shelves (e.g., *Shabtaie and Bentley* (1982), *Blindow* (1994)).

Here we investigate the nature of the radar reflection observed by *Bell et al.* (2002) and their hypothesis that this reflection represents the MAIB. *Jouzel et al.* (1999) and

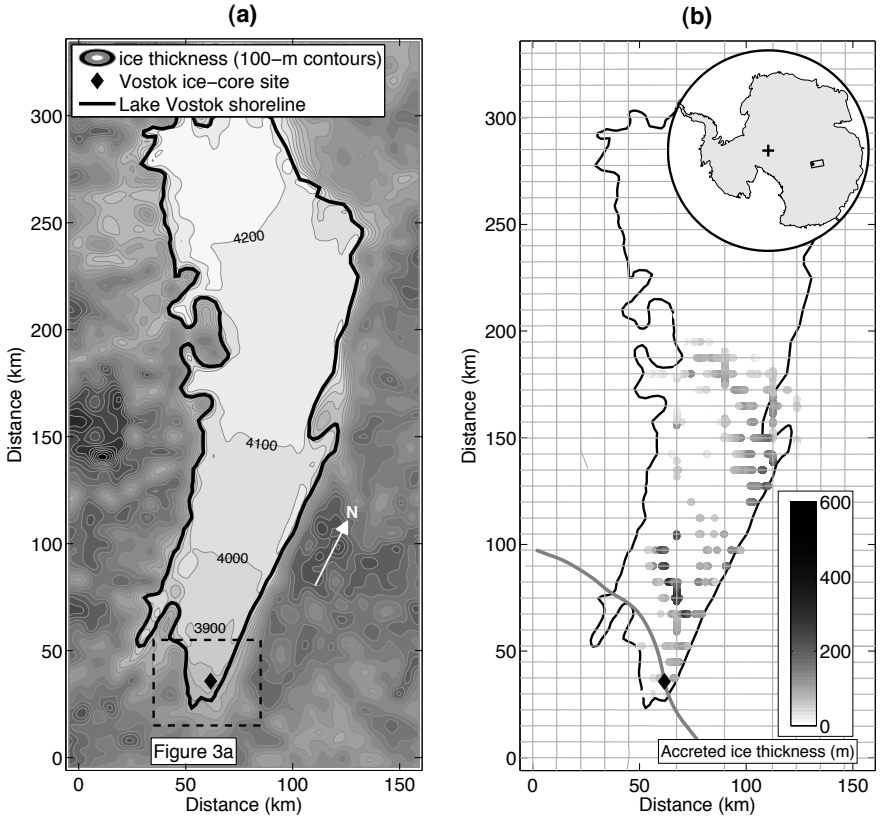

Figure 3.1: (a) Contour map of ice thickness in the Lake Vostok region (*Studinger et al.* (2003)). Also shown are the Vostok ice-core site, the area of Figure 3.3a, and the lake shoreline. (b) Map of accreted-ice thickness using picks made by *Tikku et al.* (2004). Also shown is the ice flowline passing through the Vostok ice-core site (thick gray line) inferred from the structure tracking by *Tikku et al.* (2004) and the airborne-radar flight lines (thin light gray lines). The inset map shows the location of the main panel in Antarctica.

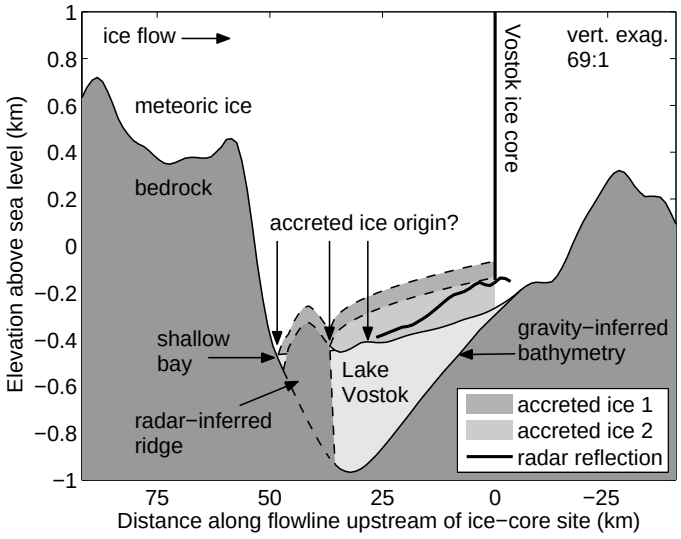

Figure 3.2: Cross-section of deep ice along Vostok flowline. Bedrock, ice–lake-interface (*Studinger et al.* (2003)), lake-bottom (*Studinger et al.* (2004)) and accreted-ice reflection elevations (*Tikku et al.* (2004)) are interpolated along the flowline shown in Figures 3.1b and 3.3a. The accreted ice elevations (dashed lines) are constrained only by their depths in the Vostok ice core. The lake-bathymetry profile was inferred from gravity data and does not resolve the radar-observed bedrock ridge that separates the main lake from the shallow bay where accreted ice 1 is believed to form.

de Angelis et al. (2004) studied the chemistry of the Lake Vostok accreted ice and identified two distinct types: an impurity- and inclusion-rich layer just below the MAIB (accreted ice 1) and an impurity- and inclusion-poor layer (accreted ice 2) below that first layer (Figure 3.4). Contrasts in both the chemical and physical properties of the accreted ice were observed, the depth of the radar layer in question is closer to the ice-core-identified depth of boundary between these two types of accreted ice (A12B) than to the depth of the MAIB. We use Vostok ice-core data to model the radar reflectivity below the MAIB and then compare our modeled values to the value derived from radar data. Identification of the cause of this reflection is important for the interpretation of its spatial pattern of detection. We aim to decipher which properties of the MAIB or within the accreted ice could explain the observed reflection, what conditions at the ice–lake interface are necessary to produce the reflection, and what these conditions imply about accretion mechanisms underneath ice sheets and ice shelves.

3.3 Data and Methods

3.3.1 Radar Data and Analysis

We use the 60-MHz airborne ice-penetrating radar data collected in a $\sim$ 350- by 150-km grid over Lake Vostok by the U.S. Support Office for Aerogeophysical Research (SOAR) at the University of Texas Institute for Geophysics (*Studinger et al.* (2003)); the system characteristics were described by *Blankenship et al.* (2001). *Tikku et al.* (2004) mapped the depth of the reflection that *Bell et al.* (2002) first suggested represents the MAIB and we use their depth picks to guide our investigation of that reflection. Its detection is generally restricted to the southern half of the lake and is concentrated along flowbands that are correlated with the presence of bedrock ridges on the upstream shoreline (Figure 3.1; *Tikku et al.* (2004)). Figure 3.3a shows a map of the southern end of Lake Vostok and the SOAR radar data collected in that region. This figure also shows a circle centered along CCx-X06a with a radius equal to the ice thickness there; this circle shows that most of the echoes investigated in this study cannot be off-nadir bedrock reflections and thus must be caused by an englacial reflector.

We use the radar equation to calculate the reflectivity R of the accreted-ice echoes (e.g., *Matsuoka et al.* (2003)):

$$P_r = \frac{RP_tT^2G^2q\lambda^2LB}{\left(h + \frac{z}{\sqrt{\varepsilon'_{ice}}}\right)^2 (4\pi)^3}, \tag{3.1}$$

where P_r is the received power, or echo intensity (Figure 3.3d), P_t is the transmitted power, T is the transmission loss at the air–ice interface, G is the system gain, q characterizes the antenna beam width, λ is the wavelength in the vacuum, L is the total dielectric attenuation loss along the two-way raypath, h is the aircraft height above the ice surface, z is the depth to the reflection, ε'_{ice} is the real part of the complex relative permittivity (hereafter permittivity) of ice near the ice-core site (*Popov et al.* (2003)) and B is the degree of echo extinction due to birefringence. Excepting L and B, all of these quantities are either known instrumental parameters or their values that can be estimated from the radar data. These values are summarized in Table 3.1. Among these parameters, uncertainty in L is the most significant (section 3.4.1). L is proportional to the conductivity σ integrated over the ice column through which the radio waves travel and can therefore be estimated using an ice-conductivity model (section 3.3.2). The one-way attenuation rate N_a in $\mathrm{dB\,km^{-1}}$ is linearly proportional to ice conductivity σ in $\mu\mathrm{S\ m^{-1}}$ (Chapter 2):

$$N_a = 0.919\sigma. \tag{3.2}$$

Figure 3.3b shows a portion of the radargram from the transect (CCx-X06a) that crosses Lake Vostok closest to the ice-core site. Depths were calculated using a radio-wave speed of 168.4 $\mathrm{m\,\mu s^{-1}}$ averaged over the ice column to the ice–lake interface (*Popov et al.* (2003); equivalent to $\varepsilon'_{ice} = 3.169$). Using the uncertainty in the mean radio-wave speed (0.5 $\mathrm{m\,\mu s^{-1}}$), the time-sampling interval of the radar data (16 ns) and uncertainty in our layer picking, we estimate that the physical uncertainty in our depth estimates for any individual pick is about 10 m. CCx-X06a does not cross directly over the ice-core site, instead crossing the lake 1.3 km northwest of the ice-core site. The depth of the accreted-ice reflection (3603 ± 88 m) is calculated as the best-fit depth at the trace closest to the ice-core site (Figure 3.3c), assuming that the reflection depth decreases linearly along this transect that is not parallel to flow. This reflection is -23 m to 153 m deeper than the depth of the MAIB

Figure 3.3: (a) Map of the southern end of Lake Vostok that shows the SOAR radar transects (CCx-X06a labeled), the lake shoreline (*Studinger et al.* (2004)), the Vostok ice-core site, the location of accreted-ice echoes (*Tikku et al.* (2004)), contour lines of the bed topography (*Studinger et al.* (2003)) and a circle centered along CCx-X06a whose radius is equal to the ice thickness at its center (section 3.3). (b) CCx-X06a radargram showing the MAIB and ice–lake reflection. The black vertical line near the center of the lake represents the trace closest to the Vostok ice core. The black box shows the area of echoes shown in (c) and (d). To better visualize the reflection each trace in the radargram shown here has been differentiated in time and then laterally smoothed using a 3-trace mean consisting of each trace and the one adjacent to it on both sides (equivalent to a running-mean filter $\sim$ 45-m long). We note that the received power P_r was calculated using the undifferentiated and unsmoothed radar data. The two near-vertical scars that cross the lake edges are hyperbolic reflections due to surface structures at the Vostok station. (c) Echo picks shown at the same vertical scale as (b) and the best-fit depth at the Vostok ice-core site. The error bar is calculated using the standard error of the best-fit line parameters. (d) Reflection echo intensity (P_r) at detected locations on this transect and the mean and standard deviation of those intensities shown at the trace that is closest to the ice-core site. The noise floor is calculated as the mean received power within the time range 60–61.5 μs, which is $\sim$ 10 μs later than the bed reflection. The two gaps in the noise-floor series are due to the hyperbolic reflections visible in (b), which prevent an accurate calculation of the noise floor.

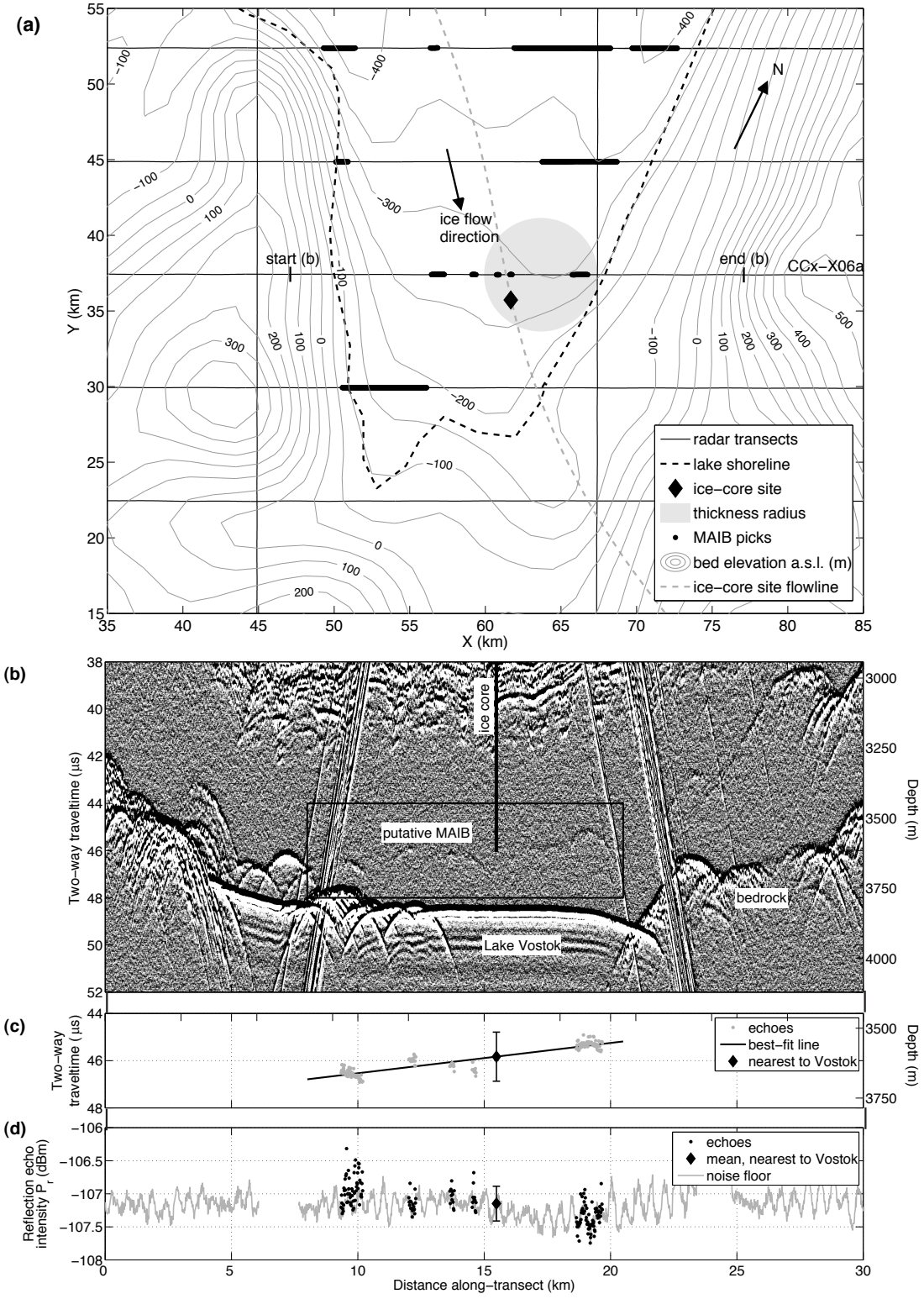
(a)
Y (km)
X (km)
N
ice flow direction
start (b)
end (b)
CCx–X06a
radar transects
lake shoreline
ice–core site
thickness radius
MAIB picks
bed elevation a.s.l. (m)
ice–core site flowline
(b)
Two–way traveltime (μs)
Depth (m)
ice core
putative MAIB
bedrock
Lake Vostok
(c)
Two–way traveltime (μs)
Depth (m)
echoes
best–fit line
nearest to Vostok
(d)
Reflection echo intensity P_r (dBm)
Distance along–transect (km)
echoes
mean, nearest to Vostok
noise floor

Table 3.1: Radar-system parameters and values estimated from transect CCx-X06a at the traces where the accreted-ice echoes were detected (Figure 3.3).

Symbol	Description	Value
P_r	Received power	-107.1 ± 0.3 dBm
P_t	Transmitted power	68.5 ± 0.5 dBm
T	Transmission loss at ice–air interface	-1 dB
G	Antenna gain	9.7 ± 1 dB [a]
q	Related to antenna beam width	0 dB (assumed)
λ	Wavelength in the vacuum	5 m
L	Dielectric attenuation loss	-57 ± 8 dB [b]
B	Echo extinction due to birefringence	0 dB [c]
z	Depth to reflection below surface	3603 ± 88 m
h	Aircraft height above surface [d]	459 ± 1 m

[a] Values provided by M.E. Peters, pers. comm. 2005. [b] Calculation of L explained in section 3.4.1. [c] See discussion in section 3.5.1. [d] Measured by differential GPS antenna mounted on top of aircraft fuselage.

(3538 m) identified in the ice core by large changes in δD and δ^{18}O of the ice (*Jouzel et al.* (1999)). Ice thickness decreases regionally towards the southern end of the lake (Figure 3.1a), but even if the MAIB shallows proportionally with the ice-thickness gradient, this gradient can only explain a few meters of the depth difference. However, there are large contrasts in several chemical and physical properties of the ice core beginning about 10 m below the depth of the isotope-identified MAIB (*de Angelis et al.* (2004); *Jouzel et al.* (1999)). The depth of the reflection is within 5 m of the A12B (3608 m), so we must also consider whether changes in the dielectric properties of ice at that boundary can explain the observed reflection.

3.3.2 Ice-Conductivity Model

We use an ice-conductivity model to calculate both the value of L (section 3.4.1) and the magnitude of the conductivity contrasts in the accreted ice (section 3.4.2). Here we describe its main features and refer the reader to Chapter 2 for further details. The high-

frequency (0.1–300 MHz) conductivity of meteoric polar ice is linearly dependent on the *in situ* molar concentrations of acid ($[H^+]$; square brackets represent molar concentration), sea-salt chloride ($[ss\,Cl^-]$) and ammonium ($[NH_4^+]$) (e.g., *Wolff et al.* (1997)). We ignore the conductivity contribution from NH_4^+ because this contribution is small at Vostok (discussed below). These linear dependencies are represented using molar conductivities (μ). The conductivity of pure ice $\sigma_{\rm pure}$ and each of the components of the conductivity due to soluble impurities have an Arrhenius-type temperature dependence, each represented by a different activation energy E. The total conductivity σ is:

$$\begin{aligned}\sigma &= \sigma_{\rm pure}\exp\left[\frac{E_{\rm pure}}{k}\left(\frac{1}{T_r}-\frac{1}{T}\right)\right] \\ &\quad +\mu_{\rm H^+}[H^+]\exp\left[\frac{E_{\rm H^+}}{k}\left(\frac{1}{T_r}-\frac{1}{T}\right)\right] \\ &\quad +\mu_{\rm ss\,Cl^-}[ss\,Cl^-]\exp\left[\frac{E_{\rm ss\,Cl^-}}{k}\left(\frac{1}{T_r}-\frac{1}{T}\right)\right], \end{aligned} \tag{3.3}$$

where k is Boltzmann's constant, T is temperature and T_r is a reference temperature. $\sigma_{\rm pure}$, $\mu_{\rm H^+}$ and $\mu_{\rm ss\,Cl^-}$ depend on density (*Barnes et al.* (2002)), but their density dependencies are not shown here for simplicity.

NH_4^+ may also enter the ice lattice (*Moore et al.* (1994b)), but its mean concentration is less than 0.1 μM (M = mol L^{-1}) in the accreted ice. Its potential contribution to the conductivity is small (< 0.5 μS m^{-1}) compared to the conductivity contrasts modeled in Figure 3.4b (> 40 μS m^{-1}) and is therefore neglected. Doping lab-grown ice with HF also increases its conductivity (e.g., *Camplin and Glen* (1973)) and F^- was detected in the accreted ice. The possible conductivity contribution of F^- ions is also neglected because the mean value of $[F^-]$ is less than 0.2 μM in the accreted ice and its conductivity contribution is expected to be less than 1 μS m^{-1}. *de Angelis et al.* (2004) suggested that Na^+ and NO_3^- ions may also enter the ice lattice, where they would presumably also create defects. However, the effect of those ions on ac conductivity has not been sufficiently quantified and they may instead be trapped in microdroplets (*de Angelis et al.* (2005)), so their possible effect is neglected here.

The pure-ice conductivity, molar conductivities of each impurity, and the activation energies of all of these components constitute the dielectric properties used in the conductivity

Table 3.2: Values and uncertainties of the dielectric properties used in the ice-conductivity model described in section 3.3.2 and (3.3).

Symbol	Description	Value
σ_{pure}	Conductivity of pure ice	9.2 ± 0.2 S m^{-1} [a]
$\mu_{\text{H+}}$	Molar conductivity of [H$^+$]	3.2 ± 0.5 S m^{-1} M^{-1}
$\mu_{\text{ss Cl}-}$	Molar conductivity of [ss Cl$^-$]	0.43 ± 0.07 S m^{-1} M^{-1}
E_{pure}	Activation energy of pure ice	0.51 ± 0.05 eV [a]
$E_{\text{H+}}$	Activation energy of [H$^+$]	0.20 ± 0.04
$E_{\text{ss Cl}-}$	Activation energy of [ss Cl$^-$]	0.19 ± 0.02
T_r	Reference temperature	251 K

[a] Values derived from conductivity data collected by *Johari and Charette* (1975), not the mean values from the synthesis of published dielectric-property values (Chapter 2).

model (3.3). Their values were determined using a synthesis of published dielectric-property measurements (Chapter 2); Table 3.2 summarizes the values used here. There are several measurements of σ_{pure} and E_{pure}, but here we only use the values inferred from *Johari and Charette* (1975). Those values produced a better match between the radar-derived (25.3 ± 1.1 dB km^{-1}) and modeled attenuation rates (24.0 ± 2.2 dB km^{-1}) at Siple Dome, West Antarctica, as compared to using the mean values of the pure-ice dielectric properties (20.0 ± 5.7 dB km^{-1}) (Chapter 2.6). Only the attenuation rates modeled below, and not the modeled conductivity contrasts (section 3.4.2), are affected by the choice of the values of the pure-ice dielectric properties.

3.3.3 Ice-Core Data

For ice chemistry, we use ion-chromatography data from the most recent Vostok ice core between the depth range 150–3623 m (*Petit et al.* (1999); *de Angelis et al.* (2004)), which includes nearly all of the meteoric ice and the top 85 m of the $\sim$ 220-m-thick accreted ice at the ice-core site (*Jouzel et al.* (1999)). The ice core was sampled using $\sim$ 10-cm long columns that were irregularly separated, especially in the meteoric ice, where the mean interval between measurements down to 3348 m was 8.8 ± 8.7 m. *Jouzel et al.* (1999) described the

grain sizes of the accreted ice, the electrical conductivity measurement (ECM) profile and along-core number density of visible inclusions. For ice temperatures, we use a composite borehole-temperature profile that is based on profiles measured separately (*Tsyganova and Salamatin* (2004); *Lipenkov et al.* (2004)) and a linear extrapolation from the temperature near the bottom of the borehole (−5.49°C at 3620 m) to the pressure-melting point at the ice–lake interface (−2.83°C at 3755 m) (V.Y. Lipenkov, pers. comm., 2006). We also use the density profile measured from the ice core by hydrostatic weighing (*Lipenkov et al.* (1997)); density data were collected at irregular intervals down to a depth of 2540 m. Finally, to determine the fabric contrast below the MAIB, we also use *c*-axis orientation data (*Souchez et al.* (2000)).

3.3.4 Impurity Concentrations

[H^+]

Impurity concentrations are calculated using ion-chromatography data, which determine the concentrations of major soluble ions present in melted ice-core samples. In the meteoric ice, [ss Cl^-] is calculated by separating [Cl^-] into its sea-salt and excess components using the conservative ion method (*Dixon et al.* (2004)). [H^+] cannot be directly measured by ion chromatography but it can be inferred using a charge balance of the measured ions ([H^+]$_{cb}$). However, this charge balance does not necessarily represent the *in situ* [H^+] that contributes to the ice conductivity because bivalent ions (e.g., H_2SO_4) that are fully dissociated in meltwater are presumably singly dissociated at grain boundaries (e.g., *Mulvaney et al.* (1988)). We therefore correct [H^+]$_{cb}$ in the meteoric ice for the single dissociation of H_2SO_4 at liquid-filled grain boundaries by not doubling the contribution of [SO_4^{2-}] from H_2SO_4 ([xs SO_4^{2-}]), which decreases the mean acidity in the meteoric ice from 1.8 μM to 0.5 μM. The charge- balance-derived acidity ([H^+]$_{cb}$) is therefore:

$$\begin{aligned}[H^+] &= [Cl^-] + [NO_3^-] + 2\,[\text{ss}\,SO_4^{2-}] + [\text{xs}\,SO_4^{2-}] \\ &\quad + [CH_3SO_3^-] - 2\,[Ca^{2+}] - [K^+] \\ &\quad - 2\,[Mg^{2+}] - [Na^+] - [NH_4^+]. \end{aligned} \tag{3.4}$$

The conductivity contribution from acids is significantly reduced below the eutectic point of each acid (*Matsuoka et al.* (1997a)) because the acids are at liquid-filled grain boundaries. In the Vostok ice core, ice temperatures lower than the eutectic point of HNO3 ($-43°$C) occur at depths shallower than 1515 m. We therefore zero the contribution to $[H^+]_{cb}$ from HNO3 in the depth range 0–1515 m and do not correct for the eutectic points of H_2SO_4 ($-73°$C) and HCl ($-85°$C) because those temperatures are below the lowest ice temperatures observed at Vostok ($-55°$C).

We do not use the values of $[H^+]$ from acid titration of samples of an earlier Vostok ice core (*Legrand et al.* (1988)) because these values do not necessarily represent the *in situ* $[H^+]$ that contributes to the electrical conductivity of ice, and because we are using data from the newest available ice core (section 3.3.3). ECM is non-linearly dependent on *in situ* $[H^+]$ and is often used to infer the *in situ* $[H^+]$ in ice cores (e.g., *Wolff* (2000)). At Siple Dome, we found a satisfactory agreement between the ECM values and $[H^+]_{cb}$ (Chapter 2). However, at Vostok, we are unable to compare the $[H^+]_{cb}$ profile to the available non-continuous ECM profile because of the different sampling intervals of those data.

The meteoric ice sampled just above the MAIB shows little variation in its ion concentrations, whereas ion concentrations within the accreted ice show large variations (*de Angelis et al.* (2004)) that could produce a significant conductivity contrast and a detectable reflection. Meteoric ice is formed by the densification of snow, whereas the accreted ice over Lake Vostok is probably formed by the consolidation of frazil ice crystals formed in supercooled water (e.g, *Souchez et al.* (2000); *Souchez et al.* (2003)). A similar process is believed to occur underneath portions of some ice shelves. This fundamentally different formation mechanism from that of meteoric ice means that the incorporation of soluble impurities into the ice is also different, which in turn affects the calculation of the *in situ* ice conductivity using meltwater-ion concentrations.

In the meteoric ice just above the MAIB, $[H^+]_{cb}$ is about 1.5 μM; in the 70 m of measured accreted ice, its mean and standard deviation are 3.0 ± 4.4 μM, and its maximum value exceeds 20 μM 10 m below the MAIB (Figure 4a). Ion concentrations decrease sharply in the first 5 m below the MAIB, but 10 m below the MAIB they increase even more sharply. It is unclear why this increase does not occur closer to the MAIB. The charge balance of major

ions in melted ice-core samples does not inform us about the location of the ions within the accreted ice, such as within the ice lattice, at grain boundaries or within isolated inclusions. We must therefore infer their location from other data and correct $[H^+]_{cb}$ as necessary. For the accreted ice, we do not correct for the dissociation of H_2SO_4 as was done for the meteoric ice (3.4), because the SO_4^{2-} ions are likely in isolated inclusions (*de Angelis et al.* (2004)) and thus not associated with the H^+ ions that are likely in the lattice (discussed below). We also include $[F^-]$, which was detected in the accreted ice, in (3.4). Although the inclusions themselves must be in charge balance and therefore cations must be present, there is no a priori expectation that the H^+ ions in the accreted ice are also concentrated in inclusions with the SO_4^{2-} ions. Also, the relative uncertainty of the charge-balance-derived $[H^+]$ is potentially large because it is a sum of ion-concentration measurements with large analytic uncertainties (*de Angelis et al.* (2004)), although we cannot quantify these uncertainties here.

The ECM data show near-zero values at its detection limit in the accreted ice (*Jouzel et al.* (1999)), which implies that $[H^+] \approx 0$ μM and also conflicts with the large values of the $[H^+]_{cb}$ profile there. We address this discrepancy by considering the *in situ* location of the H^+ ions, their relative mobility, and the cause of the dc conduction that produces an ECM signal. The exact nature of dc conduction in naturally formed ice remains unclear (*Wolff* (2000)); it is probably either ionic defects in the ice lattice, or conduction by dissociated H^+ ions in liquid-filled grain boundaries, or both of these causes. If ionic defects solely produce the ECM signal, then the near-zero ECM values suggest that H^+ ions are not in the lattice in the accreted ice. Because the mean crystal size in the accreted ice (0.20–1 m) is significantly larger than the diameter of the ice core, grain boundaries were rarely observed in the accreted ice (*Jouzel et al.* (1999)). This observation suggests that if grain-boundary conduction solely produces the ECM signal, then the near-zero ECM values are consistent with the lack of observed grain boundaries in the sampled accreted ice. Alternatively, the inclusions have a soluble part (*de Angelis et al.* (2004); *de Angelis et al.* (2005)) that could contain H^+ ions, and large inclusion densities are roughly correlated with peaks in the $[H^+]_{cb}$ profile (Figure 3.4a). If the H^+ ions remain within the isolated inclusions, where they are relatively immobile, then they are not expected to produce an ECM signal.

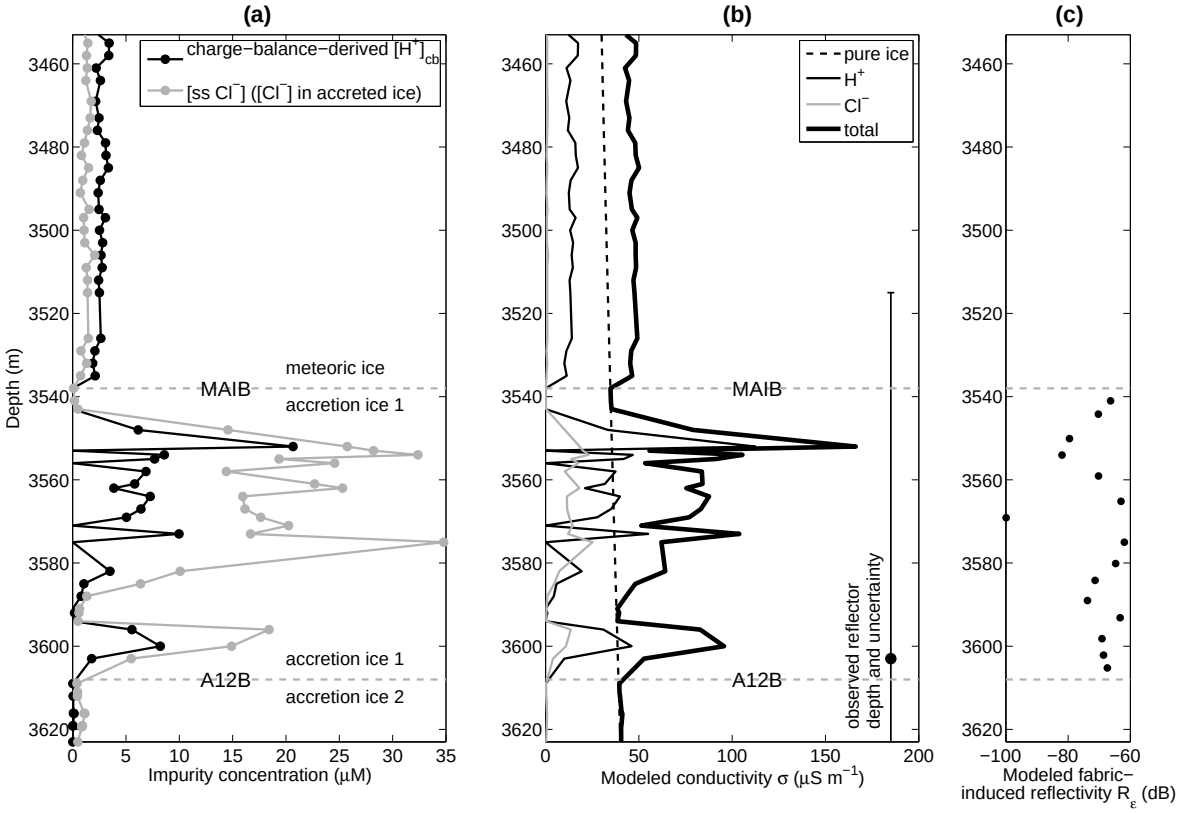

Figure 3.4: (a) $[Cl^-]$ and $[H^+]_{cb}$ vs. depth across the MAIB. Horizontal gray dashed lines show the isotope-identified MAIB and the primary boundaries between the accreted ices (*de Angelis et al.* (2004)). (b) Modeled pure, H^+, Cl^- and total conductivity vs. depth across the MAIB (equation 3). The conductivity contribution of ss Cl^- in the meteoric ice is near zero ($\sim 1\ \mu S\, m^{-1}$). (c) Modeled fabric-induced reflectivity inferred from c-axis data (only available for accreted ice 1).

The dielectric properties of the acid component of the conductivity model (μ_{H^+} and E_{H^+} in (3.3) were determined by laboratory measurements on meteoric ice cores and acid-doped ice. In those ice samples, the acid was likely at the grain boundaries, not in the ice lattice. This possible difference in acid location as compared to the Lake Vostok accreted ice may change these dielectric properties. If the H^+ ions are in the ice lattice, then they could be less mobile and have a smaller contribution to ac conduction. However, we have insufficient data to quantify this possible difference here. In summary, we cannot fully resolve the discrepancy between the $[H^+]_{cb}$ and ECM profiles and whether H^+ ions in the accreted ice contribute to the ac conductivity, so we therefore consider conductivity contrasts that both include and exclude the H^+ contribution to the conductivity.

[Cl⁻]

The mean and standard deviation of $[Cl^-]$ in the accretion ice is 10.7 ± 10.9 μM and its depth profile is shown in Figure 3.4a. Seawater-accreted ice with relatively low concentrations of $[Cl^-]$ (< 300 μM) behaves dielectrically in the same way as meteoric ice ($[\text{ss}\, Cl^-] <\sim 15$ μM) in that the Cl^- ions form ice-lattice defects (*Moore et al.* (1994a)). The largest value of $[Cl^-]$ in the Lake Vostok accreted ice is ~ 35 μM (Figure 3.4a), so all the Lake Vostok accretion ice is within the low concentration region that *Moore et al.* (1994a) observed. During freezing of the accreted ice, most of the Cl^- ions in the lake water could enter the ice lattice because $[Cl^-] \leq \sim 300$ μM, which is the solubility limit of Cl^- ions in the ice lattice (*Moore et al.* (1994a), *de Angelis et al.* (2004)). If the accreted ice crystals have not undergone much recrystallization, then the Cl^- solubility limit may be closer to 100–200 μM (*Moore et al.* (1994a)), but the $[Cl^-]$ values in the accreted ice are still much lower than this revised limit. Cl^- ions detected in meteoric ice are deposited either as HCl gas or as sea salt, but the conductivity contribution from Cl^- ions linearly depends only on the sea-salt Cl^- ions. The conductivity of the accreted ice would therefore be linearly dependent on $[Cl^-]$, rather than $[\text{ss}\ Cl^-]$. However, *de Angelis et al.* (2005) found that most of the Cl^- ions in the accreted ice exists as brine microdroplets, suggesting the Cl^- ions do not form defects in the ice lattice and therefore do not contribute to the conductivity. We therefore

consider conductivity contrasts that both include and exclude the Cl^- contribution to the conductivity.

3.4 Reflectivities in the Accreted Ice

3.4.1 Radar-Derived Reflectivities

The echo was detected in 5 separate segments that constitute about 2 km along a 10-km portion of the closest transect over the lake (Figures 3.3b–d). The echo intensity of each pick is measured as the maximum value within a 0.5-μs window around the reflections picked by *Tikku et al.* (2004), who used time-differentiated radargrams to enhance echo visibility. These echo intensities are close to the noise floor of the radar system. Despite these low values, the echo is visible and contiguous across many traces and is clearly not noise (Figure 3.3b). P_r is the mean echo intensity of the reflection where visible along CCx-X06a (-107.1 ± 0.3 dBm; 0 dBm = 1 mW), where the uncertainty is the standard deviation of the echo intensity of the visible reflections.

To estimate R from P_r using (3.1), it is necessary to estimate L and B. The depth profile of attenuation rate at the ice-core site (Figure 3.5) is modeled using the major-ion chemistry profiles, the composite borehole-temperature profile, the density profile, (3.3) and (3.2), following Chapter 2. To account for uncertainties in the dielectric properties used in the conductivity models, we distinguish between three different models: 1. The "reference" model uses the mean values of the dielectric properties with the adjustments to their values discussed in section 3.3.3, 2. The "high" model is simply the reference model plus the uncertainties in the dielectric properties, and 3. The "low" model is the reference model minus those uncertainties. The high models are labeled as such because increasing any of the dielectric properties will raise the value of L calculated using that model (the opposite is true for the low model). These distinctions are necessary because the modeled conductivity contrasts are calculated using the same conductivity model as for the estimates of L and R, so we must compare reflectivity values based on the same conductivity models.

Using the reference model, $L = -57$ dB along the two-way raypath of a radio wave to the MAIB at $\sim$ 3603 m. Uncertainty in the depth of the reflection near the ice-core site

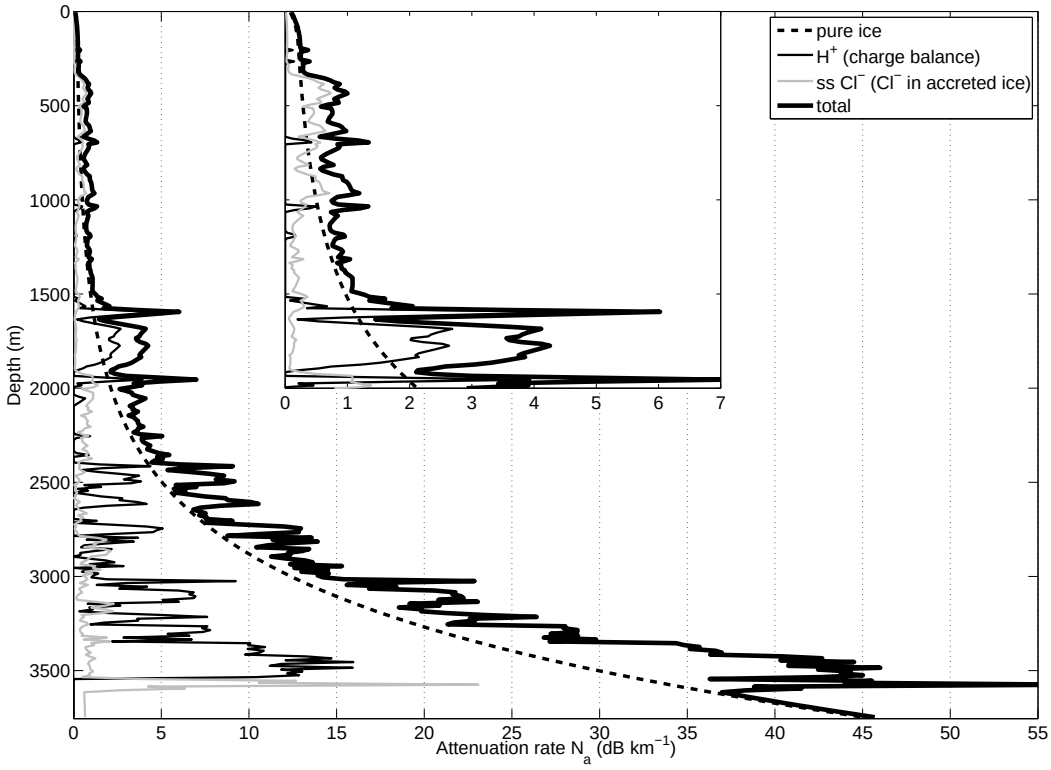

Figure 3.5: Depth profile of modeled one-way attenuation rate (N_a) at the ice-core site ((3.3) and (3.2)). The inset figure shows the same model results but with a narrower attenuation-rate scale for the top 2000 m to better show the contributions of the three components to the total modeled attenuation rate.

causes ±4 dB of uncertainty in L. The modeled one-way depth-averaged attenuation rate (N_a) to the reflection depth is -7.9 dB km^{-1}. This value is lower than most reported values of the depth-averaged attenuation rate (e.g., Chapter 2), primarily because of the lower ice temperatures at the ice-core site. Using the high model, $L = -66$ dB, and using the low model, $L = -50$ dB.

If $B < 0$ dB then the observed echo intensity can be explained by a larger value of R. The range of B is about 0 to -15 dB when the azimuthal angle between the radar-polarization plane and the vertical plane that includes the semi-major axis of the c-axis fabric (*Matsuoka et al.* (2003), *Fujita et al.* (2006)); this range is smaller if these two are nearly parallel or perpendicular to each other. The angle between CCx-X06a and the current ice-flow direction is about 70° (*Wendt et al.* (2006)). If the angle between the principal axes of the fabric and the radar profile is also about 70°, then the range of B is 0 to -3 dB (*Matsuoka et al.* (2003)). Because ice-crystal azimuths are unavailable from the ice core, we assume that $B = 0$ dB there.

Using equation 3.1 and the reference-model value of L (-57 dB), $R = -49$ dB. Using the high model of L, $R = -40$ dB, whereas using the low model for L gives $R = -56$ dB. Uncertainties in all the variables in (3.1) are included in the propagation-of-error calculation for R, but uncertainty in L dominates the uncertainty in R. The reference-model value of R is about one order of magnitude (10 dB) larger than the predicted reflectivities for most internal reflections in polar ice sheets caused by fabric, density or acidity contrasts (~ -60 to -80 dB; *Fujita and Mae* (1994)). However, this difference does not rule out that this reflection could be caused by one of those three causes, but rather that the respective dielectric contrast associated with the accreted ice may be larger than that typically observed in an ice sheet. For example, *Blindow* (1994) estimated the reflectivity of the MAIB in the Filchner–Ronne Ice Shelf to be -34 dB at 40 MHz, which is larger than most ice-sheet internal reflections.

3.4.2 Modeled Reflectivities From Ice-Core Data

Contrasts in both permittivity and conductivity can cause internal reflections in ice sheets (*Fujita and Mae* (1994)), and both may occur in the accreted ice. Here we separately model the permittivity and conductivity contrasts ($\Delta\varepsilon'_r$ and $\Delta\sigma$) using ice-core data and calculate their respective Fresnel reflectivities (R_ε and R_σ) following Paren [1981]:

$$R_\varepsilon = 20\log_{10}\left(\frac{\Delta\varepsilon'_r}{4\varepsilon'_r}\right), \tag{3.5}$$

$$R_\sigma = 20\log_{10}\left(\frac{\Delta\sigma}{8\pi f\varepsilon_0\varepsilon'_r}\right), \tag{3.6}$$

where f is the radio-wave frequency and ε_0 is the permittivity of the vacuum. We assume vertical incidence of the radio wave upon a planar interface. Because the available ice-core data are not continuous, we do not consider the possible effect of interference patterns between multiple dielectric contrasts separated by distances close to the radar wavelength (~ 3 m) (e.g., *Eisen et al.* (2003)).

Because of the differing frequency dependencies of R_ε and R_σ, multi-frequency radar data can be used to distinguish permittivity-induced reflections from conductivity-induced reflections (*Fujita et al.* (1999)). However, other airborne radar data collected over Lake Vostok (*Siegert et al.* (2000); *Tabacco et al.* (2002)) were collected at the same frequency (60 MHz) as the SOAR data used here, so we cannot determine the reflection cause using existing datasets and the multi-frequency method.

Insoluble mineral-inclusion contrast

Jouzel et al. (1999) found inclusions in the 70 m of accreted ice and a number-density peak near the top of the accreted ice. These inclusions contained both insoluble and soluble material. *Bell et al.* (2002) suggested that the reflection in question is due to the insoluble minerals in these inclusions. A strong radar layer in the Filchner–Ronne Ice Shelf was correlated with the depth of the MAIB identified in an ice core (*Oerter et al.* (1992)). At that MAIB, there were layers of clastic particles in addition to textural and chemical changes, so it is reasonable to consider whether the insoluble part of these inclusions could also cause the observed reflection at Lake Vostok. We evaluate this hypothesis by first estimating the

permittivity of the ice–inclusion mixture (ε'_{mix}) in terms of the size and permittivity of the inclusions (ε'_{incl}) using the Looyenga dielectric mixing equation (*Looyenga* (1965)):

$$\varepsilon'_{mix} = \left[\nu \left(\varepsilon'_{incl}\right)^{1/3} + (1-\nu)\left(\varepsilon'_{ice}\right)^{1/3}\right]^3, \tag{3.7}$$

where ν is the volume fraction of the insoluble inclusions in the ice and ε'_{ice} is the permittivity of pure ice that has no inclusions. We calculate R_ε using $\Delta\varepsilon'_r = \varepsilon'_{mix} - \varepsilon'_{ice}$ and equaton 3.5. To calculate the upper limit of R_ε, we assume that each inclusion is entirely composed of insoluble material.

The number of observed inclusions varies between 0 and 30 inclusions per meter length of ice core (m^{-1}) below the MAIB (the ice-core diameter is 10.8 cm). The largest and sharpest contrast in the inclusion density, which would presumably also produce the largest permittivity contrast, occurs about 10 m below the water-isotope-identified MAIB and is about 30 inclusions m^{-1}. The size of the inclusions varies between 0.3 and 1 mm (*Jouzel et al.* (1999), J.-R. Petit, pers. comm., 2008). We assume that the inclusions are spherical and we consider a range of possible inclusion diameters between 0.01 and 3 mm. *de Angelis et al.* (2004) suggested that the inclusion-rich upper portion of the accretion ice in the ice core is derived from sedimentary rocks, so we assume that ε'_{incl} ranges between 6 and 10, which is an approximate range for sedimentary rocks (e.g., *Keller* (1966)).

Because the magnitude of the linear inclusion-density contrast is well constrained relative to the inclusion size and value of ε'_{incl}, we hold the magnitude of the contrast fixed at 30 inclusions m^{-1} and vary only the other two parameters when calculating ε'_{mix}. Figure 3.6 shows that the reflectivity of an ice–inclusion mixture has only a weak dependence on the value of ε'_{incl} but has a stronger dependence on the inclusion diameter because of the cubic dependence of ν on inclusion diameter. For an inclusion diameter of 1 mm, $\Delta\varepsilon'_r = 7 \times 10^{-6}$ and the reflectivity is -125 ± 3 dB, where the uncertainty is the range of values of the reflectivity for the different values of ε'_{incl}. The inclusion-density contrast is less than 10 m^{-1} near the A12B and would produce a yet weaker reflection than the calculations we have shown here. Although the conductivity of the insoluble mineral inclusions is also expected to be different from ice, the reflectivity due to the expected conductivity contrast is yet smaller than the permittivity contrast and we neglect it here ($R_\sigma < -140$ dB or $\Delta\sigma < 0.01 \mu\mathrm{S\,m}^{-1}$

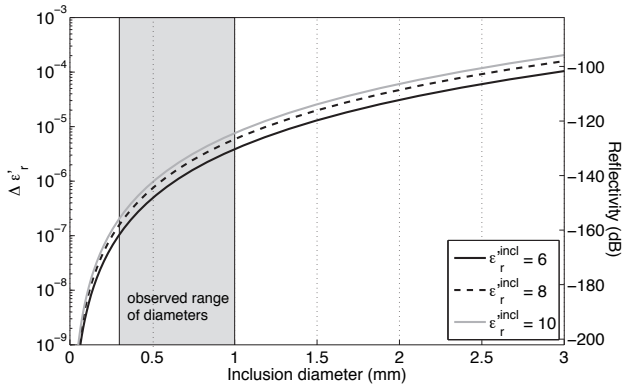

Figure 3.6: $\Delta\varepsilon'_r$ vs. inclusion diameter for several values of ε'_{incl} and equivalent Fresnel reflectivities (3.5). The area with gray fill shows the observed range of inclusion diameters (0.3–1 mm).

for 1-mm inclusions if $\sigma_{incl} = 1000\ \mu\mathrm{S\,m^{-1}}$).

Impurity-concentration contrast

We model the conductivity profile across the MAIB (Figure 3.4b) using the impurity-concentration and temperature profiles, (3.3) and the dielectric properties given in Table 3.2, and the adjustments to the impurity concentrations described in section 3.3.4. Temperature changes gradually, so the conductivity change due to temperature cannot cause a significant reflection.

The largest conductivity contrast occurs between 3543–3552 m near the MAIB, and there are several other contrasts that exceed 40 $\mu\mathrm{S\,m^{-1}}$. Using the reference model and (3.6), $\Delta\sigma = 131\ \mu\mathrm{S\,m^{-1}}$ between 3543–3552 m, equivalent to a reflectivity of −50 dB. $\Delta\sigma = 154$ and 108 $\mu\mathrm{S\,m^{-1}}$ using the high and low models, respectively, and their equivalent reflectivities are −49 and −52 dB, respectively. If we exclude the H^+ component of the conductivity in the accreted ice, then $\Delta\sigma = 23.4\ \mu\mathrm{S\,m^{-1}}$ for the reference model and the reflectivity is −65 dB. Alternatively, if we exclude the Cl^- component of the conductivity, then $\Delta\sigma = 113\ \mu\mathrm{S\,m^{-1}}$ and the reflectivity is −51 dB. The depth of the radar-observed reflection is close to the A12B and there is also a modeled conductivity decrease near that

depth (Figure 3.4). The magnitude of this decrease is less than half of the magnitude of the maximum increase near the MAIB at ~ 3548 m and could produce a reflectivity of -58 ± 2 dB, depending on the conductivity model used, which is 8 dB weaker than that produced by the shallower but larger increase near the MAIB.

Fabric contrast

A change in crystal-orientation fabric below the MAIB could cause a significant permittivity contrast and an observable reflection (e.g., *Fujita et al.* (1999), *Matsuoka et al.* (2003); *Eisen et al.* (2007)). The largest change in *c*-axis orientations in the accreted ice below the MAIB is 45°. The largest change in c-axis orientations in the accreted ice below the MAIB is 45°. Azimuths of the *c*-axis orientations are unavailable, so these data are not ideal for calculating the reflectivity of the fabric contrast. However, assuming the *c* axes align in the radar polarization plane, the largest reflectivity due to such a fabric contrast ($\Delta\varepsilon'_r = 0.010$) at the ice temperature of the MAIB (−7°C) is -61.9 ± 0.7 dB (*Fujita and Mae* (1994); *Matsuoka et al.* (1997b); (3.5)), where the uncertainty is due to uncertainty in the value and temperature dependence of the permittivity anisotropy. This reflectivity value occurs just above the A12B, but reflectivities within 1 dB of this value occur at several depths between 3538 and 3609 m (Figure 3.4c).

Ice-fabric data are limited because the ice crystals are very large,so larger fabric contrasts may occur elsewhere in the accreted ice over Lake Vostok. The maximum possible reflectivity due to fabric is -51.2 ± 0.7 dB, which occurs when the fabric changes between a single vertical pole and a single horizontal pole. Such a fabric contrast can exist in sea ice (e.g., *Jeffries et al.* (1993)), but it has been observed neither in meteoric ice, nor in marine ice accreting underneath ice shelves (e.g., *Oerter et al.* (1992)) which is a closer analog to the Lake Vostok accreted ice. A more realistic fabric change from a single pole to purely random is considered the plausible upper limit of fabric changes in ice sheets (*Fujita and Mae* (1994)) and has a reflectivity of -60.7 ± 0.7 dB. Our maximum value here (−61.9 dB) is close to this likely upper limit.

Density contrast

A density contrast greater than 10 kg m^{-3} is necessary to produce a reflectivity equivalent to the reference-model radar-derived reflectivity (−49 dB) using (3.5). No such density contrasts exist in the meteoric ice below a depth of 160 m, but no ice-density data are available below 2540 m. Because water has a higher density than ice, the accreted-ice/lake-water mixture should have a higher density than pure ice near the ice–lake interface prior to complete consolidation of the frazil ice crystals. However, we are interested in the ice properties more than 100 m above the ice–lake interface, where the consolidation process should be complete. We therefore neglect the possibility of a significant reflection due to an ice-density contrast near the MAIB or the A12B.

3.5 Discussion

3.5.1 Probable Reflection Cause

Here we discuss the probable reflection cause based on comparisons between the radar-derived reflectivity (section 3.4.1) and the modeled reflectivities (section 3.4.2), and between the depths of the reflector and the modeled reflectivities. Table 3.3 and Figure 3.7 summarize the radar-derived and modeled reflectivities near both boundaries. The calculation of both the radar-derived reflectivities and conductivity-induced modeled reflectivities required a conductivity model. However, there is no significant circularity in comparing these values because the ice-core-based reflectivities are based only on data from the accreted ice, whereas the radar-derived reflectivities are based on modeled conductivities from the surface to the depth of the reflection.

Of the known reflection causes of radio waves in polar ice sheets, the reflectivity 10 m below the MAIB due to the modeled conductivity contrast (including the H^+ and Cl^- components) using the reference conductivity model is closest to the radar-derived reflectivity (only 1 dB lower). At this depth, the high model gives a conductivity-induced reflectivity that is 8 dB smaller than the radar-derived reflectivity derived with the high model; similarly, the low model produces a reflectivity that is 4 dB larger than radar-derived value. The reflectivity due to the $[Cl^-]$ contrast by itself is 11–17 dB lower than the radar-derived

Table 3.3: Radar-derived and modeled reflectivities near the MAIB and the A12B.

	Reflectivity (dB)					
	Near the MAIB ($\sim$ 3538 m)			Near the A12B ($\sim$ 3608 m)		
Reflection cause	Ref.	High	Low	Ref.	High	Low
Radar-derived	-49	-41	-57	-49 [a]	-41 [a]	-57 [a]
Inclusion-density contrast	-125 ± 3 [b]	...	...	negligible	...	...
$[Cl^-]$ contrast	-65	-63	-67	-70	-68	-74
$[H^+]$ contrast	-51	-50	-53	-59	-58	-60
$[H^+]$ and $[Cl^-]$ contrasts	-50	-49	-52	-58	-56	-59
Crystal-orientation fabric	-62 [b], -51 [b,c]	...	...	-62 [b], -51 [a,b,c]	...	...
$[H^+]$, $[Cl^-]$ and fabric	-50	-49	-51	-56	-55	-57

"Ref." means that the mean values of the dielectric properties (excepting pure ice) were used as the conductivity-model parameters, whereas high and low models represent models where the dielectric properties were adjusted by their uncertainties (section 3.4.1). [a] Values are the same for MAIB and A12B. [b] These values do not depend on the choice of conductivity model and are not repeated. [c] Upper limit of possible fabric contrasts (section 3.4.2).

reflectivity, so it cannot satisfactorily match the radar-derived reflectivity, especially given the likelihood of Cl^- ions being trapped in brine microdroplets rather than in the lattice. Alternatively, the reflectivity of the conductivity contrast near the A12B (-59 dB) is close to the low-model radar-derived reflectivity.

The estimated reflectivity due to 1-mm mineral inclusions is more than 60 dB lower than the radar-derived reflectivity, so it is very unlikely that the inclusion contrast near the MAIB produced the observed reflection. The reference-model radar-derived reflectivity is more than 10 dB larger than the maximum predicted reflectivity from the available fabric data. However, the low-model reflectivity is close to the fabric-induced reflectivity, so a fabric change may be sufficient to explain the radar-derived reflectivity.

The reflection in question is detected along several flowbands that originate along the shoreline north of the bay, but it is not consistently detected near the western/upstream shoreline (Figure 3.1b). If impurity-rich accreted ice 1 forms only within the shallow bay (Figure 3.2), as suggested by *de Angelis et al.* (2004), and its possible reflection-causing

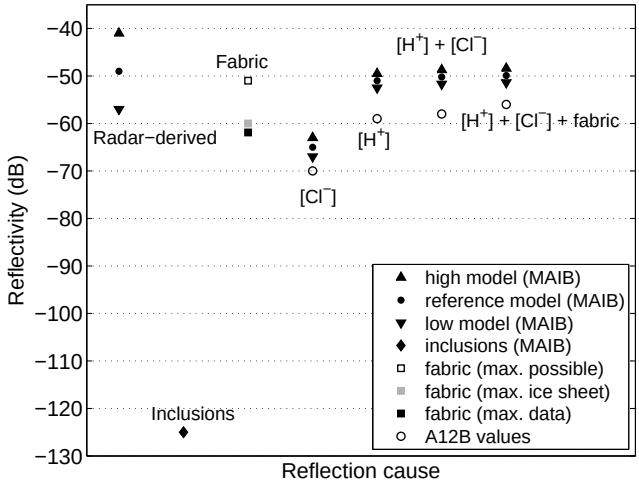

Figure 3.7: Comparison between reflectivity values for different reflection causes and conductivity models listed in Table 3.3. For the impurity-contrast-induced reflectivities, the low/ high model values are only shown for the MAIB. For fabric, the three squares represent the three fabric contrasts discussed in section 3.4.2 ("max. data": maximum value inferred from c-axis orientation data; "max. possible": contrast between single vertical and horizontal pole; "max. ice sheet": contrast between a single vertical pole and randomly oriented fabric).

properties are unique to this bay, then it is difficult to reconcile a reflection originates within accreted ice 1 (near the MAIB) with the spatial pattern of detection of the reflection. Most of the upstream shoreline in the southern half of the lake is abrupt, lacking bays that could produce ice similar to accreted ice 1. This problem further suggests that the $[H^+]$ contrast near the A12B and within accreted ice 1 cannot explain the observed reflection elsewhere over the lake. The proximity of the reflection's depth to the A12B (Figure 3.2) and its spatial pattern of detection suggest that it originates at the A12B. However, if the reflection originates at the A12B, then we must dismiss the remarkably large changes in ice properties that occur at the MAIB that could also cause a reflection. A $[Cl^-]$ contrast can, at most, only have a minor contribution to this reflection cause. Either an $[H^+]$ contrast or a fabric contrast can plausibly explain the magnitude of the radar-derived reflectivity, although there are uncertainties associated with the magnitude of the $[H^+]$ contrast, the location of these ions in the accreted ice and their conduction mechanism (section 3.3.4).

Based on the above considerations of the depth and magnitude of the modeled reflectivities, we argue that the probable reflection cause is a fabric contrast at the A12B.

We modeled the reflection as a single planar interface, and we did not consider the possibility of multiple reflectors interfering together to produce the observed reflection. Interference should be considered if multiple fabric contrasts are present and are separated by depths that are small compared to the wavelength of radio wave in the ice ($\sim$ 3 m). Available fabric data are sparse due to the size of the ice crystals, so we cannot assess interference effects from fabric contrasts. However, such effects cannot migrate the reflections depth more than the radar resolution ($\sim$ 20 m), equivalent to half of the pulse width (250 ns).

3.5.2 Implications For Radar Detection of Accreted Ice and Accretion Mechanisms

Accreted ice has been detected within several Antarctic ice shelves, but the discovery of the reflection above Lake Vostok is the only known example of direct radar detection of accreted ice above a subglacial lake, although it has been be indirectly inferred elsewhere (e.g., *Tikku et al.* (2005)). The spatial pattern of detection of the reflection (Figure 3.1b) can be better used to study the icelake interface if its reflection cause is specified. We argue that the observed reflection is primarily due to a fabric contrast at the A12B (section 3.5.1), which suggests several conditions necessary for radar detection of accreted ice at Lake Vostok. We expect that conditions similar to those that produced the A12B were present at or near the origin of the A12B upstream from the ice-core site.

There are several modeling studies predicting water-circulation patterns in Lake Vostok and melt/accretion patterns at its ice–lake interface. *Wüest and Carmack* (2000) predicted that accretion would occur where water is supercooled and flows upslope along the ice–lake interface, i.e., where the shallowest water is traveling southwards. They also predicted that freezing of lake water over the main lake along the Vostok flowline would not begin until the ice reaches the central part of the lake, and this prediction roughly agrees with our interpolated reflection depths along the flowline (Figure 3.2). Using thermomechanical ice-flow models constrained by ground-based radar data along the Vostok flowline, *Salamatin*

et al. (in press) predicted that accretion rates would be fastest at the upstream shoreline, decreasing exponentially as the ice sheet passes over the lake. *Thoma et al.* (2008) numerically modeled the water circulation using updated ice-thickness and lake-bathymetry maps, and they also predicted that freezing would mostly occur near the shoreline and in the southern end of the lake. Their preferred model of the accreted-ice thickness shares some features with that of the spatial pattern of radar detection of the accreted ice (Figure 3.1b), including sectors of thinner and thicker accreted ice along flowbands originating at the center and southern end of the western shoreline. This match is not perfect, which may be partly due to the apparent sensitivity of their modeling to the ice-thickness, lake-bathymetry, and ice-flow-direction models that they used. The reflection was detected only along flowbands that originated at bedrock ridges on the western shoreline, where basal meteoric ice descends abruptly onto the lake (*Tikku et al.* (2004)), but the reflection is not always detected where those flowbands enter the lake (Figures 3.1b and 3.2). *Thoma et al.* (2008) predicted that accretion rates along the upstream shoreline would vary by more than a factor of two, and areas where they predicted faster accretion rates are generally coincident with the origin of the bedrock-ridge flowbands, e.g., the center of the western shoreline. This link suggests that faster accretion rates are a necessary condition of detection of the accreted ice. At Lake Vostok, the reflection is often barely detectable above the noise floor of the SOAR radar system (Figure 3.3d), supporting the idea that areas with insufficiently rapid initial accretion rates will produce difficult-to-detect accreted ice.

We do not yet know why the fabric contrast would be larger where the accretion rate is initially faster. The large size of the accreted-ice crystals may be due to abnormal grain growth after the initial freezing (*Montagnat et al.* (2001)). Faster initial accretion rates may alter this process so that abnormal grain growth more strongly favors single-crystal growth (that has a single c-axis orientation), producing a larger fabric contrast with the meteoric, deformed basal ice.

Another possible explanation for the spatial pattern of detection of the reflection is that the attenuation of the ice column is lower along the flowbands that descend onto the lake from bedrock ridges. An ice sheet that has a nearly flat surface is thinner on bedrock ridges than adjacent troughs, so basal temperatures may be lower on ridges. We estimated

this basal temperature difference using a simple, steady state one-dimensional temperature model that does not include horizontal heat advection (*Paterson* (1994), p. 218). The inputs for this model are an ice-equivalent accumulation rate of 2.2 $\mathrm{cm\,a^{-1}}$ (*Parrenin et al.* (2004)), a surface temperature of $-54.3°\mathrm{C}$ (V.Y. Lipenkov, pers. comm., 2006) and a geothermal flux of 44 $\mathrm{mW\,m^{-2}}$ (*Petit* (2003)). Using this temperature model, the basal temperature difference between a bedrock ridge and a trough on the western shoreline that has a typical ice-thickness difference of 600 m (Figure 3.1a) is greater than 5 K. These lower ice temperatures for ice descending from the bedrock ridges would initially lower the roundtrip attenuation significantly, although the ice temperatures of flowbands from the bedrock ridges and troughs will equilibrate as the ice flows over the lake. Using the above modeled temperature–depth profiles and the mean values of $[\mathrm{H^+}]$ and $[\mathrm{ss\,Cl^-}]$ for the Vostok ice core, the roundtrip-attenuation difference at the shoreline could be more than 10 dB for a 3500-m-thick ice column versus that for a 2900-m-thick ice column. Given that the reflection is often barely detectable above the noise floor of the SOAR radar system (Figure 3.3d), relatively small differences in the roundtrip attenuation could affect detection of the accreted ice. This alternative explanation does not require that accretion rates be faster near the shoreline. Further work investigating the spatial variation of attenuation in the Lake Vostok region is necessary to fully evaluate this possibility.

At Lake Vostok, the total loss due to radar attenuation to the depth of the reflection is relatively low for its large depth because of the low ice-sheet temperatures over Lake Vostok. This setting and the low noise floor of the radar system also contribute to the radar detection of the accreted ice there. To detect potentially weaker echoes, either the radioglaciological conditions must be more favorable (i.e., lower attenuation due to lower temperatures or impurity concentrations) or the radar-system characteristics must be improved (e.g., lower noise floor). A ground-based operation with the same system characteristics as the SOAR airborne radar used at Vostok, i.e., $h = 0$ m in (3.1), would only decrease the geometric spreading loss by 1 dB and would not significantly improve detection of weak echoes. Radar systems with larger depth penetrations and beam focusing are necessary to further delineate and characterize accreted ice over Lake Vostok and other subglacial lakes.

3.6 Conclusions

Airborne radar data and ice-core data were used to evaluate possible causes of the accreted-ice reflection observed at Lake Vostok. The deep reflection over Lake Vostok is large for an internal reflection, and we determined that it was probably caused by the fabric contrast observed near the A12B in the Vostok ice core. We found that it is very unlikely that insoluble mineral inclusions could produce a detectable reflection, and that a Cl^- contrast could have only a secondary contribution (if any) to the observed reflectivity. An acidity contrast found in ice that presumably only forms in the shallow bay cannot explain radar detection of accreted ice over most of the southern half of the lake. Faster accretion rates could increase the fabric contrast and may be a necessary condition for radar-detectable accreted ice, if the fabric contrast causes the reflection. This reflection cause also implies that there is accreted ice at Lake Vostok and at other subglacial lakes that has yet to be detected by radar. Multi-frequency radar data could help resolve the lingering uncertainty as to the cause of the reflection (e.g., *Fujita et al.* (1999)) by determining whether the reflection is due to a permittivity or conductivity contrast. A more powerful radar system could also help detect weak reflections close to the systems noise floor. Active seismic surveys can also detect englacial fabric contrasts (e.g., *Horgan et al.* (2008)) and could confirm our hypothesis. Finally, new and deeper ice-core data from upcoming coring operations at Vostok should provide further insight into the nature of the accreted ice and the observed reflection.

More subglacial lakes continue to be discovered, some of which have a significant influence on ice flow (*Bell et al.* (2007)), and ice accretion can also alter the rheology of an ice shelf (*Larour et al.* (2005)). Interpreting the radar detection of accreted ice over subglacial lakes and ice shelves will therefore lead to a better understanding of ice masses that interact with an underlying lake or ocean.Impurity contrasts between meteoric and accreted ice in ice shelves are typically at least an order of magnitude larger than those observed at Lake Vostok (e.g., *Moore et al.* (1994a)), and the reflectivity of the MAIB there can also be larger (*Blindow* (1994)), so this reflection mechanism may be dominant there, rather than a fabric contrast.

Chapter 4

MILLENNIALLY AVERAGED ACCUMULATION RATES FOR THE LAKE VOSTOK REGION INFERRED FROM DEEP INTERNAL LAYERS

This chapter was submitted to Annals of Glaciology in April 2008, as part of the International Symposium on Radioglaciology and its Applications, and it was revised and resubmitted in September 2008. My co-authors are Kenichi Matsuoka, Michelle Koutnik, Ed Waddington, Michael Studinger and Dale Winebrenner. I wrote the text and conducted most of the work described in this chapter, including the integration of existing datasets, adaptation of the inverse model and interpretation of the results. Kenichi Matsuoka guided my work and extensively edited the manuscript. Michelle Koutnik and Ed Waddington guided the application of the inverse model and edited the manuscript. Michael Studinger provided several datasets, guided the work in the context of previous studies of Lake Vostok and edited the manuscript. Dale Winebrenner guided the comparison with satellite-microwave-derived accumulation-rate maps and edited the manuscript. Frédéric Parrenin was the scientific editor for this manuscript, and it was reviewed by Olaf Eisen and Andrey Salamatin.

4.1 Summary

Accumulation rates and their spatiotemporal variability are important boundary conditions for ice-flow models. The depths of radar-detected internal layers can be used to infer the spatial variability of accumulation rates. Here we infer accumulation rates from three radar layers (26-, 35- and 41-ka old) in the Lake Vostok region using two methods: the local-layer approximation (LLA) and a combination of steady-state flowband modeling and formal inverse methods. The LLA assumes that the strain-rate history of a particle traveling through the ice sheet can be approximated by the vertical strain-rate profile at the particle's current position, which we further assume is uniform. The flowband model, however, can account for upstream strain-rate gradients. We use the LLA to map accumulation rates over

a 150-km by 350-km area and apply the flowband model along four flowbands. The LLA accumulation-rate map shows higher values in the northwestern corner of our study area and lower values near the lake's upstream shoreline. These features are also present but less distinct in the flowband accumulation-rate profiles. The LLA-inferred accumulation-rate patterns over the three time periods are similar, suggesting that the regional pattern did not change significantly during the last $\sim$ 25 ka of the last glacial period. However, the accumulation-rate profiles inferred from the flowband model suggest changes during that period of up to 1 cm a^{-1}, or $\sim$ 50% of the inferred values.

4.2 Introduction

Lake Vostok, East Antarctica, is the world's largest known subglacial lake (*Kapitsa et al.* (1996)). Its interaction with the overlying East Antarctic ice sheet, through mass and energy exchange and reduction of basal drag, is of considerable glaciological interest (e.g., *Bell et al.* (2002); *Pattyn et al.* (2004)). Radio-echo intensities of the ice–lake interface could potentially delineate regions of basal melting and accretion over the lake, but such analysis requires estimates of the radar attenuation over the lake, which is strongly temperature dependent (e.g., Chapter 2). Ice-flow models can predict ice temperatures, but such models require maps of accumulation rates and their temporal variations to make accurate predictions. Mapping accumulation rates over the Lake Vostok region is therefore valuable for future glaciological studies there as well as the paleoclimatic interpretation of the Vostok ice core (e.g., *Parrenin et al.* (2004)) and possible future ice cores in this region.

Acquiring extensive field-based accumulation-rate measurements is a significant undertaking (e.g., *Dahe et al.* (1994)). However, such field data are inevitably sparse relative to the size of Antarctica and are subject to significant interannual and spatial variability, complicating the interpretation of trends in those data (e.g., *Magand et al.* (2007)). Atmospheric modeling can estimate regional-scale accumulation rates (e.g., *Rignot et al.* (2008)) but have low spatial resolution and must be corrected for model biases using other observations (*Magand et al.* (2007)). Satellite-microwave data (e.g., *Arthern et al.* (2006)) can be used to interpolate field-based measurements, but the spatial resolution of the satellite data is limited (25 km). This resolution is generally not fine enough to capture local accumulation-rate

anomalies, e.g., an apparent accumulation-rate high along the western/upstream shoreline of Lake Vostok (*Leonard et al.* (2004)).

Here we infer the spatial pattern of accumulation rates in the Lake Vostok region averaged over three time periods dating back to 41 ka using layer-depth data from a gridded airborne radar dataset collected over this region (Figure 4.1). We use both a steady-state flowband model with inverse methods and a local one-dimensional strain-rate model to infer accumulation rates. The former approach considers the effects of both upstream accumulation-rate gradients and ice-thickness gradients upon the layer shapes, while the latter approach ignores them. We apply the flowband model along four flowbands and compare accumulation rates inferred from this method to an accumulation-rate map for the entire study area based on the simpler model that neglects upstream strain-rate gradients. We also discuss temporal changes of the accumulation-rate pattern over the three layer ages and compare our accumulation-rate map to previous estimates for this region.

4.3 Data and Methods

4.3.1 Radar Data

We use the 60-MHz airborne ice-penetrating radar data collected over the Lake Vostok region in an approximately 150-km by 350-km grid by the U.S. Support Office for Aerogeophysical Research (SOAR) at the University of Texas Institute for Geophysics. *Blankenship et al.* (2001)) described the system characteristics. This dataset was used to derive both the surface and bed topographies (*Studinger et al.* (2003)). The radar lines were flown along an orthogonal grid; lines with a roughly E–W orientation had a 7.5-km line spacing, and lines with a roughly N–S orientation had an 11.25- or 22.5-km line spacing (Figure 4.1d). N–S profiles with the smaller line spacing were closer to the shoreline because the aerogeophysical surveys main goals were to delineate the lake shoreline and to determine the geological controls on the lake. From these data, we use the two shallowest internal layers picked by *Tikku et al.* (2004)) (layers A and B) that were traceable over most of our study area (Figures 4.1a–b), and another picked for this study (layer C, the deepest layer; Figure 4.1c). The layer and bed depths were calculated using a radio-wave speed of 168.4 m μs^{-1}

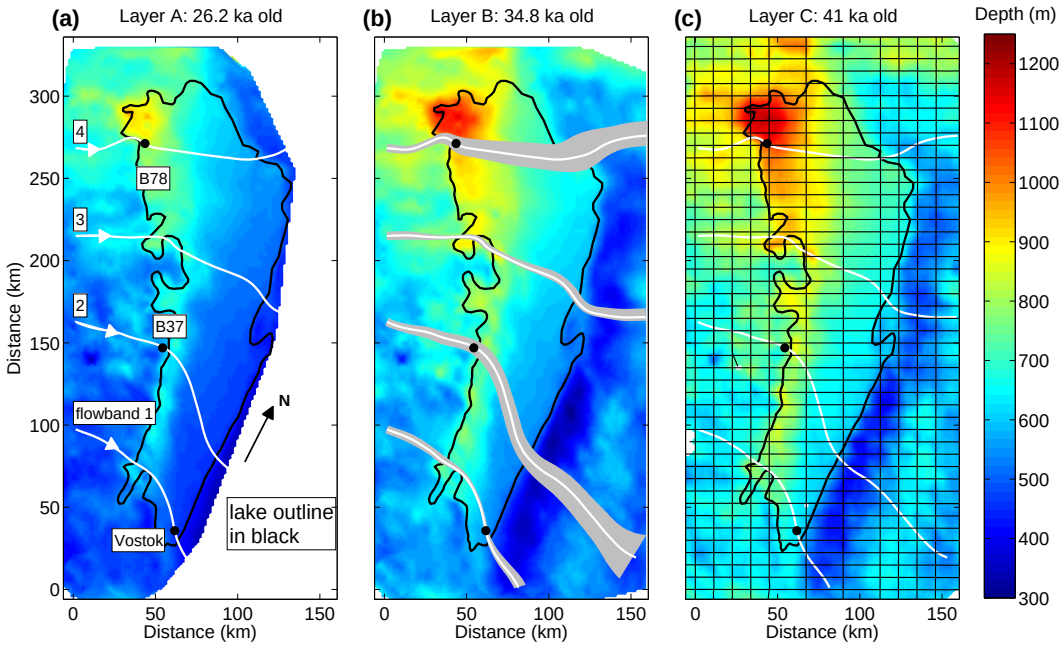

Figure 4.1: (a–c) Color maps of the depth to the three internal layers (A–C) used in this study. Layer A could be tracked over only about two-thirds of the study area. The center flowlines of the four flowbands (1–4) are shown as white lines and labeled at the head of the flowbands, and the flow directions are shown with white arrows. The locations of surface-velocity and surface accumulation-rate data are labeled. The edge of Lake Vostok is outlined in black. The gray fill around each center flowline in (b) shows the flowband's width variation. The start of each flowband has the same width (5 km). The black lines in (c) are the airborne-radar flight lines.

averaged over the ice column to the ice–lake interface (*Popov et al.* (2003)), and the layer depths varied between 334–1290 m. The layer, surface and bed elevations were linearly interpolated onto a 1.5-km grid. The location of the lake shoreline is determined as the edges of the region where the bed echo is bright and flat (*Studinger et al.* (2004)).

We estimated the layer ages by first interpolating the gridded layer depths to the Vostok ice-core site and then linearly interpolating the depth–age scale for the ice core (*Parrenin et al.* (2004)) to each layer's depth there. From shallowest to deepest, the layers labeled A, B and C are 26.2-, 34.8- and 41.0-ka old, respectively. We assign an uncertainty of 2.0 ka these layer ages (5–8% of their ages), because of the uncertainty in the layer depths, the uncertainty in the depth–age scale, and the layer-depth interpolation that was used.

4.3.2 Inferring Accumulation Rates From Layer Depths

There are several approaches to inferring accumulation rates from internal-layer depths in ice sheets (*Waddington et al.* (2007)). The simplest approach is the shallow-layer approximation (SLA), where the accumulation rate $\dot{b}$ is equal to the ice-equivalent layer depth z divided by its age A. However, the shallow-layer approximation is valid only for very shallow layers ($< 1\%$ of ice-sheet thickness) that have not yet experienced significant cumulative dynamic strain. For deeper layers, the local-layer approximation (LLA) may be valid. The LLA assumes that the actual strain-rate history of a particle traveling through the ice sheet can be approximated using the vertical strain rate profile at its current location. If we further assume that the vertical strain rate is uniform with depth, the LLA can be used to infer accumulation rates $\dot{b}_{LLA}$ from the layer depths and ice thickness H as

$$\dot{b}_{LLA} = -\ln\left(1 - \frac{z}{H}\right)\frac{H}{A}. \tag{4.1}$$

This approach has been previously applied to radar data from the Lake Vostok region (e.g., *Siegert* (2003)). However, as also acknowledged by *Siegert* (2003), the LLA is not appropriate for deep internal layers composed of particles that have traveled significant horizontal distances and thus experienced non-steady and non-uniform strain-rate patterns. To quantify the suitability of the LLA, *Waddington et al.* (2007) defined the non-dimensional depth number D. This number is based on the relationship between the horizontal distance

(L_{path}) that a particle has traveled from the surface to that layer, and the characteristic length scales of accumulation-rate ($L_{\dot{b}}$) and ice-thickness variability (L_H) as

$$D = L_{path}\left(\frac{1}{L_{\dot{b}}} + \frac{1}{L_H}\right), \tag{4.2}$$

If $D \ll 1$, the layer is not "deep", so that the spatial gradients in accumulation rates and ice thickness do not significantly affect the layer depths, and hence the LLA is sufficiently accurate to infer accumulation rates. We note that values of D help determine where the LLA is applicable, but there is no simple quantitative relationship between D and uncertainty in $\dot{b}_{LLA}$. L_{path} is the product of the layer age and the depth-averaged horizontal velocity $\bar{u}$ experienced by the particle as it traveled along its trajectory from the surface to the layer:

$$L_{path} = \bar{u}A. \tag{4.3}$$

We use the measured surface speed at Vostok station (2 $\mathrm{m\,a^{-1}}$; *Wendt et al.* (2006)) to approximate $\bar{u}$ over the entire study area. At Vostok station, the measured surface speed should be equivalent to $\bar{u}$ because the vertical profile of horizontal velocity is uniform for floating ice. Characteristic lengths $L_{\dot{b}}$ and L_H are derived from the along-flow (x-direction) gradients in $\dot{b}$ and H, respectively:

$$L_{\dot{b}} = \left|\frac{1}{\dot{b}}\frac{d\dot{b}}{dx}\right|, \tag{4.4}$$

$$L_H = \left|\frac{1}{H}\frac{dH}{dx}\right|. \tag{4.5}$$

To calculate $d\dot{b}/dx$ and dH/dx, we use $\dot{b}_{LLA}$ and H values averaged over 60 km along-flow, which is close to the mean L_{path} value for the three layers (68 km). Because our goal is to evaluate the suitability of the LLA, these $d\dot{b}/dx$ values should be of the correct order of magnitude and thus adequate for the principal purpose of calculating D.

4.3.3 Flowband Model and Inverse Solution Procedure

A method that can provide more accurate accumulation-rate patterns from deeper layers is a combination of flowband modeling and formal inverse theory. We use the steady-state flowband model and inverse solution procedure described by *Waddington et al.* (2007), and

we refer the reader to that study for full details of that model. An inverse problem begins by solving a forward problem that is the set of governing equations, boundary conditions and parameter values. In our forward problem, a flowband model calculates layer depths using steady-state ice-surface elevations, ice velocities and temperatures. It is a 2.5-dimensional ice-flow model whose flowband width can vary, but it assumes that all properties are uniform transverse to the direction of ice flow. The flowband model also requires initial estimates of the layer age and the input ice flux at the upstream end of the flowband. This ice flux is estimated kinematically using the width, ice thickness and estimated depth-averaged horizontal velocity at the start of the flowband. Uncertainty in the ice flux is set at 50% of its estimated value, because of the uncertainty in past accumulation rates (section 4.3.4). The ice flux and layer age are adjusted by the inverse solution procedure as necessary to match the data.

Flowbands were identified using the long-term flow directions determined by *Tikku et al.* (2004) using structure tracking in the internal layers, not modern surface-slope gradients. At Vostok station, their flow direction matches the modern flow direction determined by *Wendt et al.* (2006)) to within 7°. We do not use modern streamlines because they are difficult to constrain, due to the low surface slopes over the lake (Figure 4.1a) and the limited spatial extent of reliable surface-velocity data. None of the airborne-radar profiles followed ice flowlines, so we calculated flowlines within the gridded flow field and linearly interpolated the layer, surface and bed elevations along them. We chose four flowbands that traversed Lake Vostok, evenly divided the study area, and took advantage of available surface-velocity and accumulation-rate data. The southernmost flowband (labeled "1") passes through Vostok station (Figure 4.1a). Flowbands 2 and 4 pass through sites B37 and B78, respectively, for which modern accumulation-rate data are available. Flowband 3 crosses the lake roughly halfway between flowband 2 and 4. We calculated the flowband widths by finding two flowlines that began 2.5 km away from the start of the center flowline and normal to the initial direction of flow, and then calculating the distance between those two flowlines (the edges of the flowband) along-flow. The flowband widths vary between 40% (flowband 1) and 620% (flowband 2) of their initial values.

Although ice temperatures and strain rates can strongly influence each other, the temper-

ature and mechanical components of our flowband model are not coupled. Depth-averaged horizontal velocities are determined kinematically, and the vertical profiles of horizontal velocity are calculated by multiplying temperature-dependent non-dimensional shape functions by the depth-averaged horizontal velocity. The vertical velocities are then derived from the horizontal velocities using local incompressibility. Because there is no basal drag over the lake, the shape functions should be uniform and equal to unity there. Those shape functions are adjusted so that the initial temperature-dependent shape functions are closer to uniform values; they are not exactly uniform but are smoothed so that there is no velocity discontinuity at the edges of the lake.

To calculate ice temperatures along the flowlines for the temperature-dependent vertical shape functions of horizontal velocity, we use a one-dimensional steady-state temperature model that includes vertical, but not horizontal, advection and diffusion of heat (*Paterson* (1994), p. 218). We horizontally smooth the two-dimensional temperature field formed from this set of one-dimensional profiles over a length scale of approximately 5 km (116–200% of ice thickness) to approximate the effects of horizontal advection and diffusion of heat, which are neglected in the temperature model. This temperature model neglects basal melting and freezing that occur over the lake because these rates are small relative to the accumulation rates (*Wendt et al.* (2006)) and are not yet well constrained over the entire lake. However, one recent model suggested that there is significant spatial variability in the melting/freezing pattern and predicted basal freezing rates greater than 5 $\mathrm{cm\,a^{-1}}$ near the western shoreline (*Thoma et al.* (2008)), which would affect the layer depths and hence accumulation rates inferred using this model.

The layer depths generally shallow as the ice flows across the lake (Figure 4.4). However, the layers in the northern part of the lake (flowband 4 in Figure 4.4k), where basal melting is predicted (e.g., *Thoma et al.* (2008)), shallow more abruptly than those layers in the southern part of the lake, where basal accretion has been observed (*Bell et al.* (2002); *Tikku et al.* (2004)). This layer-depth pattern suggests that basal melting and accretion have less influence upon the layer depths used in this study than transverse strain rates, which generally increase, causing layer thinning, as the flowbands widen over the lake.

For a given along-flow accumulation-rate profile and boundary conditions, the flowband

model produces a velocity field, from which modeled isochronous layers are calculated. We then compare the depths of our modeled layers to those of each dated internal layer in our study area. The initial values of the accumulation rates ($\dot{b}_{LLA}$), input ice flux, and layer age are adjusted iteratively using an inverse solution procedure that seeks the best accumulation-rate pattern ($\dot{b}_{fb}$), which is the pattern that is spatially smooth and that fits the layer-depth, surface-velocity and accumulation-rate data at an expected tolerance based on the data uncertainties. We must incorporate these uncertainties using an expected tolerance because overfitting the data can produce spurious variations in $\dot{b}_{fb}$. Our solution is one whose $\dot{b}$ profile has a low curvature and whose modeled input flux and layer age have small deviations from their prescribed values. The smoothness and data-fitting constraints are competing requirements upon the final $\dot{b}_{fb}$ profile; these requirements are balanced by the inverse solution procedure using a tradeoff parameter.

The upstream (western) edge of our study area is more than 200 km from Ridge B, which is an ice-flow divide (*Parrenin et al.* (2004)). Consequently, all the ice in the Lake Vostok region is undergoing flank flow and the relatively shallow particle paths that we are modeling all have similar near-linear trajectories. Particle paths that begin at the upstream edge of our study area reach the layer depths only after traversing one third to one half of the length of the flowband. The portion of the layer that is not intersected by particle paths beginning within our study area therefore has no influence on the inferred accumulation-rate pattern. This flow regime destabilizes the inverse-solution procedure from one iteration to the next and can result in spuriously large changes in accumulation rate. Such behavior is non-physical, so we truncate small non-zero singular values to stabilize the inverse-solution procedure, as described in Appendix A of *Waddington et al.* (2007). Although this approach decreases the ability of formal inverse methods to detect accumulation-rate changes at the upstream and downstream ends of the flowbands (as opposed to not truncating the singular values), it allows us to recover physically reasonable solutions.

4.3.4 Surface-Velocity and Accumulation-Rate Data

In addition to radar-layer depths, the inverse-solution procedure can be further constrained by surface velocities and accumulation rates along the flowbands averaged over the layers' ages. Modern surface-velocity data are only available for flowband 1 at Vostok station (2 $\mathrm{m\,a^{-1}}$; *Wendt et al.* (2006)). Long-term accumulation-rate data are sparse (Magand and others, 2007) and are available only for flowbands 1, 2 and 4 at the three locations shown in Figure 1a (2.2 $\mathrm{cm\,a^{-1}}$ at Vostok, 4.0 $\mathrm{cm\,a^{-1}}$ at B37, 3.5 $\mathrm{cm\,a^{-1}}$ at B78; *Lipenkov et al.* (1998)). All accumulation rates presented here and elsewhere in this paper are in ice-equivalent.

To constrain our steady-state flowband model using these data, it is necessary to estimate constant accumulation rates and ice-flow speeds averaged over the past 41 ka. However, *Parrenin et al.* (2004) found that the accumulation rates inferred from the Vostok ice core increased twofold going from the last glacial maximum 18 ka ago into the Holocene. We account for this change in accumulation rates by multiplying the accumulation-rate data for the two oldest layers (B and C) by a factor of 0.75. This factor is calculated as the sum of the fractions of the layer age spent in each period (Holocene or glacial) multiplied by the ratios of the accumulation rate during each period to the modern value ($\dot{b}_{modern} \approx \dot{b}_{Holocene} \approx 2\dot{b}_{glacial}$). To maintain a steady state, smaller accumulation rates require lower ice-flow speeds, and *Leonard et al.* (2004) also inferred 50–65% slower ice-velocities between 26–41 ka from the hinge points in the depths of layers A and C. We apply the same reduction fraction (50%) for the ice speed when applying the flowband model to layers B and C. We also assume an uncertainty of 20% in all of these data when attempting to match them using inverse methods.

4.4 Results

4.4.1 LLA-Inferred Accumulation-Rate Maps

Figure 4.2b shows $\dot{b}_{LLA}$ inferred from layer C (41-ka old). $\dot{b}_{LLA}$ values are generally higher in the western half of our study area, and there is a 2.5-$\mathrm{cm\,a^{-1}}$ difference between the lowest and highest values of $\dot{b}_{LLA}$ inferred from layer C. The lowest values are found 10–20 km

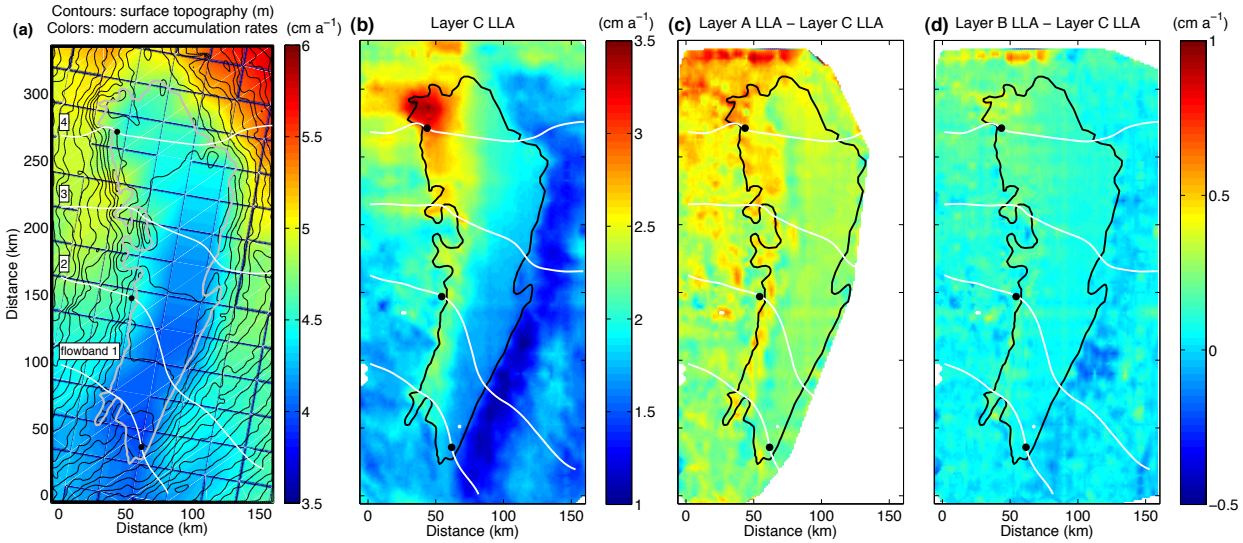

Figure 4.2: Surface topography (contour interval is 10 m) over a color map of modern ice-equivalent accumulation rates derived from satellite-microwave emission and field-based data (*Arthern et al.* (2006)). (b) LLA-inferred accumulation rates from layer C. (c) Difference between LLA-inferred accumulation rates from layer A and those for layer C. (d) Difference between LLA-inferred accumulation rates from layer B and those for layer C. The color bar to the right of (d) is for both (c) and (d).

downstream of the eastern/downstream shoreline of the lake. The highest values are focused in the northwestern corner of the lake and are consistent with the larger layer depths in that area (Figure 4.1c).

The differences between $\dot{b}_{LLA}$ values inferred from layers A and B in relation to layer C are shown in Figures 4.2c–d. The mean difference in $\dot{b}_{LLA}$ between layers A and C is 0.34 cm a^{-1}; between layers B and C it is 0.09 cm a^{-1}. The larger mean difference between layers A and C than between layers B and C is consistent with the larger difference between their ages. Forty-six percent of the age of layer A is spent in the Holocene, whereas smaller fractions of the ages of layers B and C are spent in the Holocene (24 and 29%, respectively). Layer A is therefore composed of particles that experienced more of the Holocene accumulation-rate history, which has higher values than the glacial period that dominates layers B and C. The apparent accumulation-rate high near the upstream shoreline observed by *Leonard et al.* (2004) is more prominent in layer A than it is in layers B or C. It

is displaced downstream from the lake shoreline because the equivalent trough in the layer depths has flowed downstream during the intervening 26.2 ka (the age of layer A). However, it is only displaced about 10 km from the lake shoreline, not ~ 50 km (26.2 ka $\times$ 2 m a^{-1}), suggesting that either $\bar{u}$ is lower there either now or in the past (*Leonard et al.* (2004)), or that the cause of the trough in layer depths does not originate at the lake shoreline. Because the difference in age between layers B and C (6 ka) is small relative to their ages ($< 20\%$) and both layers are older than the age of the Holocene–LGM accumulation-rate change, there is little difference between their $\dot{b}_{LLA}$ values (Figure 4.2c).

4.4.2 Suitability of the LLA (D values)

Figure 4.3 shows non-dimensional depth number D (equation 4.2) for our study area for the three different layers; Figure 4.4 shows interpolated values of D along the flowbands. The mean values of D for the study area are 0.28, 0.44 and 0.50, for layers A, B and C, respectively. D is generally larger for progressively deeper/older layers because D is proportional to L_{path}, which increases with layer age. The mean ratio of $L_{\dot{b}}/L_H$ varies between 4 and 12 for the different layers. The smaller value of either $L_{\dot{b}}$ or L_H will tend to dominate their contribution to D, so ice-thickness gradients in our study area have a greater influence on ice flow than accumulation-rate gradients.

Although we are using the three shallowest spatially extensive internal layers in the radar data, nearly all of our study area (96–98%) has D values greater than 0.1 that do not satisfy the $D \ll 1$ criterion, suggesting that the LLA may not accurately infer accumulation rates. Over the eastern (downstream) half of the lake, the LLA may be acceptable, but the large ice-thickness gradients near the lake shoreline suggest that the accumulation-rate pattern inferred with the LLA should be further investigated using a more sophisticated approach. We calculated D from values that were spatially averaged over ~ 60 km along-flow, which is less than L_{path} for any of the layers, but L_{path} is not well constrained for individual particle paths without using a flowband model. However, averaging over this distance produces a more meaningful value of D because it more accurately captures the length scales of changes that particles have experienced.

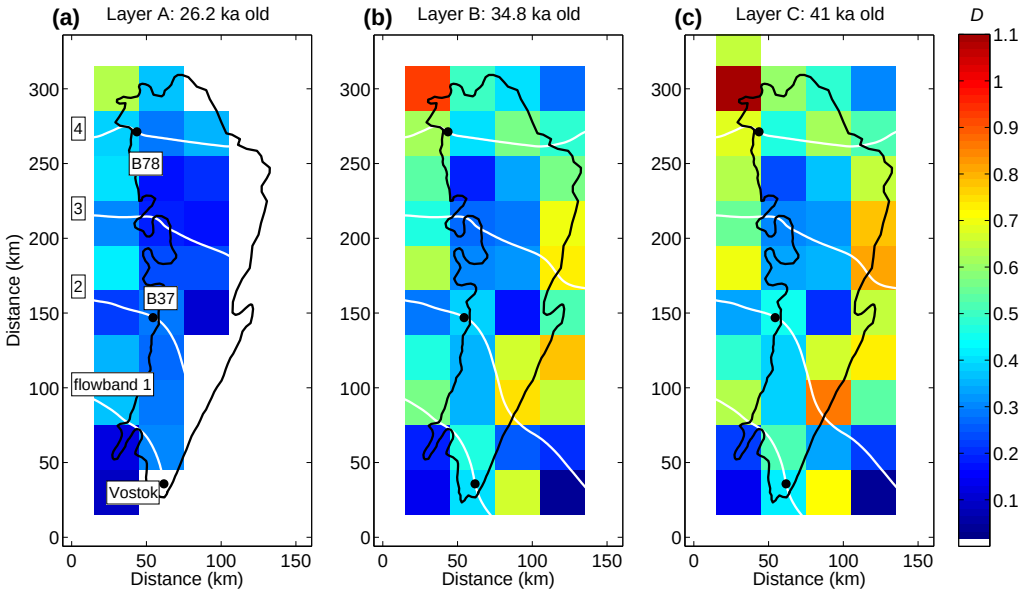

Figure 4.3: (a–c) Along-flow values of D for all three internal layers (4.2).

4.4.3 Accumulation-Rate Profiles Inferred Along Flowbands

Figure 4.4 shows the $\dot{b}_{LLA}$ profiles for all four flowbands, which were used to initialize the inverse solution procedure, and the final $\dot{b}_{fb}$ profiles inferred from that procedure. Figure 4.4 also shows the surface, layer and bed elevations, and D values along each flowband. For all four flowbands, accumulation rates are higher at their upstream end (0.2–1.0 cm a^{-1}) than downstream end, although the detailed structure of the accumulation-rate profiles varies substantially between each flowband. They also decrease smoothly across the lake, with a typical gradient of ~ -0.01 cm a^{-1} km^{-1}. Layers B and C are close in age (5 ka) relative to the age of layer C (12% of 41 ka), and both their $\dot{b}_{LLA}$ and $\dot{b}_{fb}$ profiles are similar (mean difference of 8% of layer Bs values for flowbands 1, 2, and 4). Despite being 9 and 15 ka younger than layers B or C, respectively, layer A's accumulation-rate patterns are often similar to those inferred from the older layers. Accumulation rates along the flowband that intersects Vostok station (1) were twice as high during the Holocene as during the glacial period (*Parrenin et al.* (2004)), which is consistent with the difference in magnitude between $\dot{b}_{LLA}$ and $\dot{b}_{fb}$ inferred from layer A versus those profiles inferred from layers B and C. Based on these results, we argue that the spatial pattern of relative accumulation rate has changed in our study area over the last 41 ka, although the ability to resolve these changes is limited by the steady-state models that we used, and the changes are greater for some flowbands (e.g., flowband 4) than for others (e.g., flowband 1). We note that there is no initial expectation built into the flowband model that the accumulation-rate patterns over this period would be similar.

4.5 Discussion

4.5.1 Comparison Between b_{LLA} and b_{fb} Profiles

Our initial evaluation of the non-dimensional number D (Figure 4.3) suggested that the LLA could generally be inaccurate for our study area. The mean D values along each flowband range between 0.2 and 0.5, with larger values for deeper layers, and $\dot{b}_{fb}$ is generally lower than $\dot{b}_{LLA}$ where D is low along the flowband. The $\dot{b}_{LLA}$ and $\dot{b}_{fb}$ profiles often have different shapes, except for layer A for flowband 1, where they are nearly identical. These patterns

Figure 4.4: Along-flow characteristics of flowband 1 (a–c; top left), 2 (d–f; top right), 3 (g–i; bottom left) and 3 (j–l; bottom right). The vertical gray bands represent the portion of each flowband that overlies Lake Vostok. (a, d, g, j) Surface, layer and bed elevations along the flowbands. The black (blue) lines represent the elevations of the surface and bed (three internal layers) and their vertical scale is in black (blue) and shown on the left (right). The vertical scale for the internal layers has a smaller range to better show their structure. Blue dots along the deepest layer (C) represent the points at which the radar lines cross the flowband, which shows where the two-dimensional grid interpolation may have introduced spurious structure into the internal layer shapes. Black circles along the surface-elevation profile show the location of field data used to constrain the inverse solution procedure. (b, e, h, k) Smoothed D shown in logarithmic scale for all three layers (A: black, B: blue, C: red). (c, f, i, l) Ice-equivalent accumulation-rate profiles inferred with the LLA ($\dot{b}_{LLA}$; dashed) and with formal inverse methods and a flowband model ($\dot{b}_{fb}$; solid) using the three layers (A: black; B: blue; C: red). The horizontal range for all panels is the length of the longest flowband (2).

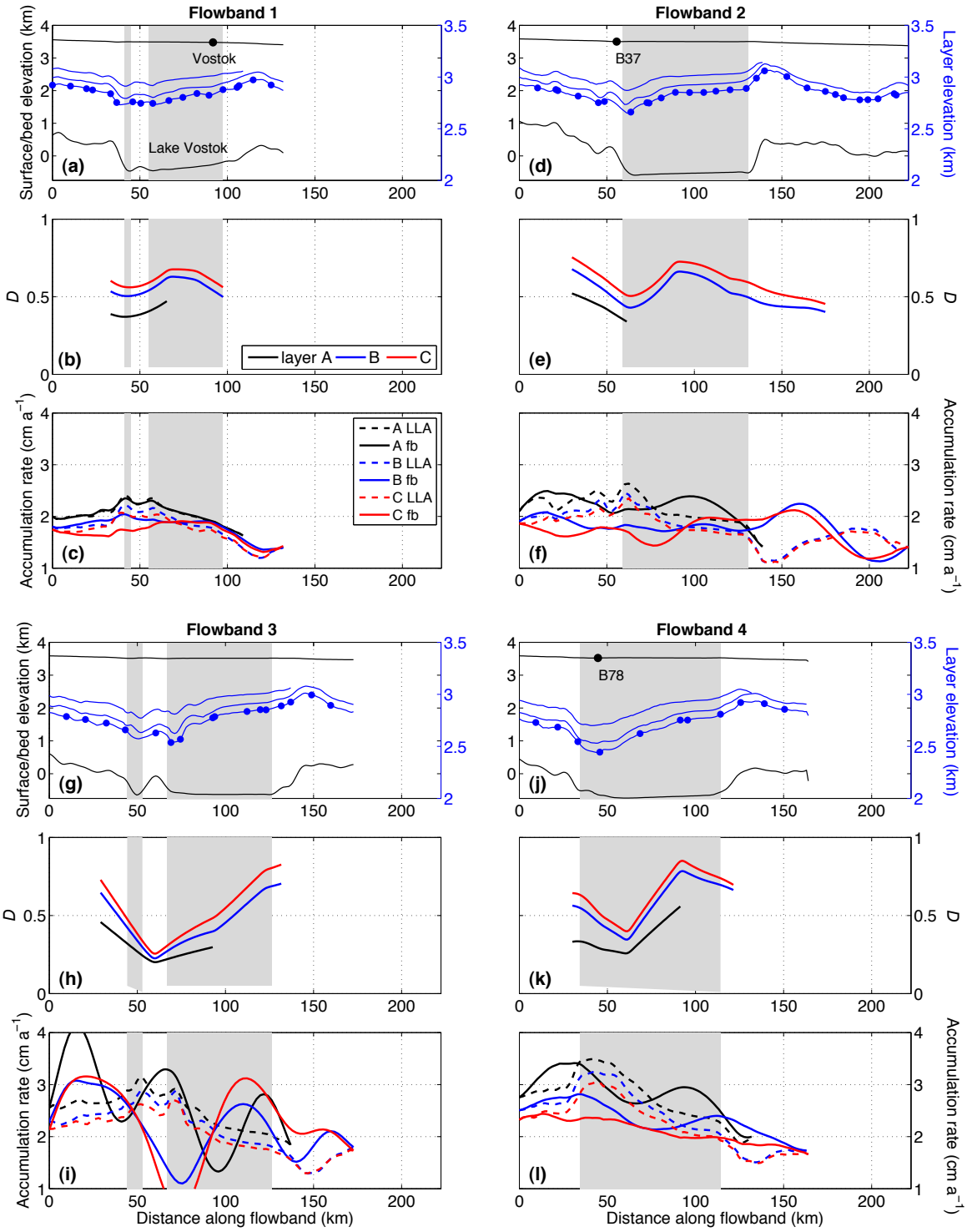
Flowband 1
Flowband 2
Flowband 3
Flowband 4
Surface/bed elevation (km)
Layer elevation (km)
Vostok
Lake Vostok
B37
B78
(a)
(b)
(c)
(d)
(e)
(f)
(g)
(h)
(i)
(j)
(k)
(l)
D
layer A B C
A LLA
A fb
B LLA
B fb
C LLA
C fb
Accumulation rate (cm a^{-1})
Distance along flowband (km)

suggest that our $D \ll 1$ criterion is sufficient for the suitability of the LLA but that it is not always necessary.

Structures in the $\dot{b}_{LLA}$ profiles are often translated further downstream than the $\dot{b}_{fb}$ profiles for progressively deeper layers, e.g., the upstream accumulation-rate high in flowband 4. This pattern is expected, as the inverse solution procedure should correctly assign these structures to their upstream origin on the surface, i.e., show less erroneous downstream translation of the structures in the accumulation-rate profiles. Flowband 1 has a relatively smooth $\dot{b}_{fb}$ profile and generally lower values than the other flowbands. The accumulation-rate high at the upstream shoreline visible in the $\dot{b}_{LLA}$ profile is less prominent in the $\dot{b}_{fb}$ profile. Flowband 2 has larger differences between $\dot{b}_{LLA}$ and $\dot{b}_{fb}$, and those differences are consistent for all layers. For example, there is no significant accumulation-rate high along the upstream shoreline in $\dot{b}_{fb}$, and $\dot{b}_{fb}$ is also higher over the lake. Upstream of the lake, $\dot{b}_{fb}$ is consistently lower than $\dot{b}_{LLA}$, whereas downstream of the lake the opposite is true. Flowband 2 is the longest of the four flowbands and it extends further downstream of the lake than any of the other flowbands, which may explain why it captures a larger difference between $\dot{b}_{LLA}$ and $\dot{b}_{fb}$ downstream of the lake. Flowband 4 is similar to flowband 1 in that it has a smoother decrease in both $\dot{b}_{LLA}$ and $\dot{b}_{fb}$ over the lake. It has a larger difference between $\dot{b}_{LLA}$ for layers B and C than for the other flowbands, and the same is true for $\dot{b}_{fb}$. The $\dot{b}_{fb}$ profile for layer C in flowband 4 deviates from the other profiles at the upstream and downstream ends the lake. There, $\dot{b}_{fb}$ is about 20% higher for layer C than would be expected based on the $\dot{b}_{fb}$ profiles of layers A and B. This difference suggests either a change in accumulation rates there between 35 and 41 ka ago or that the flowband model has difficulty reproducing layer C.

Flowband 3 shows large differences between $\dot{b}_{LLA}$ and $\dot{b}_{fb}$ that are not consistent between the three layers. These $\dot{b}_{fb}$ profiles are also very smooth and have no structures in common with the $\dot{b}_{LLA}$ profiles. Although it is able to converge to a solution, we suspect that the inverse solution procedure has failed to accurately model flowband 3 because of the unusual $\dot{b}_{fb}$ profiles and two additional reasons. First, flowband 3 is not constrained by any surface-velocity or accumulation-rate data, thus it is the least constrained of all the flowbands we used. Second, the flowband model likely does not adequately represent the more complicated

ice dynamics along flowband 3, which crosses over a shallow embayment before crossing the main body of Lake Vostok. Flowband 1 also crosses over a shallow embayment, but it is better constrained by other data. The inverse solution procedure cannot resolve features whose wavelength is close to L_{path}, i.e., such features are in its nullspace, which may cause the features in flowband 3's $\dot{b}_{fb}$ profiles.

For all three layers along flowbands 1, 2 and 4, the mean differences between $\dot{b}_{fb}$ and $\dot{b}_{LLA}$ are 5, 16 and 12% of $\dot{b}_{fb}$, respectively. The differences between $\dot{b}_{fb}$ and $\dot{b}_{LLA}$ are greater along the shoreline and away from the lake, and are generally larger for deeper layers. These small relative differences, along with the above comparisons of the $\dot{b}_{LLA}$ and $\dot{b}_{fb}$ profiles, suggest that the $\dot{b}_{LLA}$ map is an acceptable proxy for the real accumulation-rate map, particularly over the northern and southern ends of the lake, and less so in its middle. If numerous along-flow radar profiles are not available for a region of an ice sheet (as is generally the case), then the LLA is the best way to predict the regional accumulation-rate pattern from radar layers. However, we have not investigated some features of this $\dot{b}_{LLA}$ map, such as the accumulation-rate high in the northwestern corner of the lake (Figure 4.2), and we note that features of the $\dot{b}_{LLA}$ map on spatial scales smaller than the radar-line spacing are less reliable.

The $\dot{b}_{fb}$ profiles are inherently smoother because the inverse solution procedure imposes a smoothness constraint upon $\dot{b}_{fb}$. The real accumulation-rate pattern may have more structure at shorter wavelengths than can be inferred from the layer, but $\dot{b}_{fb}$ more accurately represents the particles' strain-rate histories along their paths than $\dot{b}_{LLA}$. From the surface to a deep layer, particles have traveled a horizontal distance at least an order of magnitude greater than their depth, and they have likely traversed significant strain-rate gradients. Both the real ice sheet and the particle paths calculated by the flowband model integrate these upstream gradients, so it is difficult to discern the effect of small-scale spatial changes in accumulation rate on deep layers by any method that uses a deep layer.

4.5.2 Comparison With Previous Studies of Lake Vostok Accumulation Rates

Arthern et al. (2006) presented a 25-km-resolution map of modern accumulation rates across

Antarctica, inferred from surface-measured accumulation-rate data and microwave emission recorded by satellites (Figure 4.2a). It shows a broad low in accumulation rates (about 4 $\mathrm{cm\,a^{-1}}$) over the southern half of the lake and higher values (more than 5 $\mathrm{cm\,a^{-1}}$) northeast of the lake. It also shows lower accumulation rates directly over the lake, which may be an artifact due to lower decimeter-scale surface roughness over the lake. Field measurements from *Dahe et al.* (1994) are in better agreement with our $\dot{b}_{LLA}$ map for layer A than the map of *Arthern et al.* (2006). Although the absolute accumulation-rate values differ between Arthern and others' map and ours, there is a similar pattern of increasing values to the north in our study area. However, Arthern and others' map does not resolve the large accumulation-rate high in the northwestern corner of the lake that we infer from the internal layers (Figure 4.2). It also does not resolve the $\dot{b}_{LLA}$ high along the upstream shoreline because of its coarser resolution.

Siegert (2003) inferred accumulation rates using radar-layer depths along a radar flight line that crossed over Ridge B and Vostok station and that is close to our flowband 1. He included a layer of a similar age (46 ka) to the oldest layer in this study (layer C: 41 ka). Our work improves upon that study because *Siegert* (2003) used only the LLA for layers of ages similar to or older than those used in this study, and because our flowband 1 more accurately follows the ice flow. The values of D shown in Figures 4.3c and 4.4b suggest that the LLA is generally not suitable for flowband 1, but the small relative difference between $\dot{b}_{LLA}$ and $\dot{b}_{fb}$ for flowband 1 (5%) suggests that the LLA is acceptable. The change in accumulation rate across Lake Vostok that *Siegert* (2003) found using the 46-ka-old layer is close to that which we infer using layer C (less than 0.5 $\mathrm{cm\,a^{-1}}$; Figure 4.4c). Our results and those of *Siegert* (2003) and *Vieli et al.* (2004) infer higher accumulation rates along this flowband upstream from the lake's western edge (Figure 4.4c)

Leonard et al. (2004) identified a stationary accumulation-rate high along the upstream shoreline of Lake Vostok that is likely due to the relatively large changes in surface slopes there. Higher accumulation rates have also been measured there using 1-m snow pits (*Dahe et al.* (1994)). Accumulation rates are often higher slightly downstream of steep surface slopes because katabatic winds are stronger (weaker) on steeper (shallower) slopes, so snow will be transported and then accumulate slightly downstream of the slope inflection points

(*Vaughan et al.* (1999); *King et al.* (2004)). Our $\dot{b}_{fb}$ profiles do not show higher values near the upstream shoreline, but the expected accumulation-rate high near there may not be resolvable using the flowband model because the localized high may occur over a spatial scale too short to be resolvable with our smoothness condition on $\dot{b}_{fb}$. These results suggest that ice-flow changes due to floatation over Lake Vostok, as well as accumulation rate along the upstream shoreline, cause the observed trough in the layer depths near the western shoreline from which an accumulation-rate high was inferred.

4.5.3 Uncertainty in b_{fb} and Improvements to the Flowband Model and Inverse Solution Procedure

Figure 4.4 shows that uncertainties in $\dot{b}_{fb}$ can be large ($> 50\%$) given limited data to constrain them, as was the case for flowband 3. A problem that affects all flowbands is the limited information on the upstream surface and bed topographies. Additional radar data that both follow flowlines and survey the area upstream of Lake Vostok to the ice divide at Ridge B would be valuable for constraining the inverse solution procedure. More field-measured surface-velocity and accumulation-rate data would provide further constraints (section 4.3.4). The flow field around the perimeter of Lake Vostok is poorly constrained due to the low surface-slope gradients and few internal structures that can be tracked (*Tikku et al.* (2004)). Additional layer picking may resolve this issue. If we had further confidence in the flow field, then we could model a spatially denser set of flowbands and interpolate the differences between $\dot{b}_{LLA}$ and $\dot{b}_{fb}$ along those flowbands across the entire study area to produce a more accurate accumulation-rate map.

There are several simplifications in our flowband model that could be improved upon. Our one-dimensional temperature model is unsophisticated relative to the temperature calculations in many existing thermomechanical ice-flow models (e.g., *Pattyn et al.* (2004)). Our modeled temperature profile is consistently higher than the observed temperature profile (mean difference of 2.9 K) at Vostok station (V.Y. Lipenkov, pers. comm., 2006). However, this difference is largest in the 1500–2500-m depth range, which is greater than the depth of the deepest layer used here, and ice temperatures determine only the normalized

horizontal velocity field (its shape functions) and not its magnitudes. Our simplified temperature model is therefore acceptable for the purposes of the flowband model. A flowband model that includes longitudinal strain-rate gradients and a coupled temperature model (e.g., *Price et al.* (2007)) would better represent the ice dynamics over the lake, although initial and boundary conditions would be more difficult to set. Finally, an alternate inverse solution procedure using Monte Carlo methods (e.g., *Steen-Larsen et al.* (2007)), could better evaluate the sensitivity of the modeled accumulation rates to our initial guesses of the model parameters.

We used a steady-state flowband model to infer accumulation rates, although previous modeling work using radar layers suggest that ice flow was non-steady in the Lake Vostok region during the last 41 ka (*Vieli et al.* (2004); *Salamatin et al.* (in press)). Surface elevations, ice velocities, and the location of the Vostok flowline may have changed in the last 41 ka, but here we have implicitly assumed that such changes did not significantly affect the inferred accumulation rates. If the flowline that passes through Vostok has not changed in the last 41 ka, then our steady-state model should still recover the correct mean accumulation rate during this period. *Salamatin et al.* (in press) tuned a non-steady thermomechanical flowband model along the Vostok flowline that produced layers that matched well with the observed layers. They did not use formal inverse methods to match their data, but their results and ours suggest that future accumulation-rate studies should combine the increased accuracy of non-steady flowband models with the computational efficiency of formal inverse methods.

4.6 Conclusions

We have presented an accumulation-rate map for the Lake Vostok region inferred from internal-layer depths observed in radar data. By comparing this map to results from a formal inverse method that incorporates a flowband model, we find that the regional accumulation-rate pattern inferred from internal layers using the LLA is a reasonable estimate of accumulation rates in this study area. In terms of its spatial resolution and evaluation of its uncertainties, our regional map is a significant improvement upon previous studies of accumulation rates in this region. It reproduces some features of the spatial pattern that have

been previously observed, including a broad low in the southern half of the lake and a high near the lake's upstream shoreline. We also infer a broad accumulation-rate high in the northwestern corner of the lake that has not previously been identified. For at least two of our four modeled flowbands, this pattern has changed significantly (up to 50%) over the past 41 ka, possibly during the transition from the last glacial period to the Holocene.

Airborne radar surveys are often designed as orthogonal grids that often do not follow ice flowlines. Without extensive efforts to reconstruct layer depths along flowlines from sparsely crossing radar profiles, the LLA is a reasonable method for inferring the regional accumulation-rate pattern. However, our results show that the LLA occasionally predicts questionable abrupt accumulation-rate variations in response to upstream ice-thickness gradients, such as along the shoreline of Lake Vostok. The steady-state flowband procedure accounts for these gradients at the cost of a smoother accumulation-rate profile that cannot capture some short-scale anomalies, such as the possible high along the upstream shoreline. Because the $\dot{b}_{flb}$ profiles might have differed substantially from the $\dot{b}_{LLA}$ profiles (e.g., *Waddington et al.* (2007)), we emphasize the need to apply formal inverse methods for inferring past accumulation rates from deep layers to improve upon accumulation-rate patterns inferred from simpler methods.

Chapter 5

MODELING THE SPATIAL VARIATION OF ICE-SHEET RADAR ATTENUATION

This chapter is a draft of a manuscript in preparation. My co-authors are Kenichi Matsuoka, Ed Waddington, and Dale Winebrenner, who all guided my work and edited the manuscript.

5.1 Summary

Knowledge of the spatial variation of ice-sheet attenuation rates is poor but is needed to accurately infer englacial and basal properties from ice-penetrating radar data. Radar-attenuation rates depend on the spatial variation of temperature and soluble impurity concentrations (in Antarctica, primarily acid and sea-salt chloride). Because temperature and impurity-concentration data are measured only at the surface or in ice cores or boreholes, models of their spatial variation are required to predict attenuation rates in ice sheets. Here we evaluate several methods for modeling the spatial variation of attenuation rates, using an example of their application along a flowline that crosses through the Vostok ice core in East Antarctica. We use radar-layer depths and temperature and velocity outputs from a thermomechanical ice-sheet model to extend impurity-concentration and borehole-temperature data from Vostok along the flowline. The simplest possible model is a uniform, depth-averaged attenuation rate everywhere along the flowline, the next model uses spatially varying temperatures and uniform impurity concentrations, and subsequent models use radar-layer depths the ice-sheet-model outputs to also estimate the spatial variation of impurity concentrations, along with spatially varying temperatures. We find that models that include the spatial variation of temperature can have large differences (> 10 dB) in roundtrip attenuation, as compared to models that simply use a uniform attenuation-rate field. Models with progressive improvements for modeling the spatial variation of impurity concentrations introduce only small (< 3 dB) changes in the roundtrip attenuation. This

work shows that an attenuation-rate model tied to an ice-core site can be satisfactorily extended spatially using available radar-layer depths and a temperature model.

5.2 Introduction

The current spatial distribution of ice-sheet bed conditions is poorly known and has been identified as a major source of uncertainty in predictive ice-sheet models (*Alley et al.* (2005); *Bell* (2008)). Ice-penetrating radar surveys are one of the primary geophysical methods for the investigation of ice-sheet bed conditions. The bed-echo intensity recorded by radar depends on its system parameters, on englacial losses, and on the bed reflectivity (e.g., *Peters et al.* (2005)). Englacial losses include dielectric attenuation, geometric spreading, and scattering. The bed reflectivity depends on the dielectric contrast produced at the ice–bed interface and the bed roughness. Bed-reflectivity values inferred from radar surveys are diagnostic of frozen or thawed beds, i.e., the bed condition.

Radar-system parameters are generally assumed to be constant, geometric-spreading loss is easily calculated, and scattering loss is assumed to be negligible in crevasse-free regions when using decameter-wavelength radars. The primary unknown in the calculation of bed reflectivity is therefore the total attenuation within the ice and its spatial variation. Radar attenuation in ice sheets primarily depends on both temperature and impurity concentrations, and depth-averaged attenuation rates can vary between about 10 and 30 $\mathrm{dB\,km^{-1}}$ (Chapter 2.6), yet the reflectivity difference between a dry bed and a wet bed is only about 10 dB (*Peters et al.* (2005)). A better understanding of the spatial variation of attenuation rates is therefore critical for accurate inference of bed conditions from radar data.

Bentley et al. (1998) and *Peters et al.* (2005) used uniform radar-derived values of the attenuation rate to infer bed-reflectivity variations over large areas ($> 10^4$ $\mathrm{km^2}$) of the Siple Coast ice streams, where ice temperatures vary significantly (e.g., *Engelhardt* (2004); *Joughin et al.* (2004)). For their investigation of Antarctic subglacial lakes, *Carter et al.* (2007) improved upon that method by scaling the depth-averaged attenuation rate using an impurity- and temperature-dependent attenuation-rate model and a one-dimensional temperature model. Here, using an example flowline that passes through the Vostok ice core in East Antarctica (Figure 5.1, we evaluate those methods and develop new methods

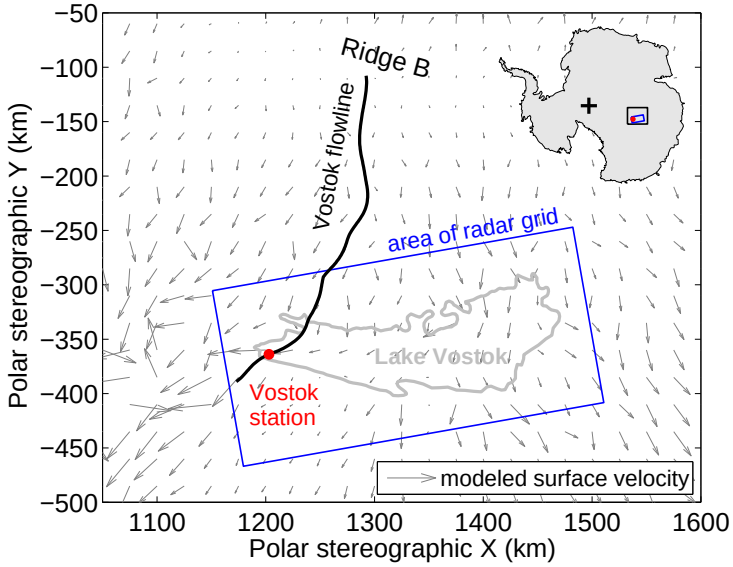

Figure 5.1: Modeled surface velocities (~ 2 m a^{-1} at Vostok) for the Lake Vostok region (section 5.3.3) and location of the flowline that crosses through the Vostok ice-core site. Only a portion of the Vostok flowline is shown. Outside of the SOAR grid, the flowline is determined using BEDMAP surface-elevation data (section 5.3.3). The blue solid line outlines the region where most of the SOAR radar data were collected (*Studinger et al.* (2003)).

for predicting the spatial variation of radar attenuation. We begin with the simplest possible model (a uniform value of attenuation rate) and improve upon it using the modeled spatial variation of temperature along the flowline, radar-layer depths, and modeled ice velocities.

5.3 Attenuation-Rate Models

5.3.1 Ice Conductivity and Radar Attenuation

Radar attenuation rates are proportional to the conductivity of the ice column through which the radio waves travel. Ice conductivity non-linearly depends on its temperature and linearly depends on its molar concentrations of two primary impurities (acid and sea-salt chloride). The depth-averaged attenuation rate N_a in dB km^{-1} is linearly proportional to the conductivity σ in μS m^{-1} integrated over the ice column (Chapter 2):

$$N_a = 0.919\sigma. \tag{5.1}$$

Table 5.1: Main features of the attenuation-rate models that we tested.

Model	Ice temperatures	Impurity concentrations
A (ref.)	Uniform	Uniform
B	From 3-D ice-sheet model	Uniform
C1	From 3-D ice-sheet model	Rescaled using observed layer depths
C2	From 3-D ice-sheet model	Rescaled using observed and modeled layer depths
D	From 3-D ice-sheet model	Particle paths tracked to surface and flux-corrected

5.3.2 Models of the Spatial Variation of Radar Attenuation

To extend a depth-averaged attenuation-rate value beyond an ice-core site, we must estimate the spatial variation of impurity concentrations and temperature, i.e., the parameters upon which attenuation rates depend. Below we describe the five attenuation-rate models considered in this study. Their primary features are also summarized in Table 5.1. These models either include or exclude spatial variations in temperature and impurity concentrations, and they are primarily distinguished by how they treat spatial variations in impurity concentrations. They consist of attenuation-rate values at each point in a two-dimensional gridded model domain oriented along the flowline. Although we consider this problem in only two dimensions, partly because they are most easily described in two dimensions, they are equally applicable to three-dimensional problems.

The first model (A) assumes a uniform value of the depth-averaged attenuation rate over the study area. A uniform attenuation-rate value is equivalent to assuming that both impurity concentrations and temperature are also uniform, i.e., they do not vary with depth or along-flow. It is also considered the reference model, because it is the simplest possible model and one that has often been used in the study of bed reflectivities (e.g., *Bentley et al.* (1998); *Peters et al.* (2005)). However, ice-temperature models in dynamic regions of an ice sheet suggest that this model is inadequate on a regional scale (e.g., the Siple Coast of West Antarctica; *Engelhardt* (2004); *Joughin et al.* (2004)). This model may be valid only in slow-moving, inland regions of an ice sheet, where ice temperatures are expected to change gradually, such as the Lake Vostok region. Large ice-thickness or bed-condition

changes likely further restrict the portions of an ice sheet where this model is valid.

The second model (B) again assumes uniform impurity concentrations, but does not assume uniform temperatures. It uses the modeled temperatures from the thermomechanical model described in section 5.3.3, and this change from model A is preserved in all subsequent models (C1, C2 and D). This attenuation-rate model is similar to that used by *Carter et al.* (2007), except that they used a one-dimensional temperature model to scale attenuation rates and a conductivity model from *Corr et al.* (1993) that was not based on a synthesis of measured dielectric properties.

Before we describe the final three models (C1, C2, and D), which no longer assume uniform impurity concentrations, we first consider the relative importance of the two mechanisms by which impurities are incorporated into ice from the surface: wet and dry deposition. A simple linear model relating the atmospheric flux f of impurity X to its surface ice concentration $[\mathrm{X}]_{surf}$ and ice-equivalent accumulation rate $\dot{b}$ at the time of deposition is (e.g., *Kreutz et al.* (2000)):

$$f_X = s\dot{b}[\mathrm{X}]_{air} + d[\mathrm{X}]_{air}, \tag{5.2}$$

where $[\mathrm{X}]_{air}$ is the concentration of impurity X in air, s is the dimensionless scavenging ratio, and d is the dry deposition velocity. The first term represents wet deposition of impurities, i.e., during snowfall, and the second term represents dry deposition, i.e., aerosol fall-out. The relative importance of these two mechanisms undoubtedly varies across an ice sheet, as accumulation rates vary by at least two orders of magnitude (*Arthern et al.* (2006)), and high acid concentrations at high surface elevations at Dome Fuji, East Antarctica, (*Fujita et al.* (2002a)) suggest increased stratospheric input and hence higher dry deposition rates there. Furthermore, s and d may also be impurity-dependent, and the physical accuracy of this empirical model is not yet known (*Alley et al.* (1995); *Kreutz et al.* (2000)). The spatially varying contribution to the impurity flux from these mechanisms could therefore affect the impurity-concentration field along an ice flowline.

The third model (C1) uses observed radar-layer depths to rescale the depth profile of impurity concentrations from the Vostok ice core along the flowline. The depth interval between any two layers may vary across the study area because the accumulation-rate and

ice-flow histories of the particles that produce these layers vary over time (*Waddington et al.* (2007)). We assume that the portions of the impurity-concentration profiles $[\mathrm{X}]_{ice}(x, z)$ that lie between any two layer depths $d_i(x, z)$ (including the surface and the bed) do not change across the study area from the values at the Vostok ice-core site (x_{core}):

$$[\mathrm{X}]_{ice}\left(x, d_i(x) : d_{i+1}(x)\right) = [\mathrm{X}]_{ice}\left(x_{core}, d_i(x_{core}) : d_{i+1}(x_{core})\right). \tag{5.3}$$

We then rescale (aka "rubber-band") the impurity-concentration profiles using the layer-depth variations. For each point along the flowline, the portion of the impurity-concentration profile between two layers is re-interpolated onto the depth-normalized grid. This rubber-banding process is illustrated for the Vostok flowline in Figure 5.3. Model C1 uses only observed radar layers.

For model C1 (and C2), we ignore any spatial or temporal variations in accumulation rates or atmospheric impurity concentrations that could affect the impurity-flux history along the flowline (equation 2). However, accumulation rates are known to vary along the flowline (Chapter 4) and it is extremely unlikely that the atmospheric concentrations of H^+ or ss Cl^- ions have remained uniform and constant along the flowline over the last 420 ka (the age of the oldest dated ice in the ice core). This model also assumes that the radar layers are isochronous, which may not be valid if the layer is due to a fabric contrast (e.g., *Eisen et al.* (2007)). Finally, it also ignores convergence (divergence) of the flowband whose center is the Vostok flowline, which would increase (decrease) impurity concentrations as ice contracts (expands) transverse to ice flow. We therefore test this model while recognizing its implicit assumption that the rescaled Vostok impurity-concentration profile is valid for the entire flowline.

The fourth model (C2) is similar to model C1 in that it uses observed radar layers to rescale the impurity-concentration profiles, but model C2 also uses modeled layers to rescale the impurity-concentration profiles. It is common to observe few or no radar layers in the bottom one-third of an ice sheet because total englacial signal loss (attenuation, geometric spreading, and scattering) increases with depth and because ice-flow-induced shear strain increases with proximity to the bed and distorts layers that might otherwise be clearly visible (e.g., *Matsuoka et al.* (2003)). Because attenuation rates increase non-linearly with

temperature and are much larger closer to the bed (Figure 5.6a), this problem motivates the use of modeled layers derived from ice-flow models to help further constrain impurity concentrations in this important section of an ice sheet. To address this limitation of model C1, we generate modeled layers by integrating the modeled velocities for the study area along particle paths (e.g., *Waddington et al.* (2007)). These modeled layers are included in model C2.

The fifth and final model (D) does not use observed or modeled layers to rescale the impurity-concentration profiles. Instead, model D uses the modeled velocities to reverse-track particle paths from each grid point to the surface and then determine the impurity concentration based on the inferred accumulation-rate and impurity-concentration histories. This reverse-particle-path tracking is illustrated in Figure 5.4. The key benefit of this model is that it more accurately represents how impurities are deposited in an ice sheet. Rescaling the depth profile of impurity concentrations from the ice core using layer depths (models C1 and C2) does not consider whether the impurity-concentration profile between any two layers has changed because of accumulation-rate or atmospheric-concentration variations. A potential disadvantage of model D is its increased reliance on the ice-sheet model outputs that are difficult to verify.

Because past values of $[\mathrm{X}]_{air}$ are poorly known, ice-core-measured impurity concentrations ($[\mathrm{X}]_{ice}$) and inferred past accumulation rates are generally used as a proxy for the past impurity flux to the ice-sheet surface:

$$f_X(t) = \dot{b}(x,t)[\mathrm{X}]_{surf}(x,t), \tag{5.4}$$

where x is the along-flow horizontal spatial coordinate, t is time, the two molar impurity concentrations [X] are acid ($[\mathrm{H}^+]$) and sea-salt chloride ($[\mathrm{ss\,Cl}^-]$), and $[\mathrm{X}]_{surf}$ is assumed to be equal to $[\mathrm{X}]_{ice}$.. We assume that $f_X(t)$ is uniform along the flowline. We do not distinguish between dry and wet deposition, which requires additional knowledge of the dry deposition rate and the scavenging ratio (e.g., *Kreutz et al.* (2000)), and may vary depending on the chemical species. The impurity-flux history $f_X(t)$ of the study area is calculated using the depth profiles of ice-core impurity-concentration $[\mathrm{X}](x_{core}, z)$ (z is depth), the ice core's depth–age scale and the modeled accumulation-rate history at the ice-core site

$\dot{b}(x_{core}, t)$. We estimate $\dot{b}(x, t)$ by scaling the mean accumulation-rate map for the last 41 ka $\bar{\dot{b}}(x, 0 - -41\,\mathrm{ka})$ by $\dot{b}(x_{core}, t)$. Using $f_X(t)$, $\dot{b}(x, t)$ and (5.4), we calculate $[\mathrm{X}]_{surf}(x, t)$. Finally, by determining the surface origin and age of each point in the two-dimensional grid using particle paths from the reversed velocity field, we produce the two-dimensional impurity-concentration field $[\mathrm{X}](x, z)$.

5.3.3 Application to Vostok Flowline

Flowline-specific considerations

Here we describe the data used for the different attenuation-rate models along the Vostok flowline. For the two-dimensional flowline grid, the along-flow horizontal resolution is 1.5 km and the vertical resolution is depth-normalized. There are 50 evenly spaced vertical layers, with intervals varying between 57–79 m depending on the ice thickness, which varies between 2831–3961 m along the flowline.

At Vostok, the deepest observed layer is found at a depth of 2210 m at Vostok, which is 56% of the ice thickness there. The observed layers can therefore usefully rescale the impurity concentrations of only about half of the ice thickness across the study area, leaving the deeper half of model C1 unimproved relative to model B. We modeled 3 layers that are 200–400-ka old and are evenly spaced in age. This age range lies between the age of the oldest mapped layer (155 ka) and the age of the oldest ice above the basal layer at Vostok ($\sim$ 420 ka; *Parrenin et al.* (2004)).

For the mean impurity concentrations in meteoric ice in the Vostok ice core, the temperature dependence of the pure ice component of the attenuation model will dominate at temperatures above $-40°$C. This temperature occurs below 1700 m at Vostok, so the attenuation rate there is dominated by the pure ice component for more than 55% of the ice thickness. The attenuation contribution from impurities is still important in the upper half the ice sheet and influences the depth-averaged value of the attenuation rate, which is the quantity that we study here. To calculate depth-averaged attenuation rate from values of these two impurity concentrations and temperature, we use Vostok ice-core data, the conductivity model synthesized in Chapter 2 and adapted for use at Vostok in Chapter 3,

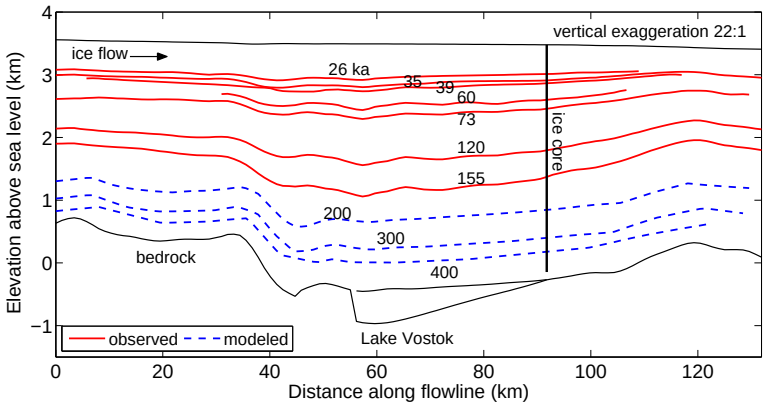

Figure 5.2: Cross-section of Vostok flowline showing its main features, radar-observed layers, (between 26-ka and 155-ka old), and modeled layers (200-, 300-, and 400-ka old).

and (5.1).

Radar data

For internal layers, we use the 60-MHz airborne ice-penetrating radar data collected over the Lake Vostok region in an approximately 150-km by 350-km grid by the U.S. Support Office for Aerogeophysical Research (SOAR) at the University of Texas Institute for Geophysics. *Blankenship et al.* (2001) described the system characteristics. This dataset was used to derive ice thickness and surface elevation along the flowline (*Studinger et al.* (2003)). *Tikku et al.* (2004) picked 7 internal layers in the radar data that were interpolated onto a 1.5-km grid. Here we interpolate their gridded layer depths along the Vostok flowline. All of these layers pass through the Vostok ice-core site (hereafter Vostok) and are dated using its most recent depth–age scale (*Parrenin et al.* (2004)), with ages ranging between 26.2 ka and 155 ka.

Ice-core data

We use ice-core chemistry (*Petit et al.* (1999), *de Angelis et al.* (2004)), borehole-temperature (*Tsyganova and Salamatin* (2004), *Lipenkov et al.* (2004), V.Y. Lipenkov, pers. comm., 2006) and ice-density data (*Lipenkov et al.* (1997)) from the 3623-m-deep Vostok ice core

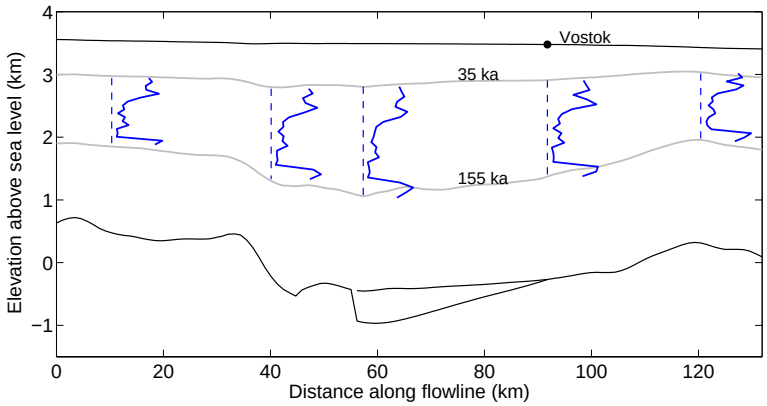

Figure 5.3: Cross-section of Vostok flowline illustrating the rubber-banding process with the portion of the [ss Cl^-] profile between the 35-ka and the 155-ka observed layers selected locations along the flowline.

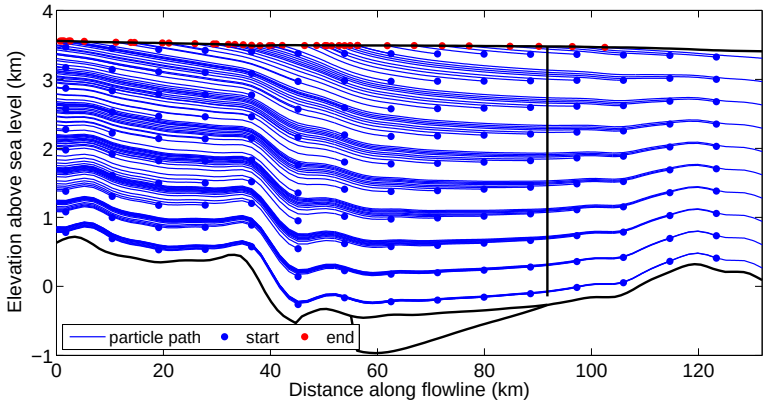

Figure 5.4: Modeled reversed particle paths from every fifth point in the two-dimensional, depth-normalized grid along the Vostok flowline.

to model attenuation rates there. We also use the modeled accumulation-rate history and depth–age scale inferred from the ice-core data (*Parrenin et al.* (2004)). The ice-core data used here are identical to those used in Chapter 3, to which we refer the reader for further details. The depth range of the ice-core chemistry data is 150–3623 m, so we assume that the ice chemistry above 150 m and below 3623 m (to the ice–lake interface at 3755 m) is uniform and is the same as that at 150 m and 3623 m, respectively.

Modeled temperatures and ice velocities

For ice temperatures and velocities along the Vostok flowline, we use outputs from a three-dimensional, coupled, thermomechanical ice-flow model with 5-km horizontal resolution over the entire Antarctic ice sheet and 7 vertical layers (*Matsuoka et al.* (in prep.)). To initialize the ice-flow model and extend our attenuation-rate model across our study area, we use the mean accumulation-rate map for the last 41 ka inferred from three radar-layer depths (Chapter 4). Temperatures and ice velocities were interpolated along the flowline, and horizontal velocities were projected into an along-flow and a transverse-to-flow component. Figure 5.5 shows these interpolated velocities and temperatures along the portion of the Vostok flowline that we focus on in this study. Upstream of the area of the SOAR grid, we used BEDMAP surface-elevation and ice-thickness data (*Lythe et al.* (2001)) to locate the flowline from surface-elevation gradients and to interpolate the temperature and ice-velocity model outputs onto an ice-thickness-normalized grid.

5.4 Results

Figure 5.6a shows the modeled one-way attenuation-rate profiles for the 5 different models at Vostok. The attenuation-rate profile modeled using all the ice-core data is also shown (Chapter 3). All modeled profiles predict a large increase in attenuation rate with increasing depth, due to higher temperatures closer to the bed. Short-scale variations are due to varying impurity concentrations. All models excepting D only depend ice-core and/or radar data, so at the ice-core site they present different averaged versions of the full ice-core-modeled attenuation-rate profile. Models C1 and C2 use observed and/or modeled layers to rescale the ice-core impurity-concentration profiles elsewhere along the flowline, but they do

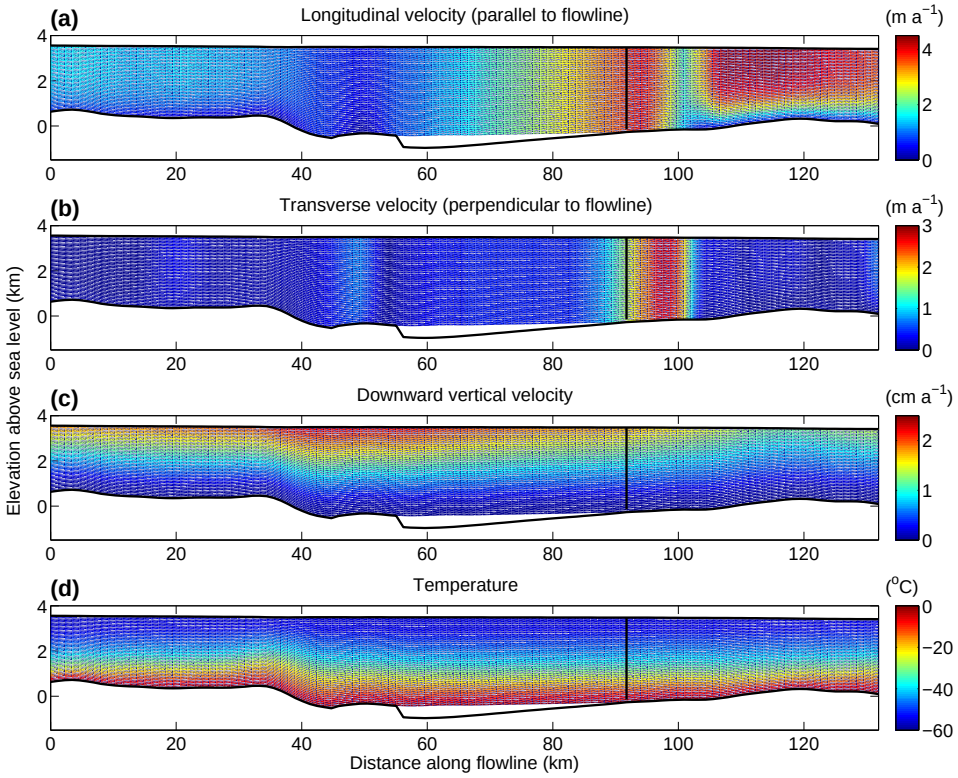

Figure 5.5: Modeled longitudinal (a), transverse (b), and vertical ice velocities (c) and temperatures (d) along the Vostok flowline.

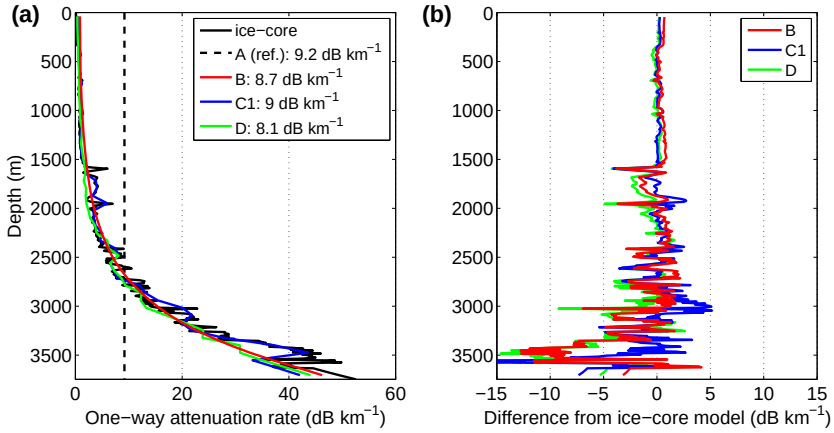

Figure 5.6: (a) One-way depth profiles of attenuation rate for the five attenuation-rate models (section 5.3) at Vostok. Equivalent depth-averaged values are shown in the legend. Models C1 and C2 are identical at Vostok, model C2 is not shown here. The ice-core-modeled attenuation-rate profile was originally shown in Chapter 3 (b) Difference between attenuation models B/C1/D and model A at the ice-core site. Because model C2 is not shown because of its similarity to model C2.

not alter the impurity-concentration profiles at the ice-core site. Hence, at the ice-core site they are simply a sub-sampled version of the ice-core-modeled profile and are not discernable from each other there. Model D uses modeled particle paths and accumulation rates upstream of the ice-core site, so its attenuation-rate profile at Vostok may not necessarily be similar to the ice-core-modeled profile. Its attenuation-rate profile matches that of the other models at shallower depths, but it is significantly lower between 3300 and 3500 m.

Figure 5.6b shows the difference in attenuation rate at Vostok between models B/C1/D and model A. All three models generally underestimate the attenuation rate at depths greater than 3000 m at Vostok, which leads to lower depth-averaged values. Models B and D are more than 10 dB km^{-1} lower than model A near 3500 m depth.

Figure 5.7 shows cross-sections of the attenuation-rate fields along the Vostok flowline for the five different attenuation-rate models (section 5.3). The along-flow depth-averaged attenuation rates and total attenuation to the bed for each model are also shown. It is clear from these cross-sections and the depth-averaged attenuation-rate profiles that the inclusion of spatially varying temperatures in the attenuation-rate models has the largest

effect upon the results. For models B, C1, C2 and D, all of which include spatially varying temperatures, the differences in the depth-averaged attenuation rate between those models and reference model A are much larger (up to 2 dB km^{-1}) than the differences between each other (< 0.5 dB km^{-1}).

The mean difference in depth-averaged attenuation rate between models B and C1 is 0.3 dB km^{-1}, and model C1 is consistently higher than model B. Values of the impurity concentrations greater than their depth-averaged values cause larger increases in attenuation rate at greater depths, because of the non-linear temperature dependence of attenuation rates and the higher temperatures closer to the bed. Impurity concentrations are often higher at greater depths than their depth-averaged values at Vostok, which explains the difference between models B and C1. Models C1 and C2 are negligibly different (mean difference of 0.1 dB km^{-1}, despite the inclusion of deep modeled layers in model C2. This result suggests that changes in impurity concentrations in deep ice at Vostok are sufficiently and accurately constrained by the depth of the deepest observed layer. Model D, which attempts to more accurately capture mechanism by which impurities are concentrated in falling snow, predicts lower attenuation rates than all the other models along most of the flowline, similar to its behavior at Vostok.

In terms of the roundtrip/total attenuation loss, the differences between model A and models B, C1, C2 are largest near the beginning (km 0–10) and end (km 110–125) of the flowline (Figure 5.8). There, these differences exceed 10 dB, which is the threshold for distinguishing dry beds from wet beds. Over Lake Vostok ($\sim$ km 55–90), the differences are smaller, ranging between 0 and 3 dB. The differences in total attenuation are not correlated with ice-thickness changes along the flowline. These results suggest that model A generally overestimates the total attenuation along the flowline, leading to an overestimate of the bed reflectivity.

5.5 Discussion

These results strongly suggest that the common assumption of a uniform depth-averaged attenuation rate (model A) is inadequate, even in relatively slow-moving ice (< 5 m a^{-1}). Errors in the roundtrip attenuation can exceed 10 dB, thus confounding the first-order goal

Figure 5.7: (a–e) Modeled one-way attenuation rates along the Vostok flowline for the five different attenuation-rate models considered in this study (section 5.3). Key features of the flowline are labeled in (a). In (c) and (d), for clarity only three observed layers are shown (Figure 5.2). The color scale is the same for all five cross-sections. (f) Equivalent along-flow depth-averaged attenuation rates and total round-trip attenuation to the bed for the five attenuation-rate models.

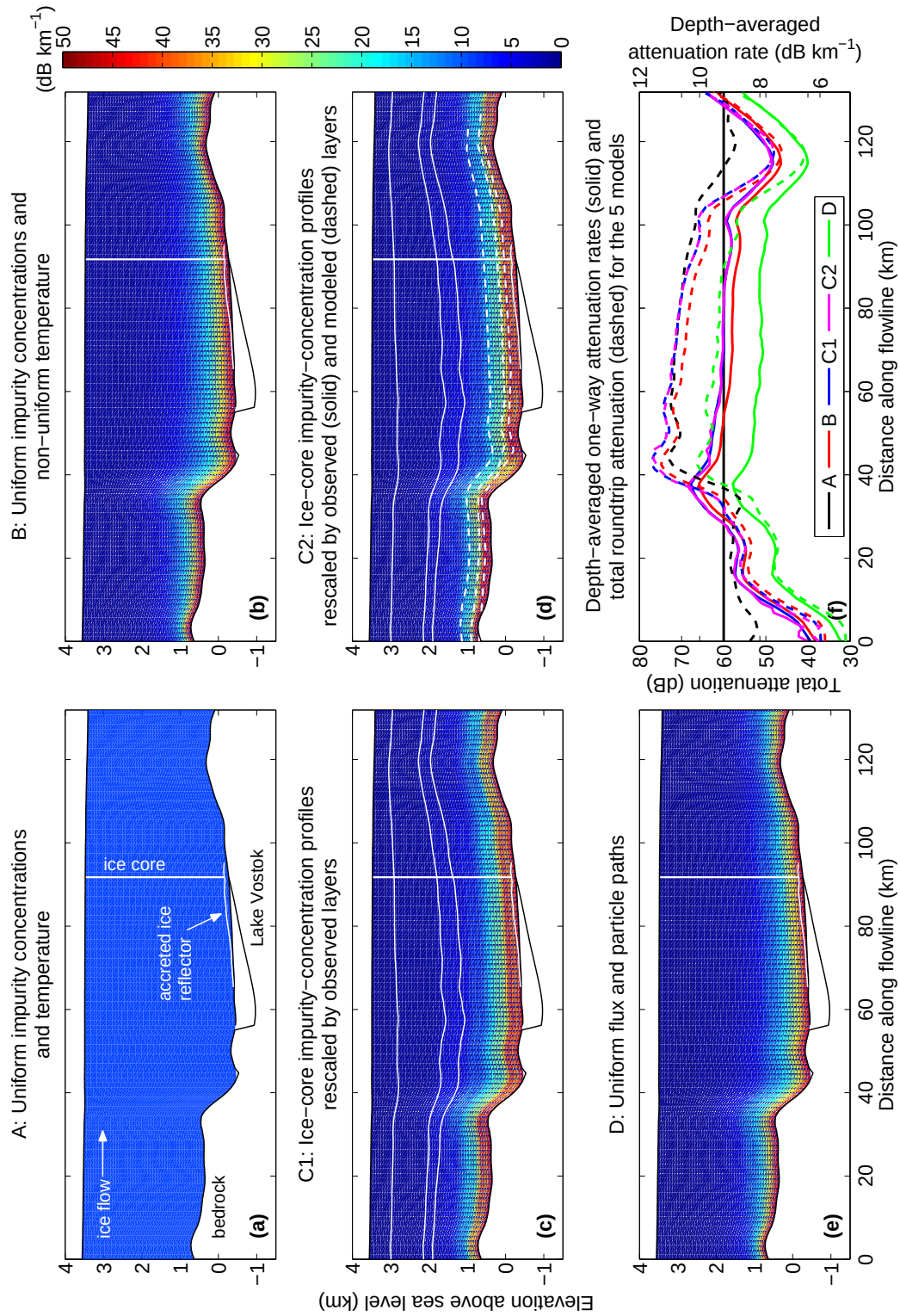
A: Uniform impurity concentrations and temperature
ice flow
ice core
accreted ice reflector
bedrock
Lake Vostok
(a)
B: Uniform impurity concentrations and non−uniform temperature
(dB km^{-1})
(b)
C1: Ice−core impurity−concentration profiles rescaled by observed layers
(c)
C2: Ice−core impurity−concentration profiles rescaled by observed (solid) and modeled (dashed) layers
(d)
D: Uniform flux and particle paths
(e)
Elevation above sea level (km)
Distance along flowline (km)
Depth−averaged one−way attenuation rates (solid) and total roundtrip attenuation (dashed) for the 5 models
Total attenuation (dB)
Depth−averaged attenuation rate (dB km^{-1})
A
B
C1
C2
D
(f)

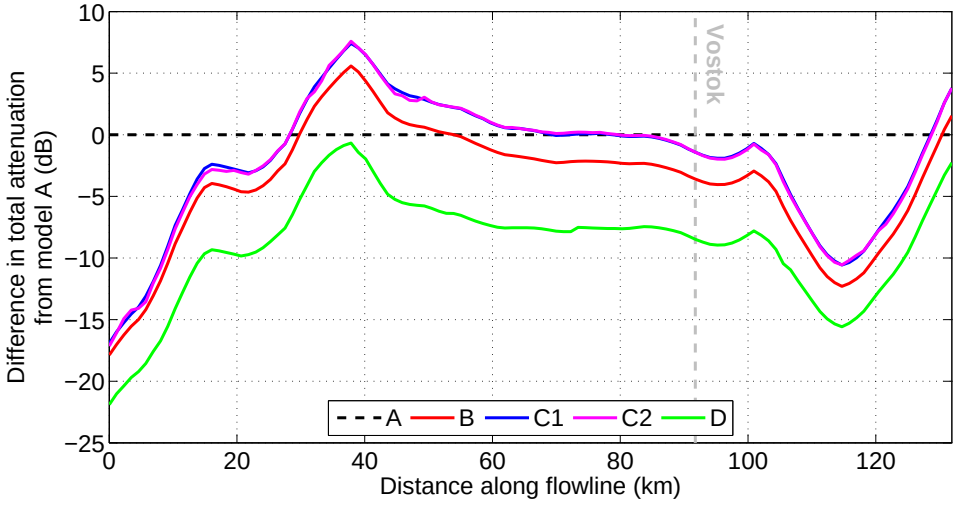

Figure 5.8: Difference in total (roundtrip) attenuation between models B/C1/C2/D and model A along the Vostok flowline. Model A is shown as a dashed horizontal line at 0 dB (it has zero difference from itself). Negative (positive) values of this difference imply that model A overestimates (underestimates) the total attenuation.

of any study of bed-echo intensities of distinguishing between wet and dry beds. Spatially varying temperatures are of primary importance when modeling attenuation. This result is expected, given the primary dependence of attenuation rates upon temperature. The inclusion of spatially varying impurity concentrations has only a secondary effect upon the attenuation rates.

Because our results show that reliable temperature models are critical for estimating the spatial variation of attenuation, improvements to temperature models will directly lead to improved attenuation estimates. Thermomechanical ice-sheeet models are becoming increasingly sophisticated in their treatment of different ice-flow regimes (e.g., ice divides versus ice streams) and spatially varying bed properties, such as geothermal flux (e.g., *Matsuoka et al.* (in prep.)). Although many of these models do not explicitly include subglacial processes (e.g., subglacial water transport) that affect the basal temperature or its condition (wet/dry), they offer an increasingly detailed prediction of ice-sheet temperatures that can be partially tested by borehole-temperature profiles (e.g., *Joughin et al.* (2004)) or indirect observations of subglacial water flux (*Fricker et al.* (2007)).

The Greenland and Antarctic ice sheets are increasingly well surveyed by radar (e.g., *Lythe et al.* (2001)), using both densely spaced grids (e.g., the SOAR data collected over Lake Vostok) and along modern flowlines (e.g., *Matsuoka et al.* (2003)). Radar surveying is also often part of the site-selection process for ice cores (e.g., *Morse et al.* (2002)), so radar transects crossing through ice-core sites are commonly available. Many areas of interest therefore have radar-layer depths that could be used to constrain the spatial variation of impurity concentrations (model C1) with little difficulty.

Models C1 and C2 could be refined by also rescaling the impurity-concentration profiles by using the spatial variation of the flowband width. This would account for the geometric effect of ice contracting and expanding transverse to flow. Although our model D underestimated the attenuation-rate field, its initial attempt to account for the impurity-deposition mechanisms is likely the route that future models of the spatial variation of attenuation should take. Model D could be improved using a transient thermomechanical ice-sheet model that keeps track of non-diffusive ice properties (e.g., *Clarke et al.* (2005)), rather than the reversed particle paths from the final state of velocity field. Impurity concentrations are non-diffusive, but as the initial ice volume deposited at the surface is strained, its volume will decrease, so the cumulative volume change must also be recorded.

5.6 Conclusions

We found that, for investigations of ice-sheet radio-echo intensities, the commonly used model of a uniform depth-averaged attenuation rate is generally inadequate. An ice-temperature model is the most critical element of an accurate two-dimensional radar-attenuation model, and layer-depth variations can be easily used to refine the impurity-concentration field of this radar-attenuation model. The spatial and temporal variation of impurity fluxes to the ice-sheet surface via wet and dry deposition also affects in situ impurity concentrations and hence attenuation rates. However, accounting for these variations requires detailed knowledge of the atmospheric impurity-concentration, accumulation-rate, and ice-flow histories along the flowline of interest, and these values can only be inferred from proxy data and models. Our results are critical for future investigations of internal-layer and bed reflectivities, and suggest that interpretations by earlier studies that used a

uniform-value attenuation-rate model should be revisited. We conclude that, for ice-sheet radar surveys that aim to investigate the spatial variation of echo intensities (e.g., subglacial lake detection), a reasonably accurate radar-attenuation model is one that includes the spatial variation of temperatures, and an even better one also uses an ice-core-derived impurity-concentration profile that is rescaled along the transect by radar layers.

Chapter 6

SYNTHESIS

This final chapter summarizes the previous four chapters of this dissertation, how this dissertation will impact the research of others in this field and what future work it suggests. Combined, this dissertation represents a logical and complete body of work suitable for a Ph.D.

6.1 Summary of This Dissertation

I first developed a radar-attenuation model for polar ice sheets after noticing a clear need for such a model in ongoing studies of polar ice sheets (Chapter 2). This model was based on a synthesis of experimental ice-conductivity data. This synthesis revealed that some dielectric properties of ice remain poorly known (particularly the pure-ice properties), but I was able to synthesize a radar-attenuation model that successfully matched the observed depth-averaged attenuation rate at Siple Dome. A similar success had not been previously achieved with a radar-attenuation model. Because this model was parameterized in such a way as to make it broadly applicable, and because it was not specifically tuned to Siple Dome, it opens doors to other glaciological applications where a radar-attenuation model would be valuable.

The first such application was an investigation of the nature of the radar detection of accreted ice over Lake Vostok (Chapter 3). Accreted ice has occasionally been observed by radar within ice shelves where basal accretion is occurring, but it had not been previously detected by radar over a subglacial lake until its observation by *Bell et al.* (2002). Using ice-core data from the accreted ice together with the radar-attenuation model, I determined that the most likely cause of the observed reflection is a fabric contrast between the dirty and clean accreted ices that formed over the lake. This reflection mechanism suggests that the spatial pattern of detection of accreted ice is related to either rapid accretion rates near

the shoreline or the spatial variation of attenuation as ice flows onto the lake.

Next, I investigated the spatial variability of accumulation rates over the Lake Vostok region using radar-layer depths, flowband modeling, and formal inverse theory (Chapter 4). The flowband modeling and inverse methods inferred smoother accumulation-rate patterns than those inferred using a local strain-rate approximation and also placed apparent accumulation-rate anomalies further upstream than those due to the simpler approximation. These results suggest that previous inferences of accumulation-rate anomalies over Lake Vostok did not sufficiently consider the effect of ice flow, but that the differences between the two methods are generally small relative to the regional pattern of accumulation rates. I also found the spatial pattern of accumulation rates that represents the mean pattern over the last 41 ka in this region.

This accumulation-rate map was used by a thermomechanical ice-sheet model to predict three-dimensional fields of temperature and ice velocities over Lake Vostok. I used these fields, along with radar-layer depths, to estimate the two-dimensional attenuation-rate field along a flowline that passed through the Vostok ice-core site (Chapter 5). I compared several different methods of estimating the attenuation-rate field to the simplest possible field, which was derived assuming uniform impurity concentrations and temperature. Methods that used non-uniform temperatures and observed (isochronal) radar layers to rescale the impurity-concentration profiles produced a sufficiently precise attenuation-rate field that was not significantly improved upon by more complex models. Such methods should become the standard approach for predicting the spatial variation of ice-sheet radar attenuation.

6.2 Impact and Future Work

The primary motivation for this dissertation was the recognition by the glaciology community that radar attenuation in ice sheets was poorly understood, that it likely varied significantly, and that a reliable radar-attenuation model would be valuable for addressing outstanding questions in glaciology, particularly those related to basal conditions. The work presented in this dissertation is not an exhaustive investigation of ice-sheet radar attenuation, but it is a novel and much-needed demonstration of the value of performing such studies, and a guide for conducting future similar studies.

Much has been learned about ice-sheet flow from the study of the geometry of radar layers in ice sheets (e.g., *Nereson et al.* (1998); *Conway et al.* (2002)). There are fewer studies of radio-echo intensities, but they can be equally revealing about the nature of ice-sheet flow and basal conditions (e.g., *Matsuoka et al.* (2003); *Carter et al.* (2007)). Such studies can be hindered by their ability to discuss only relative changes in echo intensities due to limited knowledge of radar attenuation. The work presented in this dissertation will allow the glaciology community to more reliably determine absolute reflectivity changes and quantitatively interpret observed echo-intensity variations.

Glaciologists need to accurately map ice-sheet basal conditions because of their impact on ice flow and modern sea-level rise (Chapter 1). The most immediate impact of this dissertation is the availability of a more accurate ice-sheet radar-attenuation model that is useful for estimation of attenuation at all spatial scales. Previous studies often used a single regional value of the depth-averaged attenuation rate to infer variations in the the bed reflectivity and basal conditions (e.g., *Peters et al.* (2005)). It is clear from this dissertation that the use of a single attenuation-rate value is inadequate for accurate inference of bed-reflectivity variations, and Chapter 5 presents methods for improving upon that simpler approach. Regions of the bed that are apparently bright are not necessarily absolutely bright if the attenuation is also low in that region of the overlying ice sheet. Such differences directly affect studies of ice-sheet flow that are based on parameterizations of basal conditions, e.g., *Parizek and Alley* (2004), who assigned a wet/dry bed in an ice-sheet model based on available radar data.

The methods presented here are also useful for investigation of subglacial lakes (Chapters 3–5). Although Lake Vostok is an exceptional subglacial lake, basal accretion and melting over subglacial lakes undoubtedly occur elsewhere (e.g., *Tikku et al.* (2005)), and the study of the echo intensity of the ice–lake interface over subglacial lakes is a potentially valuable tool for discriminating between freezing and melting ice–lake interfaces.

Since *Winebrenner et al.* (2003) first demonstrated how to measure of attenuation rates, there has been increased interest in performing such measurements. Novel measurement methods are being developed, including the estimation of attenuation rates from multiple reflections from the bed, which have been previously observed but not used for this purpose

(e.g., *Shabtaie and Bentley* (1982)). As the dynamic range, portability, triggering accuracy, noise levels, and antenna design of radar systems improve, so will the ability of these systems to accurately record the echo intensities of ever-fainter reflections and potentially to measure attenuation rates. Furthermore, the increased availability of outputs from reliable thermomechanical ice-flow models (e.g., *Joughin et al.* (2004); *Pattyn et al.* (2004)) makes it easier to compare modeled and measured attenuation rates, and to extend such results across larger regions. These scientific and technical developments will undoubtedly contribute to a better understanding of basal conditions across Greenland and Antarctica.

Ice softens as its temperature rises (*Paterson* (1994)), and temperature can be horizontally non-uniform over distances as small as 10 km in regions of an ice sheet that have a complex flow structure and history (e.g., *Engelhardt* (2004); *Joughin et al.* (2004)). Inferring ice-sheet temperatures from radar-attenuation data is therefore a problem of broad glaciological interest. Future work will address this problem, which differs from the determination of bed-reflectivity. It will require the estimation of the depth-averaged radar-attenuation rate to several internal layers and the bed, a radar-attenuation model, and formal inverse theory (e.g., *Aster et al.* (2005)). The most promising method for measuring local attenuation rates to several internal layers and the bed is the common-midpoint antenna configuration (*Winebrenner et al.* (2003)), where the transmitting and receiving antennæ are progressively separated from a fixed (common) midpoint. This method requires several technical advances in terms of receiver triggering and antenna beam-pattern estimation, but when these issues are resolved, the common-midpoint method will become a valuable new tool for measuring attenuation rates. The formal inverse problem itself is nonlinear but relatively straightforward. In this inverse problem, the temperature-dependent radar-attenuation model constitutes the "forward" model used to iteratively solve for a temperature profile that fits the attenuation-rate data to within their uncertainties.

Finally, the existing uncertainties in the radar-attenuation model strongly encourage further studies of the radar-frequency conductivity of polar ice, particularly pure ice (Chapter 2). The primary goals of these studies should be twofold: 1. to reduce existing uncertainties in the dielectric properties of ice, particularly their temperature dependence, and 2. to clarify the relationship with soluble impurities other than H^+ and ss Cl^- (e.g., NH_4^+), and the

possible spatial variability of those relationships between soluble-impurity concentrations and conductivity. The dielectric properties of ice at premelting temperatures ($> -10°C$) are especially uncertain and warrant further investigation, because radio waves commonly probe deep basal ice, whose temperature may be close to the pressure-melting point. Radar investigations of extraterrestrial ice bodies on Mars (e.g., *Picardi et al.* (2005)) and Europa (e.g., *Moore* (2000)) also require radar-attenuation models, which are further complicated by the presence of dust and other impurities. Ice-conductivity studies should also consider such impurities to successfully predict radar attenuation through these extraterrestrial ice bodies.

BIBLIOGRAPHY

Alley, R., R. Finkel, K. Nishizumi, S. Anandakrishnan, C. Shuman, G. Mershon, G. Zielinski, and P. Mayewski (1995), Changes in continental and sea-salt atmospheric loadings in central Greenland during the most recent deglaciation: model-based estimates, *J. Glaciol.*, *41*(139), 503–514.

Alley, R., P. Clark, P. Huybrechts, and I. Joughin (2005), Ice sheets and sea-level changes, *Science*, *310*, 456–460, doi:10.1126/science.1114613.

Anandakrishnan, S., D. Blankenship, R. Alley, and P. Stoffa (1998), Influence of subglacial geology on the position of a West Antarctic ice stream from seismic observations, *Nature*, *394*.

Arcone, S. (1995), Numerical studies of the radiation patterns of resistively loaded dipoles, *J. Appl. Geophys.*, *33*, 39–52.

Arthern, R., D. Winebrenner, and D. Vaughan (2006), Antarctic snow accumulation mapped using polarization of 4.3-cm wavelength microwave emission, *J. Geophys. Res.*, *111*, D06017, doi:10.1029/2004JD005667.

Aster, R., B. Borchers, and C. Thurber (2005), *Parameter Estimation and Inverse Problems*, 1st ed., 320 pp., Elsevier Academic Press, Burlington, MA.

Barnes, P., and E. Wolff (2004), Distribution of soluble impurities in cold glacial ice, *J. Glaciol.*, *50*(170), 311–324.

Barnes, P., E. Wolff, R. Mulvaney, R. Udisti, E. Castellano, R. Röthlisberger, and J.-P. Steffensen (2002), Effect of density on electrical conductivity of chemically laden polar ice, *J. Geophys. Res.*, *107*(B2), doi:10.1029/2000JB000080.

Bell, R. (2008), The role of subglacial water in ice-sheet mass balance, *Nature Geosci.*, *1*, 297–304, doi:10.1038/ngeo186.

Bell, R., M. Studinger, A. Tikku, G. Clarke, M. Gutner, and C. Meertens (2002), Origin and fate of Lake Vostok water frozen to the base of the East Antarctic ice sheet, *Nature*, *416*, 307–310.

Bell, R., M. Studinger, C. S. M. Fahnestock, and I. Joughin (2007), Large subglacial lakes in East Antarctica at the onset of fast-flowing ice streams, *Nature*, *445*, 904–907, doi: 10.1038/nature05554.

Bentley, C., N. Lord, and C. Liu (1998), Radar reflections reveal a wet bed beneath stagnant Ice Stream C and a frozen bed beneath ridge BC, West Antarctica, *J. Glaciol.*, *44*(146), 149–156.

Bevington, P. (1969), *Data Reduction and Error Analysis for the Physical Sciences*, 1st ed., 336 pp., McGraw-Hill, New York.

Blankenship, D., R. Bell, S. Hodge, J. Brozena, J. Behrendt, and C. Finn (1993), Active volcanism beneath the West Antarctic ice sheet and implications for ice-sheet stability, *Nature*, *361*, 526–529.

Blankenship, D., D. Morse, C. Finn, R. Bell, M. Peters, S. Kempf, S. Hodge, M. Studinger, and J. Behrendt (2001), Geologic controls on the initiation of rapid basal motion for the ice streams of the Southeastern Ross Embayment: A geophysical perspective including new airborne radar sounding and laser altimetry measurements, in *The West Antarctic Ice Sheet: Behavior and Environment*, edited by R. Alley and R. Bindschadler, pp. 105–121, Amer. Geophys. Union, Washington, DC.

Blindow, N. (1994), The central part of the Filchner–Ronne Ice Shelf, Antarctica: internal structures revealed by 40 MHz monopulse RES, *Ann. Glaciol.*, *20*, 365–371.

Bogorodsky, V., C. Bentley, and P. Gudmandsen (1985), *Radioglaciology*, 1st ed., D. Reidel Publishing Co., Dordrecht, Holland.

Brook, E., J. White, A. Schilla, M. Bender, B. Barnett, J. Severinghaus, K. Taylor, R. Alley, and E. Steig (2005), Timing of milennial-scale climate change at Siple Dome,

West Antarctica, during the last glacial period, *Quat. Sci. Rev.*, *24*, 1333–1343, doi: 10.1016/j.quascirev.2005.02.002.

Camplin, G., and J. Glen (1973), The dielectric properties of HF-doped single crystals of ice, in *Physics and Chemistry of Ice*, edited by E. Whalley, S. Jones, and L. Gold, pp. 256–261, Royal Soc. Canada, Ottawa.

Carter, S., D. Blankenship, M. Peters, D. Young, J. Holt, and D. Morse (2007), Radar-based subglacial lake classification in Antarctica, *Geochem. Geophys. Geosyst.*, *8*, Q03016, doi: 10.1029/2006GC001408.

Castellano, E., S. Becagli, J. Jouzel, A. Migliori, M. Severi, J. Steffensen, R. Traversi, and R. Udisti (2004), Volcanic eruption frequency over the last 45 ky as recorded in Epica-Dome C ice core (East Antarctica) and its relationship with climatic changes, *Glob. Planet. Change*, *42*, 195–205, doi:10.1016/j.gloplacha.2003.11.007.

Clarke, G., N. Lhomme, and S. Marshall (2005), Tracer transport in the Greenland ice sheet: three-dimensional isotopic stratigraphy, *Quat. Sci. Rev.*, *24*, 155–171, doi: 10.01016/j.quascirev.2004.08.021.

Clow, G., R. Slatus, and E. Waddington (1996), A new high-precision borehole-temperature logging system used at GISP2, Greenland and Taylor Dome, Antarctica, *J. Glaciol.*, *42*(142), 576–584.

Conway, H., B. Hall, G. Denton, A. Gades, and E. Waddington (1999), Past and future grounding-line retreat of the West Antarctic ice sheet, *Science*, *286*, 280–283.

Conway, H., G. Catania, C. Raymond, A. Gades, T. Scambos, and H. Engelhardt (2002), Switch of flow direction in an Antarctic ice stream, *Nature*, *419*(6906), 465–467, doi: 10.1038/nature01081.

Corr, H., J. Moore, and K. Nicholls (1993), Radar absorption due to impurities in Antarctic ice, *Geophys. Res. Lett.*, *20*(11), 1071–1074.

Cullen, D., and I. Baker (2001), Observations of impurities in ice, *Micro. Res. Tech.*, *55*, 198–207.

Dahe, Q., J.-R. Petit, J. Jouzel, and M. Stievenard (1994), Distribution of stable isotopes in surface snow along the route of the 1990 International Trans-Antarctica Expedition, *J. Glaciol.*, *40*(134), 107–118.

de Angelis, M., J.-R. Petit, J. Savarino, R. Souchez, and M. Thiemens (2004), Contributions of an ancient evaporitic-type reservoir to subglacial Lake Vostok chemistry, *Earth Planet. Sci. Lett.*, *222*, 751–765, doi:10.1016/j.epsl.2004.03.023.

de Angelis, M., M.-C. Morel-Fourcade, J.-M. Barnola, J. Susini, and P. Duval (2005), Brine micro-droplets and solid inclusions in accreted ice from Lake Vostok (East Antarctica), *Geophys. Res. Lett.*, *32*, L12501, doi:10.1029/2005GL022460.

Dixon, D., P. Mayewski, S. Kaspari, S. Sneed, and M. Handley (2004), A 200 year sub-annual record of sulfate in West Antarctica, from 16 ice cores, *Ann. Glaciol.*, *39*, 545–556.

Eisen, O., F. Wilhelms, U. Nixdorf, and H. Miller (2003), Revealing the nature of radar reflections in ice: DEP-based FDTD forward modeling, *Geophys. Res. Lett.*, *30*(5), doi: 10.1029/2002GL016403.

Eisen, O., I. Hamann, S. Kipfstuhl, D. Steinhage, and F. Wilhelms (2007), Direct evidence for continuous radar reflector originating from changes in crystal-orientation fabric, *The Cryosphere*, *1*, 1–10.

Engelhardt, H. (2004), Thermal regime and dynamics of the West Antarctic ice sheet, *Ann. Glaciol.*, *39*, 85–92.

Evans, S. (1965), Dielectric properties of ice and snow — a review, *J. Glaciol.*, *5*(42), 773–792.

Fricker, H., T. Scambos, R. Bindschadler, and L. Padman (2007), An active subglacial water system in West Antarctica mapped from space, *Science*, *315*, 1544–1548, doi: 10.1126/science.1136897.

Fujita, S., and S. Mae (1994), Causes and nature of ice-sheet radio-echo internal reflections estimated from the dielectric properties of ice, *Ann. Glaciol.*, *20*, 80–86.

Fujita, S., M. Shiraishi, and S. Mae (1992), Measurement on the dielectric properties of acid-doped ice at 9.7 GHz, *IEEE Trans. Geosci. Rem. Sens.*, *30*(4), 799–803.

Fujita, S., H. Maeno, S. Uratsuka, T. Furukawa, S. Mae, Y. Fujii, and O. Watanabe (1999), Nature of radio echo layering in the Antarctic ice sheet detected by a two-frequency experiment, *J. Geophys. Res.*, *104*(B6), 13,013–13,024.

Fujita, S., T. Matsuoka, T. Ishida, K. Matsuoka, and S. Mae (2000), A summary of the complex dielectric permittivity of ice in the megahertz range and its applications for radar sounding of polar ice sheets, in *Physics of Ice Core Records*, edited by T. Hondoh, pp. 185–212, Hokkaido Univ. Press, Sapporo, Japan.

Fujita, S., N. Azuma, H. Motoyama, T. Kameda, H. Narita, Y. Fujii, and O. Watanabe (2002a), Electrical measurements on the 2503 m Dome F Antarctic ice core, *Ann. Glaciol.*, *35*, 313–320.

Fujita, S., N. Azuma, H. Motoyama, T. Kameda, H. Narita, S. Matoba, M. Igarashi, M. Kohno, Y. Fujii, and O. Watanabe (2002b), Linear and non-linear relations between the high-frequency-limit conductivity, AC-ECM signals and ECM signals of Dome F Antarctic ice core from a laboratory experiment, *Ann. Glaciol.*, *35*, 321–328.

Fujita, S., H. Maeno, and K. Matusoka (2006), Radio-wave depolarization and scattering within ice sheets: a matrix-based model to link radar and ice-core measurements and its application, *J. Glaciol.*, *52*(178), 407–424.

Fukazawa, H., K. Sugiyama, S. Mae, H. Narita, and T. Hondoh (1998), Acid ions at triple junction of Antarctic ice observed by Raman scattering, *Geophys. Res. Lett.*, *25*(15), 2845–2848.

Gades, A., C. Raymond, H. Conway, and R. Jacobel (2000), Bed properties of Siple Dome and adjacent ice streams, West Antarctica, inferred from radio echo-sounding measurements, *J. Glaciol.*, *46*(152), 88–94.

Gogineni, P., T. Chuah, C. Allen, K. Jezek, and R. Moore (1998), An improved coherent radar depth sounder, *J. Glaciol.*, *44*(148), 659–669.

Gow, A., and H. Engelhardt (2000), Preliminary analysis of ice cores from Siple Dome, West Antarctica, in *Physics of Ice Core Records*, edited by T. Hondoh, pp. 63–82, Hokkaido Univ. Press, Sapporo, Japan.

Gow, A., H. Ueda, and D. Garfield (1968), Antarctic Ice Sheet: preliminary results of first core hole to bedrock, *Science*, *161*(3845), 1011–1013.

Gudmandsen, P. (1971), Electromagnetic probing of ice, in *Electromagnetic Probing in Geophysics*, edited by J. Wait, pp. 321–348, Golem Press, Boulder, Colorado.

Hammer, C., H. Clausen, and C. Langway (1997), 50,000 years of recorded global volcanism, *Clim. Change*, *35*, 1–15.

Holland, H. (1978), *The Chemistry of the Atmosphere and Oceans*, 1st ed., John Wiley & Sons, New York.

Horgan, H., S. Anandakrishnan, R. Alley, L. Peters, G. Tsoflias, D. Voigt, and J. Winberry (2008), Complex fabric development revealed by englacial seismic reflectivity: Jakobshavn Isbræ, Greenland, *Geophys. Res. Lett.*, *35*, L10501, doi:10.1029/2008GL033712.

Jackson, J. (1975), *Classical Electrodynamics*, 2nd ed., 848 pp., John Wiley & Sons, New York.

Jacobel, R., and B. Welch (2005), A time marker at 17.5 kyr BP detected throughout West Antarctica, *Ann. Glaciol.*, *41*, 47–51.

Jacobel, R., T. Scambos, C. Raymond, and A. Gades (1996), Changes in the configuration of ice stream flow from the West Antarctic Ice Sheet, *J. Geophys. Res.*, *101*(B3), 5499–5504.

Jeffries, M., W. Weeks, R. Shaw, and K. Morris (1993), Structural characteristics of congelation and platelet ice and their role in the development of Antarctic land-fast sea ice, *J. Glaciol.*, *39*(132), 223–238.

Johari, G., and P. Charette (1975), The permittivity and attenuation in polycrystalline and single-crystal ice Ih at 35 and 60 MHz, *J. Glaciol.*, *14*(71), 293–303.

Joughin, I., S. Tulaczyk, D. MacAyeal, and H. Engelhardt (2004), Melting and freezing beneath the Ross ice streams, Antarctica, *J. Glaciol.*, *50*(168), 96–108.

Jouzel, J., J.-R. Petit, R. Souchez, N. Barkov, V. Lipenkov, D. Raynaud, M. Stievenard, N. Vassiliev, V. Verbeke, and F. Vimeux (1999), More than 200 m of lake ice above subglacial Lake Vostok, Antarctica, *Science*, *286*(5447), 2138–2141, doi: 10.1126/science.286.5447.2138.

Kapitsa, A., J. Ridley, G. de Q. Robin, M. Siegert, and I. Zotikov (1996), A large deep freshwater lake beneath the ice of central East Antarctica, *Nature*, *381*, 684–686.

Keller, G. (1966), Electrical properties of rocks and minerals, in *Handbook of Physical Constants*, edited by S. Clark, pp. 553–577, Geol. Soc. Amer., Boulder, Colo.

King, J., P. Anderson, D. Vaughan, G. Mann, S. Mobbs, and S. Vosper (2004), Windborne redistribution of snow across an Antarctic ice rise, *J. Geophys. Res.*, *109*, D11104, doi:10.1029/2003JD004361.

Kovacs, A., A. Gow, and R. Morey (1995), The in-situ dielectric constant of polar firn revisited, *Cold Reg. Sci. Tech.*, *23*(3), 245–256.

Kreutz, K., P. Mayewski, L. Meeker, M. Twickler, and S. Whitlow (2000), The effect of spatial and temporal accumulation rate variability in West Antarctica on soluble ion deposition, *Geophys. Res. Lett.*, *27*(16), 2517–2520.

Larour, E., E. Rignot, I. Joughin, and D. Aubry (2005), Rheology of the Ronne Ice Shelf, Antarctica, inferred from satellite radar interferometry using an inverse control method, *Geophys. Res. Lett.*, *32*, L05503, doi:10.1029/2004GL021693.

Legrand, M., and M. de Angelis (1996), Light carboxylic acids in Greenland ice: A record of past forest fires and vegetation emissions from the boreal zone, *J. Geophys. Res.*, *101*(D2), 4129–4145.

Legrand, M., and R. Delmas (1988), Formation of HCl in the Antarctic atmosphere, *J. Geophys. Res.*, *93*(D6), 7153–7168.

Legrand, M., and P. Mayewski (1997), Glaciochemistry of polar ice cores: a review, *Rev. Geophys.*, *35*(3), 219–243.

Legrand, M., C. Lorius, N. Barkov, and V. Petrov (1988), Vostok (Antarctica) ice core: atmospheric chemistry changes over the last climatic cycle (160,000 years), *Atmos. Envir.*, *22*(2), 317–331.

Leonard, K., R. Bell, M. Studinger, and B. Tremblay (2004), Anomalous accumulation rates in the Vostok ice-core resulting from ice flow over Lake Vostok, *Geophys. Res. Lett.*, *31*, L24401, doi:10.1029/2004GL021102.

Lipenkov, V., A. Salamatin, and P. Duval (1997), Bubbly-ice densification in ice sheets: II. Application, *J. Glaciol.*, *43*(145), 397–407.

Lipenkov, V., A. Ekaykin, N. Barkov, and M. Pourchet (1998), On the relationship of the surface snow density in Antarctica and wind speed (in Russian), *Mater. Glyatsiol. Issled.*, *85*, 148–158.

Lipenkov, V., Y. Shibayev, A. Salamatin, A. Ekaykin, R. Vostretsov, and A. Preobrazhenskaya (2004), Recent climatic variations reflected in the upper 80 m of the Vostok borehole temperature profiles, *Mater. Glyatsiol. Issled.*, *97*, 44–56.

Looyenga, H. (1965), Dielectric constants of heterogeneous mixtures, *Physica*, *31*(3), 401–406.

Lythe, M. B., D. G. Vaughan, and the BEDMAP Consortium (2001), BEDMAP: A new ice thickness and subglacial topographic model of Antarctica, *J. Geophys. Res.*, *106*(B6), 11,335–11,351.

Magand, O., C. Genthon, M. Fily, G. Krinner, G. Picard, M. Frezzotti, and A. Ekaykin (2007), An up-to-date quality-controlled surface mass balance data set for the 90°E–

180°E Antarctica sector and 1950–2005 period, *J. Geophys. Res.*, *112*, D12106, doi: 10.1029/2006JD007691.

Matsuoka, K., S. Fujita, T. Matsuoka, T. Ishida, T. Hondoh, and S. Mae (1996), Measurements of the complex permittivity of acid-doped ice from 1 kHz to 30 MHz — new data set for developing ice radar and dielectric analysis of ice cores, in *Proc. NIPR Symp. Polar Meteorol. Glaciol.*, vol. 10, edited by Nat. Inst. Polar Res., pp. 25–35, Tokyo, Japan.

Matsuoka, K., H. Maeno, S. Uratsuka, S. Fujita, T. Furukawa, and O. Watanabe (2002), A ground-based multi-frequency ice-penetrating radar system, *Ann. Glaciol.*, *34*, 171–176.

Matsuoka, K., T. Furukawa, S. Fujita, H. Maeno, S. Uratsuka, R. Naruse, and O. Watanabe (2003), Crystal orientation fabrics within the Antarctic ice sheet revealed by a multipolarization plane and dual-frequency radar survey, *J. Geophys. Res.*, *108*(B10), doi: 10.1029/2003JB002425.

Matsuoka, K., F. Pattyn, and J. MacGregor (in prep.), Continent-wide attenuation-rate distribution for Antarctica inferred from ice-temperature modeling.

Matsuoka, T., S. Fujita, and S. Mae (1997a), Dielectric properties of ice containing ionic impurities at microwave frequencies, *J. Phys. Chem. B*, *101*, 6219–6222.

Matsuoka, T., S. Fujita, S. Morishima, and S. Mae (1997b), Precise measurement of dielectric anisotropy in Ice Ih at 39 GHz, *J. Appl. Phys.*, *81*(5), 2344–2348.

Mayewski, P., M. Twickler, and S. Whitlow (1995), The Siple Dome ice core — Reconnaissance glaciochemistry, *Antarct. J. U.S.*, *30*(5), 85–87.

Millar, D. (1981), Radio-echo layering ice polar ice sheets and past volcanic activity, *Nature*, *292*, 441–443.

Miners, W., E. Wolff, J. Moore, R. Jacobel, and L. Hempel (2002), Modeling the radio echo reflections inside the ice sheet at Summit, Greenland, *J. Geophys. Res.*, *107*(B8), doi:10.1029/2001JB000535.

Montagnat, M., P. Duval, P. Bastie, B. Hamelin, O. Brissaud, M. de Angelis, J.-R. Petit, and V. Lipenkov (2001), High crystalline quality of large single crystals of subglacial ice above Lake Vostok (Antarctica) revealed by hard X-ray diffraction, *C. R. Acad. Sci. Paris, Series II-A*, *333*, 419–425.

Moore, J. (2000), Models of radar absorption in Europan ice, *Icarus*, *147*, 292–300, doi: 10.1006/icar.2000.6425.

Moore, J., and S. Fujita (1993), Dielectric properties of ice containing acid and salt impurity at microwave and low frequencies, *J. Geophys. Res.*, *98*(B6), 9769–9780.

Moore, J., R. Mulvaney, and J. Paren (1989), Dielectric stratigraphy of ice: a new technique for determining total ionic concentrations in polar ice cores, *Geophys. Res. Lett.*, *16*(10), 1177–1180.

Moore, J., J. Paren, and H. Oerter (1992a), Sea salt dependent electrical conduction in polar ice, *J. Geophys. Res.*, *97*(B13), 19,803–19,812.

Moore, J., E. Wolff, H. Clausen, and C. Hammer (1992b), The chemical basis for the electrical stratigraphy of ice, *J. Geophys. Res.*, *97*(B2), 1887–1896.

Moore, J., A. Reid, and J. Kipfstuhl (1994a), Microstructure and electrical properties of marine ice and its relationship to meteoric ice and sea ice, *J. Geophys. Res.*, *99*(C3), 5171–5180.

Moore, J., E. Wolff, H. Clausen, C. Hammer, M. Legrand, and K. Fuhrer (1994b), Electrical response of the Summit-Greenland ice core to ammonium, sulphuric acid, and hydrochloric acid, *Geophys. Res. Lett.*, *21*(7), 565–568.

Morse, D., D. Blankenship, E. Waddington, and T. Neumann (2002), A site for deep ice coring in West Antarctica: results from aerogeophysical surveys and thermo-kinematic modeling, *Ann. Glaciol.*, *35*, 36–44.

Mulvaney, R., E. Wolff, and K. Oates (1988), Sulphuric acid at grain boundaries in Antarctic ice, *Nature*, *331*, 247–249.

Murray, T., H. Corr, A. Forieri, and A. Smith (2008), Contrasts in hydrology between regions of basal deformation and sliding beneath Rutford Ice Stream, West Antarctica, mapped using radar and seismic data, *Geophys. Res. Lett.*, *35*, L12504, doi: 10.1029/2008GL033681.

Nereson, N., and E. Waddington (2002), Isochrones and isotherms beneath migrating ice divides, *J. Glaciol.*, *48*(160), 95–108.

Nereson, N., C. Raymond, R. Jacobel, and E. Waddington (2000), The accumulation pattern across Siple Dome, West Antarctica, inferred from radar-detected internal layers, *J. Glaciol.*, *46*(152), 75–87.

Nereson, N. A., C. F. Raymond, E. D. Waddington, and R. W. Jacobel (1998), Migration of the Siple Dome ice divide, West Antarctica, *J. Glaciol.*, *44*(148), 643–652.

Oerter, H., J. Kipfstuhl, J. Determann, H. Miller, D. Wagenbach, A. Minkin, and W. Grag (1992), Evidence for basal marine ice in the Filchner–Ronne Ice Shelf, *Nature*, *358*, 399–401.

Oswald, G., and S. Gogineni (2008), Recovery of subglacial water extent from Greenland radar survey data, *J. Glaciol.*, *54*(184), 94–106.

Paren, J. (1981), Reflection coefficient at a dielectric interface, *J. Glaciol.*, *27*(95), 203–204.

Paren, J., and G. Q. Robin (1975), Internal reflections in polar ice sheets, *J. Glaciol.*, *14*(71), 251–259.

Parizek, B., and R. Alley (2004), Ice thickness and isostatic imbalances in the Ross Embayment, West Antarctica: model results, *Global Planet. Change*, *42*, 265–278.

Parrenin, F., F. Rémy, C. Ritz, M. Siegert, and J. Jouzel (2004), New modeling of the Vostok ice flow line and implication for the glaciological chronology of the Vostok ice core, *J. Geophys. Res.*, *109*, D20102, doi:10.1029/2004JD004561.

Paterson, W. (1994), *The Physics of Glaciers*, 3rd ed., 481 pp., Butterworth-Heinemann, Oxford, England.

Pattyn, F., B. D. Smedt, and R. Souchez (2004), Influence of subglacial Vostok lake on the regional ice dynamics of the Antarctic ice sheet: a model study, *J. Glaciol.*, *50*(171), 583–589.

Peters, M., D. Blankenship, and D. Morse (2005), Analysis techniques for coherent airborne radar sounding: Application to West Antarctic ice streams, *J. Geophys. Res.*, *110*, B06303, doi:10.1029/2004JB003222.

Petit, J.-R. (2003), Ice–water exchanges in Lake Vostok constrained by an energy-balance model, *Geophys. Res. Abstr.*, *5*, 03628.

Petit, J.-R., J. Jouzel, D. Raynaud, N. Barkov, J.-M. Barnola, I. Basile, M. Benders, J. Chappelaz, M. Davis, G. Delaygue, M. Delmotte, V. Kotlyakov, M. Legrand, V. Lipenkov, C. Lorius, L. Pepin, C. Ritz, E. Saltzman, and M. Stievenard (1999), Climate and atmospheric history of the past 420,000 years from the Vostok ice core, Antarctica, *Nature*, *399*(6735), 429–436.

Petrenko, V., and R. Whitworth (1999), *Physics of Ice*, 1st ed., Oxford University Press, Oxford, England.

Picardi, G., J. Plaut, D. Biccari, O. Bombaci, D. Calabrese, M. C. A. Cicchetti, S. Clifford, P. Edenhofer, W. Farrell, C. Federico, A. Frigeri, D. G. T. Hagfors, E. Heggy, A. Herique, R. Huff, A. Ivanov, W. Johnson, R. Jordan, D. Kirchner, W. Kofman, C. Leuschen, E. Nielsen, R. Orosei, E. Pettinelli, R. Philips, D. Plettemeier, A. Safaeinili, R. Seu, E. Stofan, G. Vannaroni, T. Watters, and E. Zampolini (2005), Radar soundings of the subsurface of Mars, *Science*, *310*, 1925–1928, doi:10.1126/science.1122165.

Popov, S., A. Sheremetyev, V. Masolov, V. Lukin, A. Mironov, and V. Luchiniov (2003), Velocity of radio-wave propagation in ice and Vostok station, Antarctica, *J. Glaciol.*, *49*(165), 179–183.

Price, S., E. Waddington, and H. Conway (2007), A full-stress thermomechanical flow band model using the finite volume method, *J. Geophys. Res.*, *112*, F03020, doi: 10.1029/2006JF000724.

Rankin, A., V. Auld, and E. Wolff (2000), Frost flowers as a source of fractionated sea salt aerosol in the polar regions, *Geophys. Res. Lett.*, *27*(21), 3469–3472.

Rankin, A., E. Wolff, and R. Mulvaney (2004), A reinterpretation of sea-salt records in Greenland and Antarctic ice cores?, *Ann. Glaciol.*, *39*, 276–282.

Rasmussen, L. (1986), Refraction correction for radio-echo soundings of ice overlain by firn, *J. Glaciol.*, *32*(111), 192–194.

Rignot, E., J. Bamber, M. van den Broeke, C. Davis, Y. Li, W. J. van de Berg, and E. van Meijaard (2008), Recent Antarctic ice mass loss from radar interferometry and regional climate modeling, *NATGEO*, *1*, 106–110, doi:10.1028/ngeo102.

Robin, G. (1975), Radio-echo sounding: glaciological interpretations and applications, *J. Glaciol.*, *15*(73), 49–64.

Robin, G., S. Evans, and J. Bailey (1969), Interpretation of radio echo sounding in polar ice sheets, *Phil. Trans. Royal Soc. London, Ser. A*, *265*(1166), 437–505.

Salamatin, A., E. Tsyganova, S. Popov, and V. Lipenkov (in press), Ice flow line modeling in ice core data interpretation, in *Physics of Ice Core Records*, vol. 2, edited by T. Hondoh, Hokkaido Univ. Press, Sapporo, Japan.

Saltzman, E., I. Dioumaeva, and B. Finley (2006), Glacial/interglacial variations in methanesulfonate (MSA) in the Siple Dome ice core, West Antarctica, *Geophys. Res. Lett.*, *33*, L11811, doi:10.1029/2005GL025629.

Shabtaie, S., and C. Bentley (1982), Tabular icebergs – Implications from geophysical studies of ice shelves, *J. Glaciol.*, *28*(100), 413–430.

Shabtaie, S., I. Whillans, and C. Bentley (1987), The morphology of ice streams A, B, and C, West Antarctic, and their environs, *J. Geophys. Res.*, *92*(B2), 8865–8883.

Siegert, M. (2003), Glacial–interglacial variations in central East Antarctic ice accumulation rates, *Quat. Sci. Rev.*, *22*, 741–750.

Siegert, M., R. Kwok, C. Mayer, and B. Hubbard (2000), Water exchange between the subglacial Lake Vostok and the overlying ice sheet, *Nature*, *403*, 643–646.

Smith, A., T. Murray, K. Nicholls, K. Makinson, G. Aoalgersdóttir, A. Behar, and D. Vaughan (2007), Rapid erosion, drumlin formation, and changing hydrology beneath and Antarctic ice stream, *Geology*, *35*(2), doi:10.1130/G23036A.1.

Souchez, R., J.-R. Petit, J.-L. Tison, J. Jouzel, and V. Verbeke (2000), Ice formation in subglacial Lake Vostok, Central Antarctica, *Earth Planet. Sci. Lett.*, *181*, 529–538.

Souchez, R., J.-R. Petit, J. Jouzel, M. de Angelis, and J.-L. Tison (2003), Reassessing Lake Vostok's behaviour from existing and new ice core data, *Earth Planet. Sci. Lett.*, *217*, 163–170, doi:10.1016/S0012-821X(03)00588-0.

Steen-Larsen, H., M. Koutnik, and E. Waddington (2007), Formulating an inverse problem to determine the accumulation rate pattern from keep internal lyaering in an ice sheet, *Geophys. Res. Abstr.*, *9*(01181).

Studinger, M., R. Bell, G. Karner, A. Tikku, J. Holt, D. Morse, T. Richter, S. Kempf, M. Peters, D. Blankenship, R. Sweeney, and V. Rystrom (2003), Ice cover, landscape setting, and geological framework of Lake Vostok, East Antarctica, *Earth Planet. Sci. Lett.*, *205*, 195–210.

Studinger, M., R. Bell, and A. Tikku (2004), Estimating the depth and shape of subglacial Lake Vostok's water cavity from aerogravity data, *Geophys. Res. Lett.*, *31*, L12401, doi: 10.1029/2004GL019801.

Sugiyama, K., S. Fujita, H. Narita, S. Mae, T. Hondoh, K. Goto-Azuma, D. Fisher, and R. Koerner (2000), Measurement of electrical conductance in ice cores by AC-ECM method, in *Physics of Ice Core Records*, edited by T. Hondoh, pp. 173–184, Hokkaido Univ. Press, Sapporo, Japan.

Tabacco, I., C. Bianchi, A. Zirizzotti, E. Zuccheritti, A. Forieri, and A. D. Vedova (2002), Airborne radar survey above Vostok region, east-central Antarctica: ice thickness and Lake Vostok geometry, *J. Glaciol.*, *48*(160), 62–69.

Takei, I., and N. Maeno (1987), Electric characteristics of point defects in HCl-doped ice, *J. de Physique*, *48*(C1), 121–126.

Taylor, K., and R. Alley (2004), Two-dimensional electrical stratigraphy of the Siple Dome (Antarctica) ice core, *J. Glaciol.*, *50*(169), 231–235.

Thoma, M., K. Grosfeld, and C. Mayer (2008), Modelling accreted ice in subglacial Lake Vostok, Antarctica, *Geophys. Res. Lett.*, *35*, L11504, doi:10.1029/2008GL033607.

Tikku, A., R. Bell, M. Studinger, and G. Clarke (2004), Ice flow field over Lake Vostok, East Antarctica inferred by structure tracking, *Earth Planet. Sci. Lett.*, *227*, 249–261, doi:10.1016/j.epsl.2004.09.021.

Tikku, A., R. Bell, M. Studinger, G. Clarke, I. Tabacco, and F. Ferraccioli (2005), Influx of meltwater to subglacial Lake Concordia, East Antarctica, *J. Glaciol.*, *51*(172), 96–104.

Tsyganova, E., and A. Salamatin (2004), Non-stationary temperature field simulations along the ice flow line "Ridge B – Vostok Station", East Antarctica, *Mater. Glyatsiol. Issled.*, *97*, 57–70.

Vaughan, D., H. Corr, C. Doake, and E. Waddington (1999), Distortion of ischronous layers in ice revealed by ground-penetrating radar, *Nature*, *398*, 323–326.

Vieli, G. J.-M. C. L., M. Siegert, and A. Payne (2004), Reconstructing ice sheet accumulation rates at ridge B, East Antarctica, *Ann. Glaciol.*, *39*, 326–330.

Waddington, E., T. Neumann, M. Koutnik, H.-P. Marshall, and D. Morse (2007), Inference of accumulation-rate patterns from deep layers in glaciers and ice sheets, *J. Glaciol.*, *53*(183), 694–712.

Wendt, J., R. Dietrich, M. Fritsche, A. Wendt, A. Yuskevich, A. Kokhanov, A. Senatorov, V. Lukin, K. Shibuya, and K. Koi (2006), Geodetic observations of ice flow velocities over the southern part of subglacial Lake Vostok, Antarctica, and their glaciological implications, *Geophys. J. Int.*, *166*, 991–998, doi:10.1111/j.l365-246X.2006.03061.x.

Wettlaufer, J. (1999), Impurity effects in the premelting of ice, *Phys. Rev. Lett.*, *82*(12), 2516–2519.

Winebrenner, D., B. Smith, G. Catania, H. Conway, and C. Raymond (2003), Radio-frequency attenuation beneath Siple Dome, West Antarctica from wide-angle and profiling radar observations, *Ann. Glaciol.*, *37*, 226–232.

Wolff, E. (2000), Electrical stratigraphy of polar ice cores: principles, methods and findings, in *Physics of Ice Core Records*, edited by T. Hondoh, pp. 155–171, Hokkaido Univ. Press, Sapporo, Japan.

Wolff, E., and J. Paren (1984), A two-phase model of electrical conduction in polar ice sheets, *J. Geophys. Res.*, *89*(B11), 9433–9438.

Wolff, E., J. Moore, H. Clausen, C. Hammer, J. Kipfstuhl, and K. Fuhrer (1995), Long-term changes in the acid and salt concentrations of the Greenland Ice Core Project ice core from electrical stratigraphy, *J. Geophys. Res.*, *100*(D8), 16,249–16,263.

Wolff, E., W. Miners, J. Moore, and J. Paren (1997), Factors controlling the electrical conductivity of ice from the polar regions – a summary, *J. Phys. Chem. B*, *101*, 6090–6094.

Wüest, A., and E. Carmack (2000), A priori estimates of mixing and circulation in the hard-to-reach water body of Lake Vostok, *Ocean. Modell.*, *2*, 29–43.

Appendix A

REFLECTION LOSS

Power loss at internal reflecting layers could result in an overestimate of attenuation due to dielectric absorption measured by radar. In the frequency range of 1–10 MHz, internal reflections are mainly caused by changes in conductivity due to volcanogenic acids (*Fujita and Mae* (1994)). The reflectivity $|R|$ for an internal reflection due to an acid layer is calculated following *Paren* (1981) as $|R| = (\Delta\sigma/8\pi f\varepsilon'_r\varepsilon_0)^2$, where f is frequency. The two-way reflection loss R_L across n reflectors that have the same $|R|$ is $R_L = 1 - (1 - |R|)^{2n}$. We estimate an upper bound on the magnitude of two-way reflection loss expected in West Antarctica using data from the Byrd ice core, our conductivity model and the above method for calculating layer reflectivities. We use the Byrd ice core to estimate reflection loss rather than the Siple Dome ice core because we prefer to estimate $|R|$ for a ice-core volcanic signal that is clearly matched to a prominent radar layer.

Hammer et al. (1997) reported on volcanism at Byrd detected by ECM and found 57 large volcanic events over the last $\sim$ 50 ka over a depth range of 88–2164 m. The largest event that they reported occurred $\sim$ 17.5 ka ago and consists of several $[H^+]$ peaks of $\sim$ 10 μM above a background $[H^+]$ of 1.5 μM and a background $[\mathrm{ss\,Cl^-}]$ of 2.0 μM. This event corresponds to a prominent radar layer that has been tracked over a large portion of West Antarctica (*Jacobel and Welch* (2005)). Using these peak and background concentrations and the measured ice temperature at the depth of this event ($-25°$C, *Gow et al.* (1968)), we use (2.1) to calculate the conductivity difference between the acid peaks and the background as $\Delta\sigma = 24 \pm 7$ $\mu\mathrm{S\,m^{-1}}$. Using $f = 1$ MHz yields $|R| = -29 \pm 2$ dB. This value of $|R|$ is larger than the range of typical values (-55 to -80 dB) reported by *Fujita and Mae* (1994), so we consider it an end-member case that provides an upper bound on the magnitude of reflection loss at a single layer. The two-way reflection loss after 57 such events, spanning 50 ka, is $R_L = -0.6$ dB of the power transmitted into the ice sheet. This value of R_L

is probably a slight underestimate for the last 50 ka because the depth range of 300–900 m in the Byrd core was not measured by ECM. Multiple reflections between layers are also ignored because *Miners et al.* (2002) showed that they are small compared to primary reflections.

At Siple Dome, ice from 50 ka ago occurs at a depth of $\sim$ 900 m (*Brook et al.* (2005)). Assuming that the frequency of volcanic events recorded at Siple Dome is similar to that at Byrd, we expect the total two-way reflection loss over the upper 900 m to be ~ -0.6 dB. Reflection loss in the lower $\sim$ 100 m of the ice will increase this value slightly, but this calculation shows that power loss from internal reflections is small compared to loss from dielectric absorption. The frequency of volcanic events recorded in ice cores is generally higher in Greenland than in Antarctica, so this loss calculation may be an underestimate in Greenland.

Appendix B

RELATIONSHIPS BETWEEN ELECTRICAL DATA AND IMPURITY CONCENTRATIONS

Electrical logs of ice cores are often related to impurity concentrations and can be used to independently validate impurity concentration profiles from major-ion data. ECM currents are often found to have a power-law relationship with $[H^+]$ of the form $[H^+] = a \cdot \mathrm{ECM}^b$, where a and b vary depending on the ECM instrument used and the ice cores measured (*Wolff et al.* (1997)). Direct comparison between raw ECM measurements and calculated $[H^+]$ profiles is difficult because they were measured at different sampling intervals and have independent noise sources. An independent validation of the $[\mathrm{ss\,Cl}^-]$ profile using ECM data is not possible because ECM does not respond to the Bjerrum-L defects formed by $\mathrm{ss\,Cl}^-$ ions (*Wolff et al.* (1997)).

Here we compare ECM and $[H^+]$ profiles that have been spatially averaged. We only use measurements within the depth range 100–799 m; above 100 m, the ECM currents are lower, probably due to lower densities in the firn, and ECM was not measured at depths greater than 799 m. Figure B.1 shows the non-linear least-squares fit between these 10-m averaged ECM and $[H^+]$ profiles; the best-fit exponent ($b = 1.04 \pm 0.25$) is lower than the $[H^+]$ calibrations for most ECM instruments but it does fall within the range of reported values (e.g., *Moore et al.* (1992b)). No previous $[H^+]$ calibration exists for the ECM instrument used on the Siple Dome core, so it is not possible to directly compare these best-fit coefficients to previous results. The scatter in this relationship is similar to that for other ice cores (*Moore et al.* (1992b), *Wolff et al.* (1995)) and the fraction of explained variance is 0.56; the fraction of explained variance decreases to 0.42 when averaging over 2-m intervals. Overall, the observed relationship between the ECM and calculated $[H^+]$ profiles is indicative of the validity of (2.8).

Another electrical method that was used to study the Siple Dome ice core is CCM, which

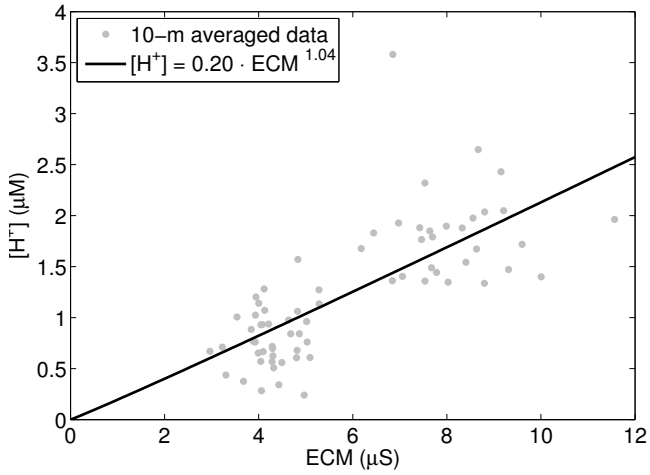

Figure B.1: Non-linear least-squares fit between 10-m averaged ECM and calculated $[H^+]$ profiles within the depth range 100–799 m at Siple Dome. The fraction of explained variance is 0.56.

is similar to AC-ECM (e.g., *Sugiyama et al.* (2000)) so we might expect a linear relationship between CCM and impurity concentrations. However, the Siple Dome CCM data are not calibrated and are reported as conductances, not conductivities. Here we compare CCM data over the same depth range as before (100–799 m) to the $[H^+]$ and $[\mathrm{ss}\,Cl^-]$ profiles using a multiple linear regression of the form $\mathrm{CCM} = j + k[H^+] + l[\mathrm{ss}\,Cl^-]$. This yields a value of k that is 3 times larger than l, which is lower than the ratio of μ_{H^+} to $\mu_{\mathrm{ss}\,Cl^-}$ expected from Table 2.1 (7.4). The fraction of explained variance for this regression using observations averaged over 10-m intervals is 0.55.

Appendix C

RADAR-DERIVED ATTENUATION

Our adjustments to the calculation of attenuation derived from radar traverse data originally presented by *Winebrenner et al.* (2003) include:

1. Ice thicknesses are used instead of two-way traveltimes in the attenuation calculation. The radio-wave velocity profile is calculated using the measured density profile with Looyenga's dielectric mixing equation (*Kovacs et al.* (1995)) and is also adjusted for the refraction of the raypath in the firn (e.g., *Rasmussen* (1986)).

2. BRPs are calculated using the sinusoidal integration method of *Gades et al.* (2000). This produces a more stable estimate of the reflected power than the method used by *Winebrenner et al.* (2003).

3. *Winebrenner et al.* (2003) binned traveltime ranges and used a limited number of BRPs from each bin to avoid biasing the fit. However, we find that this binning procedure does not significantly alter the fit. Here we do not bin the data and all BRPs within 54 km of the ice divide are used.

4. *Winebrenner et al.* (2003) used a non-linear least-squares relationship that included a calibration for geometric spreading. We eliminate the need to calibrate for geometric spreading by normalizing the BRPs by BRP_0, which is the mean BRP value of all traverse data within 1 km of the Siple Dome ice divide:

$$\frac{\mathrm{BRP}}{\mathrm{BRP}_0} = \frac{H_0^2}{H^2} \exp\left[-\frac{2}{L_a^*}\left(H - H_0\right)\right], \tag{C.1}$$

where L_a^* is the depth-averaged attenuation length, H is ice thickness and H_0 is the mean ice thickness from all the bed reflections within 1 km of the Siple Dome ice divide. We use a non-linear least-squares fit to find the value of L_a^* that minimizes

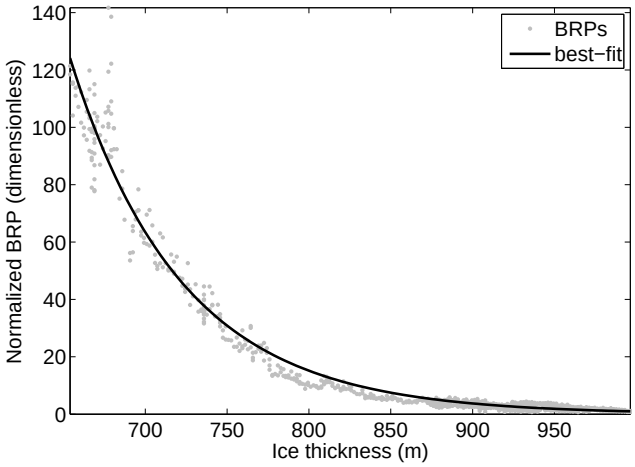

Figure C.1: Normalized Siple Dome BRPs from traverse data vs. ice thickness. Normalized BRP is calculated as the left-hand side of (C.1). The solid line is the non-linear least-squares fit to these data. The traverse data span 54 km both north and south of the ice divide. The best-fit depth-averaged attenuation rate is 25.3 ± 1.1 dB km^{-1}; the fraction of explained variance is 0.97.

the root-mean-square of the residuals between the data and the fit using (C.1). L_a^* is converted to a depth-averaged attenuation rate using (2.10).

The application of this method to all of the Siple Dome traverse data within 54 km of the ice divide is shown in Figure C.1. The revised radar-derived depth-averaged attenuation rate calculated using this method is 25.3 ± 1.1 dB km^{-1}, where the uncertainty is the 99% confidence interval. This value is 0.6 dB km^{-1} less than the value calculated by *Winebrenner et al.* (2003).

VITA

Joseph A. MacGregor

Education

1. Ph.D., 2008, Geophysics, University of Washington
   Thesis title: Development and applications of a radar-attenuation model for polar ice sheets

2. B.S. with honors, 2002, Geophysical Engineering. Colorado School of Mines

Publications

1. MacGregor, J.A., K. Matsuoka, M.R. Koutnik, E.D. Waddington, M. Studinger and D.P. Winebrenner, in review, Milennially averaged accumulation rates for the Lake Vostok region from deep internal layers, *Annals of Glaciology*.

2. Jacobel, R.W., B.C. Welch, D. Osterhouse, R. Pettersson and J.A. MacGregor, in review, Spatial variation of basal conditions on Kamb Ice Stream, *Annals of Glaciology*.

3. MacGregor, J.A., K. Matsuoka and M. Studinger, in review, Radar detection of accreted ice over Lake Vostok, Antarctica, *Earth and Planetary Science Letters*.

4. MacGregor, J.A., D.P. Winebrenner, H. Conway, K. Matsuoka, P.A. Mayewski and G.D. Clow, 2007, Modeling englacial radar attenuation at Siple Dome, West Antarctica, using ice chemistry and temperature data. *Journal of Geophysical Research*, 112, F03008.

5. O'Neal, M.A., M.E. O'Mansky and J.A. MacGregor, 2005, Modeling the natural degradation of earthworks, *Geoarchaeology*, 20(7), 739–748.